Microfluidic Tools for Advanced Biomolecular Characterisation

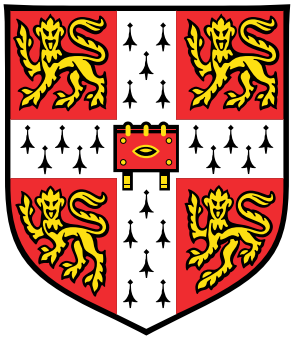

Tadas Kartanas

Department of Chemistry

University of Cambridge

This Dissertation is Submitted for the Degree of *Doctor of Philosophy*

Girton College

September 2018

Declaration

This dissertation is the result of my own work and includes nothing which is the outcome of work done in collaboration except where specifically indicated in the text. It is not substantially the same as any that I have submitted for a degree or diploma at the University of Cambridge or any other University or similar institution.

This dissertation does not exceed the prescribed word limit of 60,000 words.

Cambridge, 17th September 2018

Tadas Kartanas

Abstract

Proteins – the key building blocks of life – are responsible for the majority of the processes behind biological function. To understand what role proteins play in health and disease, how they operate and interact, it is vital to have tools for biomolecular detection, quantification and fundamental physicochemical characterisation. In this thesis, I have focused on the development of new microfluidic approaches enabling quantitative analysis of biomolecules.

First, I describe a microfluidic spray device, developed for a controlled deposition of analyte on surfaces. Due to the small micron-scale droplet size, the evaporation happens in a few milliseconds, thus, leaving only the solvent-free solutes. This method has been vital for depositing biomolecules on a scanning-probe microscopy-imaging substrate, enabling quantitative measurements of heterogeneous protein mixtures. Afterwards, I present the spray combination with gravimetric sensors, such as micro-cantilevers, for a label-free protein detection. I show that this technique can be used for a protein-solution concentration measurement in a quantitative manner. Currently, one of the main issues of diagnostic platforms is the analysis of heterogeneous mixtures. A number of protein-separation techniques have been developed; however, most of the characterisation requires an offline analysis which can introduce artefacts and reequilibration.

In the second part of this dissertation, I bridge the gap between liquid chromatography, microfluidic characterisation and mechanical-sensor detection. Specifically, I demonstrate the serial combination between liquid chromatography and analyte deposition by a microfluidic spray nozzle. By depositing analytes onto a quartz-crystal microbalance, I perform a specific label-free analysis of protein mixtures. Furthermore, I present a fluidic interface, facilitating a combination of separation at fast liquid flow with microfluidic size and electrophoretic-mobility measurements. This method allows for a simultaneous measurement of molecule size and charge and acts as an additional chromatographic detector. I demonstrate that this method works for both label-free and labelled biomolecule characterisation and suggests ways to perform scalable mass-spectrometry analysis on a chip.

To scientific curiosity. And to my family.

Acknowledgements

My journey leading to this PhD has started purely by chance when I met Prof. Tuomas P. J. Knowles on the stairs at the Department of Chemistry. He openly invited me to visit the lab for a few minutes which subsequently extended to a few fantastic years of science. First and foremost, I would like to thank Tuomas for this opportunity, for his support, encouragement and stimulating discussions which inspired me to explore and develop as a scientist. I would also like to thank Dr Ronan Daly, Prof. Michele Vendruscolo and Sir Chris M. Dobson for their supervision and for creating a synergistic environment for cross-disciplinary research.

The Knowles lab is a group of exceptionally talented people from all over the world creating a friendly and collaborative environment for science. All of the group members have taken the time to teach me new concepts and methods, for which I am very grateful. Dr Jerome Charmet has welcomed me to the lab, introduced me to microfluidics and helped to steer my project during the early stages of my research. In particular, I would like to thank Tom Scheidt who has not only taught me a number of biophysical protein-characterisation techniques but also has challenged me to be more disciplined and consistent. Our common research efforts were very productive; I thank him for his patience and also for proof-reading this thesis. I would also like to thank Dr Simone Ruggeri for a fruitful collaboration and teaching me about surface-probe microscopy. Thanks to Kadi L. Saar, Quentin Peter, Dr Pavan K. Challa, Dr Therese Herling and Annie Chiu for sharing their expertise in programming, optics, device design and other general experimental techniques and also for making significant contributions to the work presented in this thesis. Finally, I would like to thank Tuuli Hakala, Dr Aviad Levin, Dr Janet Kumita, Dr George Meisl, Dr Marc Rodriguez-Garcia, Itzel Condado Morales, Sean Chia, Ryan Limboker, Zenon Toprakcioglu, Will Arter, and all the other members of the Center for Misfolding Diseases for great discussions and help on various aspects of research.

During the course of my research in Cambridge, I have had the pleasure of collaborating with scientists from other research groups. Victor Ostanin has taught me a lot about electronics

and sensors. Yoanna Shams has introduced me to inkjet printing, Dr Christian Bortolini introduced me to circular dichroism and Dr Maria Andreasen taught me about functional amyloid systems and their assembly on surfaces.

My PhD experience has been quite diverse, thanks to the startup companies I have been involved with. First of all, I am grateful to Fluidic Analytics for a research collaboration and welcoming me to do an internship. Dr Thomas Mueller has taught me a lot of experimental methods and tricks, provided me direction during the collaboration and introduced me to the IP world. I am also grateful to Dr Andrew Lynn, Dr Kyla Grimshaw, Dr Ashish Asthana, Dr Sean Devenish, Dr Anand Rane, Anthony Douglas and Dr Liam Dower for their support. Secondly, I would like to thank Dr Dishant Mahendru and Dr Dirk Mersch from Cambridge Innovation Consulting for inviting me to join their team with Dr Michal Wlodarski and Jeroen Verheyen where I have learnt about sales. Finally, I am grateful to Wren Therapeutics for providing me with a technology-consulting opportunity to improve their transformative drug-discovery assay.

I would also like to acknowledge the Nanotechnology Doctoral Training Centre for funding me during my doctorate and welcoming me to the Cambridge research ecosystem. The NanoDTC community broadened my scientific horizons beyond physics and introduced me to a group of bright scientists and future colleagues.

Last but not least, immense thanks goes to my family and friends. First of all, I am blessed to have my wife Elvina Petrenaitė-Kartanė by my side. I would not have gotten through this doctorate if it was not for her. Elvina was the main person who supported me at difficult times, always found a way to look out for the bright future and helped me focus on important tasks at hand. Secondly, I am very grateful to my parents who gave me everything they had for my education and allowed me to pursue my dreams. I would also like to thank my sisters Diana and Jolita, aunt Danguolė and Elvina's family for their encouragement from my early years of education till now. Special thanks to my daughter Izabelė for being patient and allowing me to finish this thesis on time. Finally, thanks to my friends Justas, Simas, Edvardas, Justinas, Šarūnas, Darius, Vladas, Arnoldas, Yelena, Miglė, Aidas, Aurimas, Antanas, Raminta, Elena and Cosmin for helping me to grow and improve as a person during my time in Cambridge.

Publications

My research here in Cambridge has resulted in a few manuscripts, which have been published, submitted or are in preparation for publication. The following manuscripts form the basis for Chapters 2 - 6:

(1) Pavan Kumar Challa, **Tadas Kartanas**, Jerome Charmet, and Tuomas PJ Knowles. Microfluidic devices fabricated using fast wafer-scale LED-lithography patterning. *Biomicrofluidics* **11**, 014113 (2017).

(2) **Tadas Kartanas**, Victor Ostanin, Pavan Kumar Challa, Ronan Daly, Jerome Charmet, and Tuomas PJ Knowles. Enhanced Quality Factor Label-free Biosensing with Micro-Cantilevers Integrated into Microfluidic Systems. *Analytical chemistry* **89**, 11929-11936 (2017).

(3) Francesco S. Ruggeri, Jerome Charmet, **Tadas Kartanas**, Quentin Peter, Sean Chia, Johnny Habchi, Christopher M. Dobson, Michele Vendruscolo, Tuomas PJ Knowles. Microfluidic deposition for resolving single molecule protein architecture and heterogeneity. *Nature communications* **9**, 3890 (2018).

(4) **Tadas Kartanas**, Tuuli Hakala, Therese Herling, Aviad Levin, Thomas Muller, Simone Ruggeri, Ronan Daly, Jerome Charmet, and Tuomas PJ Knowles. Mechanism of droplet formation in a supersonic microfluidic spray device. *Manuscript in preparation*.

(5) **Tadas Kartanas**, Tom Scheidt, Tuuli Hakala, Therese Herling, Aviad Levin, Thomas Muller, Jerome Charmet, and Tuomas PJ Knowles. Label-free gravimetric dry protein mass detection using liquid chromatography combined with QCM. *Manuscript in preparation*.

(6) **Tadas Kartanas***, Tom Scheidt*, Quentin Peter, Thomas Muller, Kadi Liis Saar, Therese Herling, Sean Devenish, and Tuomas PJ Knowles. Multidimensional protein characterisation using liquid chromatography combined with microfluidics. *Manuscript in preparation*.

In addition to the manuscripts listed above, I have also been fortunate enough to be involved in a number of collaborations with the following outcomes:

(7) Salvatore Tesoro, Kerstin Göpfrich, **Tadas Kartanas**, Ulrich F. Keyser, and Sebastian E. Ahnert. Nondeterministic self-assembly with asymmetric interactions. *Physical Review E* **94**, 022404 (2016).

(8) Christian Bortolini, **Tadas Kartanas**, Davor Copic, Itzel Condado Morales, Yuewen Zhang, Pavan K. Challa, Quentin A. E. Peter, Tamas Javorfi, Rohanah Hussaind, MD Dong, Giuliano Siligardi, Tuomas PJ Knowles, and Jerome Charmet. Resolving protein mixtures using microfluidic diffusional sizing combined with synchrotron radiation circular dichroism. *Lab on a Chip*, **19**, 50-58 (2019).

(9) Hoi Kei Chiu, **Tadas Kartanas**, Sean Devenish, Carina Luxhoj, and Tuomas PJ Knowles. High sensitivity chemiluminescent detection of proteins. *Manuscript in preparation*.

Patent applications

(10) GB 1803724.2 (application filed in 2018) Universal worm tracking platform for screening of anti-aggregation compounds.

(11) GB 1815360.1 (application filed 2018) Improvements in or relating to profiling of particles using microfluidic devices.

(12) PTC/GB2018/053583 (application filed 2018) Fluidic apparatus and methods.

Table of contents

List of figures

Abbreviations

AFM	Atomic force microscopy
BBA	Biobarcode amplification assay
BioMEMS	Biological micro-electromechanical systems
BSA	Bovine serum albumin
FFT	Fast fourier transform
GPIO	General purpose input/output
ID	Inner diameter
IFA	Immunofluorescent assay
LC	Liquid chromatography
LED	Light emitting diode
LFA	Lateral flow assay
LOD	limit of detection
MC	Microcantilever
MEMS	Micro-electromechanical systems
MRR	Microring resonator
NEMS	Nano-electromechanical systems
NMR	Nuclear magnetic resonance
NW	Nanowire
PBS	Phosphate-buffered saline
PCR	Polymerase chain reaction
PDMS	polydimethylsiloxane
PEEK	Polyether ether ketone
PGMEA	Propylene glycol methyl ether acetate
QCM	Quartz-crystal microbalance
RC	Resistor and capacitor
RMS	Root mean squared value

R&D	Research and development
SEM	Scanning electron microscopy
SMR	Suspended microchannel resonator
SPR	Surface-plasmon resonance
UV	Ultraviolet light

Chapter 1

Introduction

To invent, you need a good imagination and a pile of junk.

Thomas A. Edison, American inventor and research laboratory pioneer, 1847 – 1931

The intrinsic motivation of human endeavour is to explore the world around us. Thomas Edison, one of the greatest inventors of all times, proved that imagination is key for making progress in fundamental science and technology. The scope of this doctoral thesis was to design tools and instrumentation which may prove to be useful for studying biological systems. More specifically, I have focused on the development of biophysical techniques for quantitative protein detection and characterisation using microfluidic approaches enabled by soft-lithography.

1.1 Protein function and characterisation

Proteins, with their diverse structures and functionalities, build the machinery of life [1]. Biological processes, such as energy production and cell respiration, rely on a complex network of molecular interactions. Proteins are polymers, which consist of long and uniquely folded chains of amino-acid residues, and mediate the processes in cellular activity. However, due to the non-covalent nature of protein interactions, their reversible, and in some cases rapid, reactions are difficult to probe and challenging to describe in terms of the key physical parameters. Proteins interact with a wide range of ligands from single ions to large macromolecules. The binding specificity, affinity and kinetics of protein-ligand interactions

is governed by electrostatic, hydrophobic and van der Waals forces. The charge, size, mass and shape of a protein are, therefore, the key parameters determining protein function.

To gain their native function, proteins fold into a specific conformation [2, 3]. A detailed understanding of how proteins fold and misfold could enable progress in numerous fields, from protein engineering to disease diagnostics and treatment. Our view of the processes involved in protein folding has advanced from pathways all the way to free-energy landscapes, where the folded form not necessarily occupies the global energy minimum [4–6]. Incompletely folded proteins feature altered physical properties and interactions with other biomolecules, which can lead to protein aggregation, amyloid synthesis and malfunction. Protein amyloid deposits are found in a variety of organs and tissues, such as brain and liver, and associated with a number of disorders, e.g. Alzheimer's disease [7–9] and diabetes [10, 11]. By gaining insights into protein properties and their interactions, we can create interventions for extending the lifespan of the affected patients.

There is a number of methods for studying protein structure and function. X-ray crystallography has been applied to determine the structures of increasingly complex biomolecular systems [12]. In combination with the recent advances of cryo-electron microscopy, a large amount of structural information has been acquired [13–18]. Nuclear magnetic resonance (NMR) spectroscopy can be a source of structural as well as dynamic system information [19–21]. Atomic force microscopy (AFM) can be used for studying the mechanical properties of proteins [22, 23] as well as to reveal information about the self-assembly process of proteins [24–26]. Circular dichroism (CD) and Fourier-transform infrared spectroscopy (FTIR) are excellent methods for rapid determination of the secondary structure and folding properties of proteins [27–31]. Surface-plasmon resonance (SPR) is a common technique for studying the kinetics of biomolecular interactions and offers unique real-time label-free measurement capabilities with high detection sensitivity [32]. Finally, mass spectrometry can be used for the identification of proteins [33–35] and studying their post-translational modifications [36, 37]. However, techniques providing an experimental set-up for simultaneous measurements of multiple parameters are rare and often non-applicable for a wide variety of proteins.

Generally, analytical methods used for disease diagnostics are expensive and labour intensive [38]. To increase the throughput of diagnostic clinics, as well as to enable researchers to carry out more effective biochemistry research, new ways of process automation must be found reducing the cost, manual handling time and increasing reproducibility [39]. The recent developments in nanotechnology, micro-sensors and miniaturised detection systems have the potential to refine protein science and disease diagnostics [40]. When combined

with the existing sample preparation and characterisation techniques, nano/micro technology can help to introduce novel approaches to understanding and probing biological systems [41]. More importantly, the advanced technology should be brought closer to the point-of-care environment, especially, in low-resource settings. Producing such low-cost, fast and reliable hand-held devices would have a large impact and improve the lives of billions of people around the globe [42–44].

1.2 Micro/nano sensor devices

Mechanical interactions are fundamental to biology. Organisms, cells and biological machinery generate mechanical forces of chemical origin, not only to determine macroscopic motility and adhesion but also to influence molecular transport and affinity at the nano-scale. By probing forces [45], fluctuations [46, 47], mass [48] and concentration changes within cellular and sub-cellular processes, we can gain new insights into the biological interactions as well as detect malfunction [49]. Nano/micro-electromechanical systems (NEMS/MEMS) are particularly well-suited to probe molecular matter at an unprecedented single-molecule sensitivity.

The origins of MEMS date back to the middle of the twentieth century when Charles S. Smith published an article on stress-sensitive effects in silicon and germanium [50]. In general, during the 1950's, researchers across the world were looking to invent sensors based on the advances in the semiconductor and micro-electronics industries [51]. Since then, a number of MEMS devices have emerged for physical sensing of all sorts. From pressure [52], flow [53] and strain [54] sensors to microphones [55], gyroscopes and micromirror arrays [56], MEMS have played a crucial role in transforming automotive, mobile and aerospace industries [57]. However, even though MEMS technology has exerted a major impact on physical sensing, yet it has made a minimal impact on biochemical sensing. Analytical MEMS, often referred to as BioMEMS, Lab-on-chip or micro-TAS devices, are taking an increasingly more important role in the market, currently valued at $3 B worldwide. The demand for BioMEMS devices is growing exponentially and the standardisation of medical-device technologies enable patient monitoring at the point of need [58].

In general, NEMS/MEMS mechanical devices feature extreme resolution because the minimum detectable mass is proportional to the total mass of the sensor. Using this strategy, zeptogram-level mass resolution was achieved while operating in a vacuum environment [59] and forces of the order of 10 pN could be measured, sensitive to the breakage of an

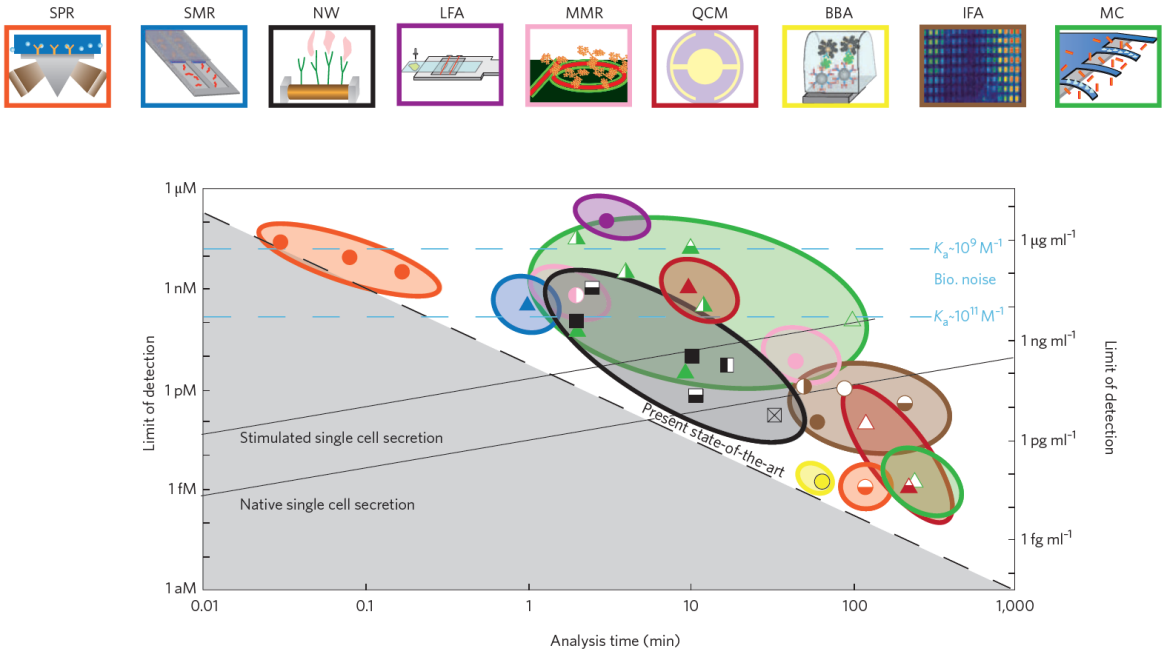

Fig. 1.1 Detection limits of biosensors versus the corresponding analysis time. An ideal biosensor offers a low limit of detection and a short duration of data acquisition. However, it can be seen that the sensitivity scales inversely with the analysis time and novel biosensors are competing with conventional immunofluorescence assays (IFAs). As we can see, a handful of sensors are now approaching the level of sensitivity that will enable real-time detection of protein secretion from individual cells. Panels at the top of the figure represent: surface-plasmon resonance (SPR), suspended microchannel resonator (SMR), nanowire (NW), lateral-flow assay (LFA), microring resonator (MRR), quartz-crystal microbalance (QCM), biobarcode amplification assay (BBA), immunofluorescent assay (IFA), microcantilever (MC). Figure reproduced from reference [60].

individual hydrogen bond [60]. Furthermore, mechanical devices exhibit fast response times, allowing for rapid process observation, suitable for fast biological processes [46]. A number of gravimetric sensors have been developed, offering varying analysis times and sensitivity ranges [60]. Microcantilevers [61], quartz-crystal microbalances [62], nanowires [63] and whispering-gallery mode resonators [64] are superior to conventional biosensors, such as lateral-flow assays and are almost sensitive enough to detect single-cell protein secretion levels. Figure 1.1 summarizes the analysis times and sensitivities of the various existing and emerging biosensing technologies.

Light trapping and enhancement achieved by plasmonic structures potentially could allow for a high density of independent sensor units to be placed in micrometre-sized arrays. They could be integrated into microfluidic chips, making nanoplasmonic devices a promis-

ing candidate for next-generation biosensors [65]. Recently, there have been a number of nanoplasmonic structure designs generated and used in various biosensing [66], nanomachinery [67] and theranostic applications [68]. Novel sensing strategies have been implemented, from high-density plasmonic nanowire [69] and nanohole [70] geometries to nanogap surface-enhanced Raman spectroscopy [71] and graphene–gold metasurface architectures [72] for ultrasensitive single-molecule detection.

The most natural sensor-biological matter interface is achieved in a fluid environment and can be split into four categories, describing the sensor and the analyte interaction: (1) high affinity-based assays, such as antigen and antibody interaction; (2) fingerprint assays relying on the analyte binding to multiple less-selective functional molecules; (3) separation-based assays where a specific fraction can be isolated from a complex mixture and detected by a sensor; and (4) deterministic assays where the mass or other properties of the molecule of interest enable its identification. However, the availability of capture molecules for a chosen disease biomarker is limited and sometimes requires large development resources. What is more, mechanical sensing in liquids is strongly affected by viscous damping, thus significantly reducing the resonator sensitivity [73, 74]. A particularly simple but effective solution addressing this issue is presented in Chapters 4 and 5, where microfluidic liquid processing is interfaced with acoustic sensing in a gaseous environment using a microfluidic spray.

1.3 Microfluidics

Microfluidics is a multidisciplinary field at the boundary between physics, life sciences and engineering and involves processes of liquid manipulation on a micron scale [75–78]. Microfluidic devices, typically featuring channels with dimensions of tens of microns, offer numerous capabilities, such as minimised sample consumption, high throughput, parallel analysis, automated operation, low cost, short experimental timescales and compact device footprints [76, 79].

The origins of microfluidics date back to the 1980's when the MEMS industry started to gain importance. This progress was combined with the advances in conventional analysis tools, new findings in the biological field and a strategic investment of the US Department of Defence in a series of programmes, aiming to develop devices and sensors for chemical and biological threats [77]. Early microfluidic approaches were adopted from the MEMS fabrication industry and silicon devices [76, 80, 81]. However, due to the opaque nature of

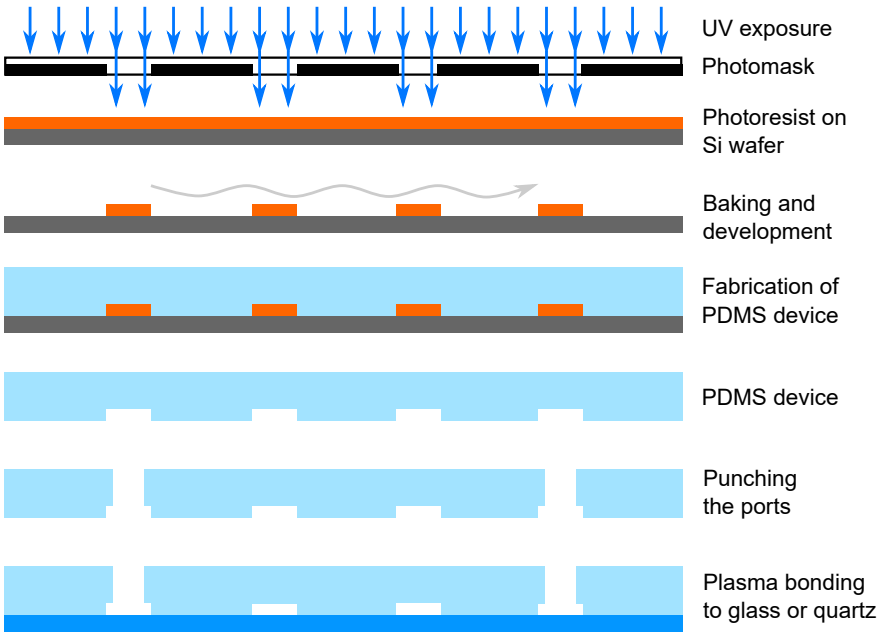

Fig. 1.2 Microfluidic device fabrication. A silicon wafer is coated by a layer of photoresist, baked and cross-linked by exposure to UV light through an acetate mask. The uncross-linked photoresist is removed by washing with developer. A PDMS device is cast on the master, ports are punched and bonded to a glass or quartz slide after cleaning.

silicon, this idea did not take hold and researchers have moved to etching channels in glass [82]. This process was slow, expensive, dangerous and, therefore, the accessibility to a large community of researchers was limited. Finally, the introduction of soft-lithography methods in the late 1990's enabled rapid prototyping of microfluidic devices and led to an increased interest in research [83–87].

Typically, microfluidic devices are fabricated in a flexible polydimethylsiloxane (PDMS) polymer using a positive mould master. The moulds are created by photolithography through transparent printable masks [84] or more recently by 3D-printing [88]. This new strategy enabled researchers within academia and industry to develop and fabricate individual devices from scratch in days rather than months [77]. These new innovations have led to a vast majority of analytical devices, featuring on chip valves [89, 90], pumps [91], separation [92, 93], mixing [94, 95], flow focusing [96], cell culturing [97, 98] and novel detection capabilities [99]. In this thesis, I have used a combination of photolithography and PDMS to prepare microfluidic devices, as outlined in Figure 1.2.

1.4 Physics and measurements at the micro-scale

The physics of fluid at the micro-scale is different to its macroscopic behaviour [75]. One of the main differences between the two regimes is mixing or the lack of it due to laminar flow. The dimensionless number, qualitatively predicting the fluid behaviour, called the Reynolds number Re, is a ratio of inertial to viscous forces. For a liquid of density ρ, viscosity η and moving at speed v within a channel of characteristic dimension L, the Reynolds number is defined as $Re = \rho v L/\eta$. Microfluidic laminar flow systems feature low Reynolds numbers, typically on the order of 10^{-6} - 10. The transition to turbulent flow occurs at Re values of 2000 - 3000, distorting the continuous-flow streamlines and causing large pressure drops [75, 78]. The full Navier-Stokes equation describing the balance of the forces acting on a small fluid element is:

$$\rho\left(\frac{\partial \boldsymbol{u}}{\partial t} + \boldsymbol{u}\cdot\nabla\boldsymbol{u}\right) = -\nabla p + \eta\nabla^2\boldsymbol{u} + \boldsymbol{f} \tag{1.1}$$

where $\boldsymbol{u}$ is the velocity, p is the pressure and $\boldsymbol{f}$ is the body force density. At low Re, the inertial forces are small compared to the viscous forces, which, as discussed above, is usually the case in microfluidic devices, and the non-linear terms in the equation can be neglected. Considering the time-independent flow, the Stokes equation applies:

$$-\nabla p + \eta\nabla^2\boldsymbol{u} + \boldsymbol{f} = \boldsymbol{0} \tag{1.2}$$

Combining it with the continuity equation:

$$\frac{\partial \rho}{\partial t} + \nabla\cdot(\rho\boldsymbol{u}) = 0 \tag{1.3}$$

gives a complete set of equations allowing to determine both analytical and numerical solutions. In the laminar-flow regime, the flow rate of the fluid through a channel Q is linearly proportional to the applied pressure difference Δp and inversely proportional to the hydraulic resistance R_{hyd} caused by viscous dissipation. Thus, the simple relationship called the Hagen-Poiseuille law, similarly to Kirchhoff's laws in electricity, enables reliable prediction of fluid flow distribution within a complex microfluidic network [76]. Using dimensional analysis, the hydraulic resistance R_{hyd} of a microfluidic channel can be expressed as:

$$R_{hyd} = \frac{\eta L}{A^2}\, C(\beta) \tag{1.4}$$

where A is the cross sectional area, L is length and $C(\beta)$ is a dimensionless, geometry-dependent correction factor [100]. In particular, soft-lithographically fabricated rectangular microchannels typically feature high aspect ratios and their hydraulic resistance can be approximated as:

$$R_{rectangle} = \frac{12\eta L}{1-0.63(h/w)}\frac{1}{h^3 w} \tag{1.5}$$

where h and w are the channel height and width, respectively ($h \ll w$).

When two fluid streams come together in a microchannel, they flow side by side along the channel, where mixing is only driven by molecular diffusion. Therefore, with the absence of active mixing or high Re, the motion of molecules can be approximated by the convection-diffusion equation:

$$\frac{\partial c}{\partial t} = D\nabla^2 c - \boldsymbol{u}\cdot\nabla c \tag{1.6}$$

where c and D are the molecular concentration and diffusivity, respectively. The lack of turbulence can be used to an advantage, and by carefully probing the molecular diffusion on chip along the flow in the channel, it is possible to estimate the molecular size of the diffusing species [99, 101, 102]. This strategy has been applied in a number of studies answering biological questions, such as protein folding/unfolding, molecular binding and assembly [101, 103–106].

Additional forces can also be applied to drive molecular motion, e.g. acoustic or electric fields. Acoustic forces have been demonstrated to perform molecular separation and sample pre-concentration [107–110]. Electric fields on chip, however, open an even bigger variety of phenomena, such as electrophoretic mobility, electroosmotic flow and dielectrophoresis [111–115]. Such devices have been used to separate proteins [116], study molecular interactions [117], determine protein charges [106, 118] and differentiate cancerous cells [119, 120]. By combining conventional liquid chromatography with diffusional sizing and electrophoresis measurements, I demonstrate in Chapter 6 that this approach is a reasonable strategy for a scalable "mass-spectrometer on a chip" platform which could help to characterise protein mixtures under native conditions.

Microfluidic devices can also feature unique physics at high Reynolds numbers. For example, in a flow-focusing scenario, mixing two immiscible fluids with a high interfacial surface tension results in drop formation [121–123]. Such setups, generating thousands of micrometer-sized drops, can be utilised in platforms, from more sensitive PCR assays due to the enhanced molecular concentration [124–126] to frameworks for studying the physics of

self-assembly [127] and single-cell encapsulation and sorting [128, 129]. The latter approach has been applied for single-cell transcriptomics to characterise thousands of individual cells in a single experimental procedure [41, 130] and has recently led to the discovery of new cell types [131]. Finally, high-*Re* number flow exhibits a non-negligible inertial force. When fluid undergoes a curved section of a channel, secondary flows, called Dean vortices, are formed [132, 133]. This phenomenon has been utilised for enhancing fluid mixing and inertial particle focusing [133].

Yet another microfluidic high-*Re* number application is realised by mixing gas and liquid on a chip. This strategy has been used for mixing enhancement [96], microbubble generation [134, 135] or aerosol spray formation [136, 137]. In the latter example, Amstad et al. [136] have demonstrated supersonic gas velocity generation on a chip which was utilised for sub-micron drop generation, leading to amorphous nanoparticle production. I have used a similar approach to generate micron-sized drops, resulting in a controlled drop deposition on a surface, as described in Chapter 3.

There is "*plenty of room at the bottom*", as once stated by Richard P. Feynman. He hypothesised back in 1959 [138, 139] that we could create tiny machines of order of tens of atoms that could do things we had not yet imagined. After almost 60 years, we are not only able to build nanometer-sized machinery but also can manipulate single atoms [140, 141] and use nanoscale structures for various applications, such as nanopore sensing [142–144] which is revolutionising DNA sequencing [145]. Researchers have already been exploring the possibility of shrinking the Lab-on-chip systems even further [146]; however, rapid nanoscale fabrication methods are still limited [147]. Most of the nanofluidic structures are fabricated using techniques such as electron-beam lithography or AFM which are slow and non-scalable. When we approach the dimensions close to the Debye layer, electrostatic and entropic forces start to be more important [148–150]. Major scientific and technological breakthroughs in the understanding of the phenomena at nanoscale lie ahead of us.

However, as fundamental science and technological proof-of-concept studies develop, other important aspects must be addressed for making the technology available for non-technical specialist audiences by a route of commercialisation.

1.5 Future of Lab-on-chip systems

Although the advances in the microfluidic technology have been acknowledged, one of its entrepreneurs, George M. Whitesides, has raised some critical points about the future

of microfluidics [77]: "*Why is every biochemistry laboratory not littered with labs on chips? Why does every patient not monitor his or her condition using microfluidic home-test systems?*" In this section, I will briefly review what has been achieved at the proof-of-concept stage and beyond to mature the platforms into industrial-grade technologies.

Perhaps the most ubiquitous application of Lab-on-chip systems is in medical diagnostics. Devices would fit in the palm of a hand, be cheap and easy to mass produce, and require only a drop of blood to carry out the diagnosis. Some basic approaches have already been generated and implemented in practice for the diagnosis of infectious diseases [151], measuring glucose levels in body fluids [152] or cancer-cell analysis [153]. There is also a large community of molecular biologists already using and adapting novel analytical systems. Some examples include enzymatic-reaction screening, reaching a 1,000-fold increase in throughput compared to conventional approaches [154], or generation of protein-interaction networks, performing almost 15,000 experiments and probing over 150 interactions between 43 proteins [155].

The proof-of-concept platform transfer to commercial settings usually takes between 20 to 30 years and experiences high expectations followed by unfulfilled promises. This phenomenon can be described by the Gartner Hype [156] and the Product Life cycles [157]. Initial research, conducted typically in an academic environment, generates a wide public interest, leading to unreasonable expectations such as " *building a carbon nanotube space elevator*" [158]. However, due to unanticipated difficulties in technology research and development (R&D), societies have come to realise that the future they had envisioned is still inaccessible; the excitement drops. Eventually, determined industrial efforts to overcome the engineering challenges are successful, the costs are reduced and the high-value large-scale applications spread around the world, maturing the technology. The phenomenon is summarised in Figure 1.3.

A decade after the famous article by George M. Whitesides [77], have we progressed from being just excited about Lab-on-chip systems? According to market reports, microfluidics as a technology platform is at a stage of continuously increasing market adoption - the so called "*Slope of Enlightenment*" [159]. The valuation of the microfluidics industry as of 2017 was at $2.5 B, with an annual growth rate of 18%. With the high end-user demand for increasingly automated, integrated and miniaturised disease diagnostics and treatment planning, the industry market is forecasted to reach the $5.8 B mark by 2022. The company ecosystem seems to grow strong with a number of small companies enabling the prototyping research community (Elveflow, Fluigent, Microfluidic ChipShop), companies providing industrial-scale chip manufacturing capabilities (uFluidix, Micronit, thinXXS), modern gene-

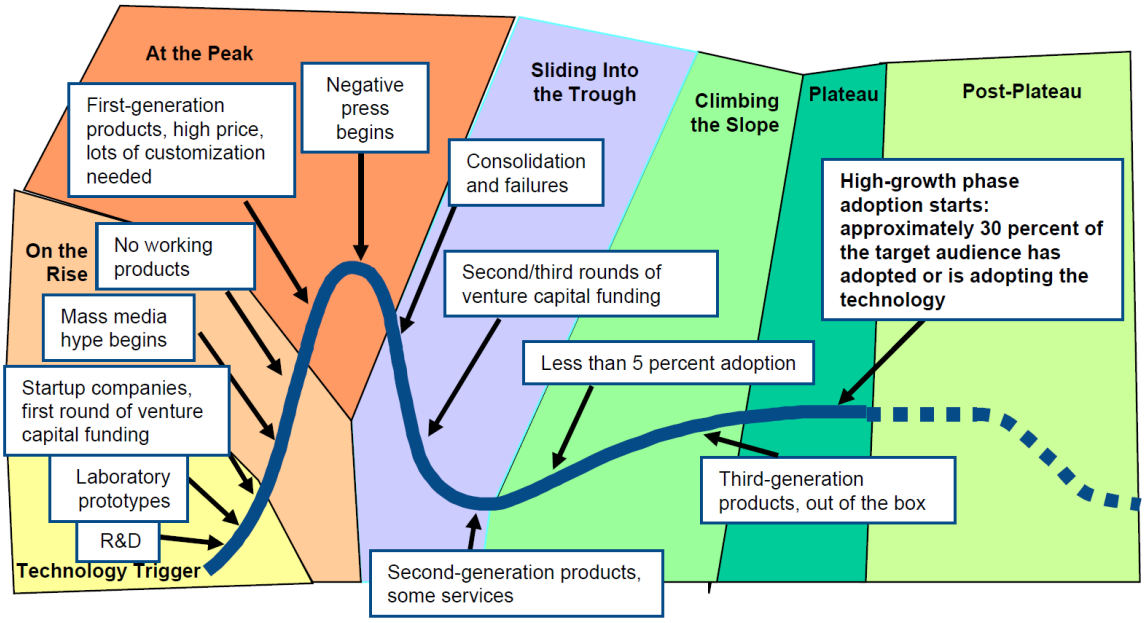

Fig. 1.3 Phases of the technology Gartner Hype Cycle. The initial research acts as a "Technology Trigger" and is followed by a "*Peak of Inflated Expectations*". Then the technology drops to the "*Trough of Disillusionment*" where most likely it fails. However, if the invention is successful and gains trust, it rises again through the "*Slope of Enlightenment*" until, finally, reaching the "*Plateau of Productivity*". Figure reproduced from reference [156].

sequencing corporations (Illumina), automated-process providers (Fluidigm) and diagnostics companies (Cepheid, Roche, Agilent, PerkinElmer). The latter are racing to acquire the emerging microfluidic-technology startups and include more automation in their already existing diagnostic-platform portfolio.

However, the microfluidic industry is at its early "*Scale*" stage and still has about 15-20 years to reach the "*Plateau of Productivity*" [159]. Engineering solutions are emerging for making the systems genuine labs on chips. The instruments now include steps all the way from cell culture, sample preparation and protein purification to fluidic handling and MEMS detection. Therefore, to my understanding, George Whitesides' concerns have been addressed and the industry is going in the right direction. However, the biggest widespread applications and technology giants in the area remain to be seen.

1.6 Summary of the thesis

Based on the research described in this thesis, I have aimed to develop microfluidic methods for quantitative studies of molecules in solution and dry phase. One of my main objectives was to establish multiple interfaces between microfluidic flow handling and micro/nano sensors, standard protein-characterisation and separation methods. This combination is an inevitable step which has to be achieved in order to develop new tools to answer biophysical problems.

Chapter 3 describes the development of a microfluidic spray nebuliser, able to transfer biomolecules from liquid to dry phase. By using high-speed imaging, I am able to observe how the spray nozzle works and identify its ideal operation conditions. Then, I demonstrate the capability of controlling the drying time of the drops, leading to millisecond-scale attachment of biomolecules on surfaces. I validate this strategy for atomic force microscopy studies and demonstrate the ability to investigate protein-oligomer and aggregate systems.

In Chapter 4, I show that the ability to transfer biomolecules to a dry phase in a controlled way can be used to advantage when detecting the molecules in an atmospheric environment with MEMS cantilevers. The custom-built cantilever resonant-frequency monitoring platform is shown to avoid viscous damping effects in liquids, leading to a limit of detection of 370 femtogram. Using this system, I show detection of inorganic salts and standard proteins. Finally, by incorporating a calibration step before the spray deposition, I demonstrate the ability to determine the concentration of protein solution in a label-free manner.

Measurement selectivity in microfluidic platforms is usually achieved by a labelling step, enhancing the readout sensitivity. However, we rely on the availability of molecular labels as well as the risk that biomolecular properties, such as mass, size and charge, are affected. Protein separation can greatly improve on the measurement specificity. Chapter 5 presents a strategy to interface standard bulk-flow protein separation with label-free MEMS sensing for a selective protein-mass measurement. I demonstrate that this sensitive approach can characterise mixtures down to concentrations as low as 1 µg/mL.

Liquid chromatography, combined with analytical microfluidics, establishes diverse opportunities for protein characterisation of the molecules which are being purified. In Chapter 6, I describe a scalable interface between bulk-flow separation and a multidimensional microfluidic analysis platform. To this effect, I can characterise protein mixtures and determine the key biophysical properties of individual mixture components after their separation. This strategy is demonstrated to work for both label-free and fluorophore labelled proteins.

In the preparation of Chapters 3 - 6, I have aimed to make these sections relatively self-contained, so that they can be read independently or as a part of the whole thesis.

Chapter 2

Method of rapid prototyping in microfluidics

2.1 Device design

The microfluidic-device designs were created using the educational Autodesk AutoCAD software package. The devices typically feature channel dimensions anywhere from 10 μm to a few 1000 μm. Kirchhoff's circuit laws were applied for the prediction of the relative fluid flows in neighbouring channels. Device designs were printed on acetate for use as the fabrication masks (Microlithography Serives Ltd, UK).

To maximise the microfluidic device operational success, the following design considerations should be made. First of all, the important feature sizes should be larger than 5 μm and, ideally, larger than 20 μm. Also, the spacing between the nearby features should be larger than $20-30$ μm; otherwise, it takes a lot of time and effort to develop the photoresist from the gaps. Secondly, the feature aspect ratio should be less than two (height over width) because they may peel into the PDMS during the soft-lithography step. Finally, one should note that the hydraulic resistance of a long channel on a chip will have quite a large uncertainty due to the limitations of this rapid prototyping approach. The spin-coated photoresist layer results in errors of up to ± 10 % which, subsequently, translates into a ~ 30 % error in the absolute value of hydraulic resistance ($R_{hyd} \sim 1/h^3$). However, this is normally not an issue as all of the *resistors* on a chip are scaled accordingly. On the other hand, this may be a serious issue when PDMS devices are interfaced with other systems of a well-defined hydraulic resistance. In such cases, the heights of the individual devices should be measured.

2.2 Soft-lithography mould fabrication

2.2.1 Affordable UV-LED lithography platform

This platform previously appeared in:

*Pavan Kumar Challa, **Tadas Kartanas**, Jerome Charmet, and Tuomas PJ Knowles. Microfluidic devices fabricated using fast wafer-scale LED-lithography patterning. Biomicrofluidics **11**, 014113 (2017).*

A custom built setup was used for UV lithography. The instrument was based on a UV-LED (Thorlabs M365LP1) with the maximum power of about 1000 mW. The LED was powered by an LED Driver (Thorlabs LEDD1B). The driver output was set to a constant current of 1.2 A. The exposure time was varied by setting the driver into an external trigger mode with the trigger input controlled by a general purpose input/output (GPIO) pin on a Raspberry Pi 3. A custom Python-based graphical user interface was developed allowing the user to change the exposure time and start the illumination. Raspberry Pi was connected to a 7 in. touchscreen monitor for user friendly input and control. Even though Python is not a real-time programming language, variability in the timing of the order of 1 ms, typical to GPIO pins, did not represent an issue for exposure times in the range of 30 s. An aspheric condenser lens of focal length 60 mm (Thorlabs ACL7560U) was positioned 60 mm from the LED. The lens was positioned 210 mm above the exposure surface. For single-layer patterning, when no alignment was necessary, the wafer was placed at the bottom of the exposure plane. When multilayer devices were fabricated, a mask-aligner was used. The total cost of the platform was only around £1000. The setup is depicted in Figure 2.1.

2.2.2 Single-layer mould master fabrication

To begin with, approximately 3 mL of SU-8 3000 series photoresist (MicroChem Corp.) was pipetted onto a circular 3 inch silicon wafer (PI-KEM, UK). It was subsequently spin-coated evenly on the wafer using a SCS G3 series spin coater (PI-KEM, UK). The total spinning procedure consisted of three steps: (1) spreading the photoresist at 500 rpm, then (2) accelerating the rotor until the terminal speed and (3) maintaining the rotation for 30 s. The terminal spin speed depends on the chosen photoresist type, the desired thickness and ambient conditions. SU-8 3025 and 3050 photoresists were used to create 25 micron and 50 micron thick layers, respectively, using a spin speed of 3000 rpm. After the coating, the wafer was soft-baked at 96° C for 12 (SU-8 3025) to 25 (SU-8 3050) minutes. Following this, the

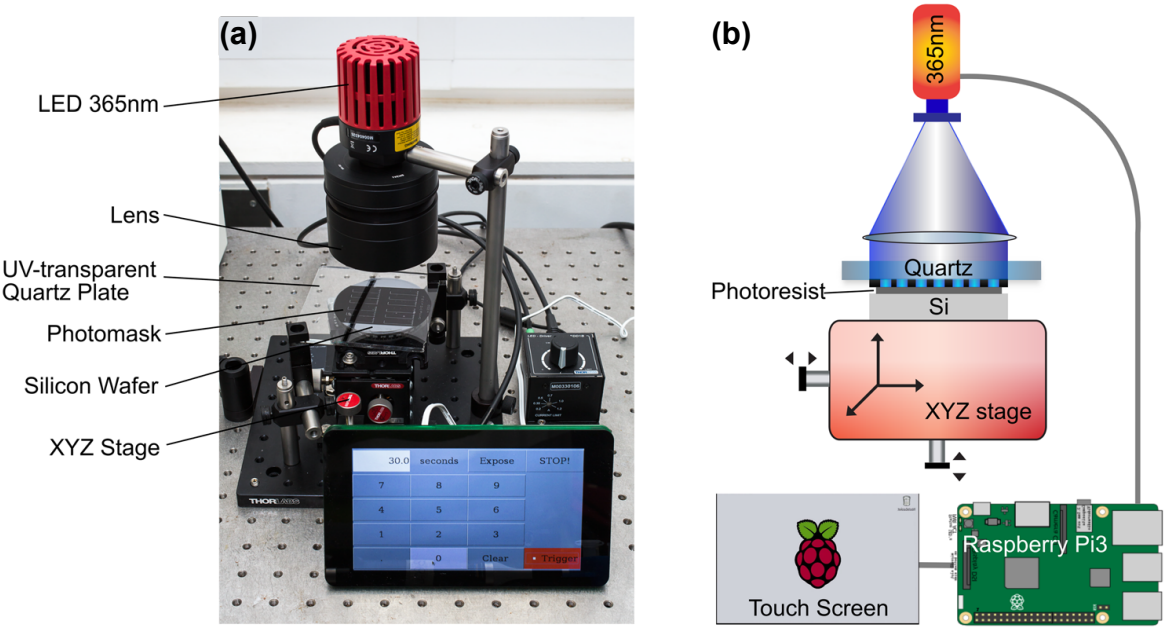

Fig. 2.1 Custom-made UV exposure setup. (a) The UV-LED lithography platform uses an inexpensive commercially available UV-LED as the light source. The collimated light beam was turned ON/OFF with a custom-designed user-friendly Raspberry Pi application. (b) Schematic diagram of the optical and electronic setup.

acetate mask, patterned with the desired design, was fixed to the wafer using a clamp. The wafer was then illuminated by the UV light source, described in Section 2.2.1, for 30 s. The lithography was relatively sensitive to this step, and if the exposure time was much longer or shorter than the expected exposure dose, the features risked being not well-resolved. After the exposure, the wafer was baked for 5 minutes, which cross-linked the exposed photoresist regions. Finally, the uncrosslinked SU-8 was removed using propylene glycol methyl ether acetate (PGMEA). The wafer was placed in a glass container, filled with PGMEA until the wafer was fully submerged and agitated for 5 to 10 minutes, depending on the device thickness. Finally, it was rinsed with fresh PGMEA, isopropyl alcohol and blown dry with nitrogen, before being stored in a covered Petri dish. The result of this was a positive master patterned with photoresist of constant thickness.

2.2.3 Multilayer mould master fabrication

To fabricate microfluidic devices with 3D features, we used a multilayer photo-lithography approach. The core lithography steps remained as for the single-layer lithography, with the addition of aligner marks included on the device designs as well as the mask aligning

procedure. First, the device features of smaller height were developed as normal. Then, the mask-aligner marks were taped and the second photoresist layer was spin-coated. After the soft-bake step, the tape was peeled off, exposing the mask-aligner marks. Then the second mask was positioned above the wafer with a mask-aligner, exposed to UV light and the uncrosslinked photoresist was developed in PGMEA. These steps could be repeated multiple times.

2.3 PDMS device fabrication

2.3.1 Soft-lithography

The silicon wafer, patterned with SU-8 features, was then covered with PDMS (Sylgard 184, Dow Corning), which was mixed with cross-linker in a 10:1 ratio before being degassed for 15 min, and then baked for 1-2 h at 65° C. Longer baking times are possible, but it makes PDMS more brittle. The functional part of PDMS was then removed from the reusable mould master using a scalpel. Inlets, connecting to the channels, were made with a 0.75 mm biopsy punch (World Precision Instruments) and the device was sonicated in isopropyl alcohol and blown dry.

2.3.2 PDMS device bonding

To seal the microfluidic devices with glass, quartz or another PDMS layer, I used a Diener Electronic Femto oxygen plasma oven. This part of the process was sensitive to small changes in the settings. In this case, the power was set to 40 % with the gas flow rate of 5 sccm at a pressure of 2 bar. The exposure time was 10 s for bonding PDMS to glass, 30 s for PDMS to quartz and 30 s for PDMS to PDMS surfaces. PDMS-quartz and PDMS-PDMS devices were placed on a hotplate with 96° C for 10 min to ensure complete bonding. To minimise the background signal during fluorescence experiments (as for devices used in Chapter 6), I mixed a small amount of carbon nano-powder (Sigma, UK) into the PDMS prior to curing. Pictures of the most important fabrication steps are shown in Appendix A. Also, a troubleshooting guide for microfluidic experiments is given in Appendix B.

2.3.3 Device treatment

To avoid sample sticking or to improve the device operation, the devices need a post-treatment. The surface of the channels can be made hydrophobic by Aquapel (Aquapel Glass Treatment, USA) or trichlorosilane (Sigma, UK) treatment. To make devices more hydrophilic and less prone to sample sticking, the devices can be exposed to 80 % oxygen plasma for 500 s, carried out after the device bonding.

2.4 Accessories for microfluidic device development

2.4.1 Fluidic connectors

To interface the microfluidic chips with glass syringes (Hamilton, USA), I used bent metal tips (FIS5601169, Fisnar USA), connected to the chip port on one end and polyethylene tubing with 1.52 mm outer diameter on the other end (800/100/280, Smiths Medical Portex ,USA). Also a narrower tubing of 0.96 mm outer diameter (800/100/200, Smiths Medical Portex, USA) can be used; however, the devices are more likely to leak.

2.4.2 Syringe pumps

A number of syringe pumps could be used, depending on the required precision of flow stability. The most widespread pumps used in the field are neMESYS (CETONI GmbH, Germany) and Harvard PHD2000 (Harvard Apparatus, USA) syringe pumps. However, for simple flow-cell type experiments, cost-effective NE-300 pumps (Pump Systems Inc., USA) are sufficient. Care must be taken to prime the syringes before use to ensure that there are no air bubbles.

2.4.3 Pressure pumps

Fluid flow, driven by a pressure source rather than a flow source (syringe pump), is typically more stable. Due to the elastic properties of PDMS, tubing and syringes, the syringe-driven flows stabilise in $\sim$ 1 min, in contrast to $\sim$ 20 ms for the pressure-driven flows. MK3 (Elveflow, France) or LINEUP (Fluigent, France) pressure pumps are the most common examples.

2.4.4 Flow sensors

To optimise the device operation, flow sensors can give invaluable information of the flow magnitude and stability. I used user-friendly sensor kits MFS (Elveflow, France); however, one can incorporate cost-effective flow sensors with typically analogue readouts (e.g. SLx Series, Sensirion Holding, Switzerland).

Chapter 3

Supersonic microfluidic spray nozzle for a controlled surface-spray deposition

3.1 Summary

Spray-drying, employed in automotive, food and pharmaceutical industries, is a robust and cost-efficient liquid atomisation technique offering control over the droplet size. However, the majority of the commercially available spray nozzles are designed for large-throughput spray-drying or uniform surface spray coating. Here, I present a microfluidic spray nozzle for 4-10 μm drop generation. This is achieved through a supersonic choked nitrogen-gas flow through a microfluidic constriction, introducing high shear stresses to the emerging liquid jet. In this chapter, I describe the essential conditions for a choked flow, required to form drops evaporating in less than 10 ms. Then, I characterise the spray operation and compare the measured distribution with the expected drop size. Furthermore, I investigate the different droplet drying regimes in flight and upon landing on the surface and establish the drop-drying time to the spraying-distance relationship. Finally, I illustrate how the spray nozzle can be used for heterogeneous protein sample deposition on a scanning-probe microscopy imaging substrate.

Parts of this work previously appeared in:

***Tadas Kartanas**, Victor Ostanin, Pavan Kumar Challa, Ronan Daly, Jerome Charmet, and Tuomas PJ Knowles. Enhanced Quality Factor Label-free Biosensing with Micro-Cantilevers Integrated into Microfluidic Systems. Analytical chemistry **89**, 11929-11936 (2017).*

Francesco S. Ruggeri, Jerome Charmet, ***Tadas Kartanas****, Quentin Peter, Sean Chia, Johnny Habchi, Christopher M. Dobson, Michele Vendruscolo, Tuomas PJ Knowles. Microfluidic deposition for resolving single molecule protein architecture and heterogeneity. Nature communications* ***9****, 3890 (2018).*

3.2 Introduction

Material deposition on surfaces is key for many applications, such as polymer electronics [160], drug delivery [161], chemical protection [162], solar cells [163], nanoparticle processing [164] and medical diagnostics [165]. Currently available techniques for surface drying the active material are aerosol/pneumatic spraying [166], inkjet printing [167] and electrospray [168], making use of shear, acoustic and electric driving forces, respectively. Even though inkjet printing offers by far the most control over the generated droplet size [169], it is a relatively low-throughput technique with large dead-volumes and often requires additives for the liquid to be deposited [170].

Aerosol spray, however, can be much higher throughput and is used in a range of industries from food powder production [171] to cosmetic [172] and pharmaceutical nanoparticle generation [173]. Typical commercially available nozzles generate droplets of the order of the nozzle dimension [174] with diameters between 3 µm and 100 µm [175, 176]. By contrast, recently developed microfluidic spray devices can produce drops with diameters ranging from 300 nm to 10 µm, which is smaller than their characteristic orifice size [136]. The droplet makers feature liquid introduction into a narrow constriction, pressurised by air or nitrogen gas with relative pressures between 0.1 bar and 3 bar. The spray devices have been shown to operate in a jetting regime at low pressures to create drops with monodisperse/polydisperse distributions [177]. In such cases, the drop breakup was induced by the Rayleigh-Taylor instability creating surface waves, eventually developing into drops [178]. The small droplets evaporate more quickly due to the increased surface-to-volume ratio and, therefore, have been used for amorphous nanoparticle formulation [136, 179], femtosecond X-ray crystallography [177] and mass-spectrometry [180], aiming to dry the formed drops in-flight. However, droplet delivery to surfaces and the drying time on the deposition substrate have never been explored with these nozzles.

In this chapter, I describe how aqueous airborne micron-sized drops are generated inside a supersonic microfluidic spray device, depicted in Figure 3.1. I demonstrate how the gas pressure influences the device operation and measure the generated drop-size distributions.

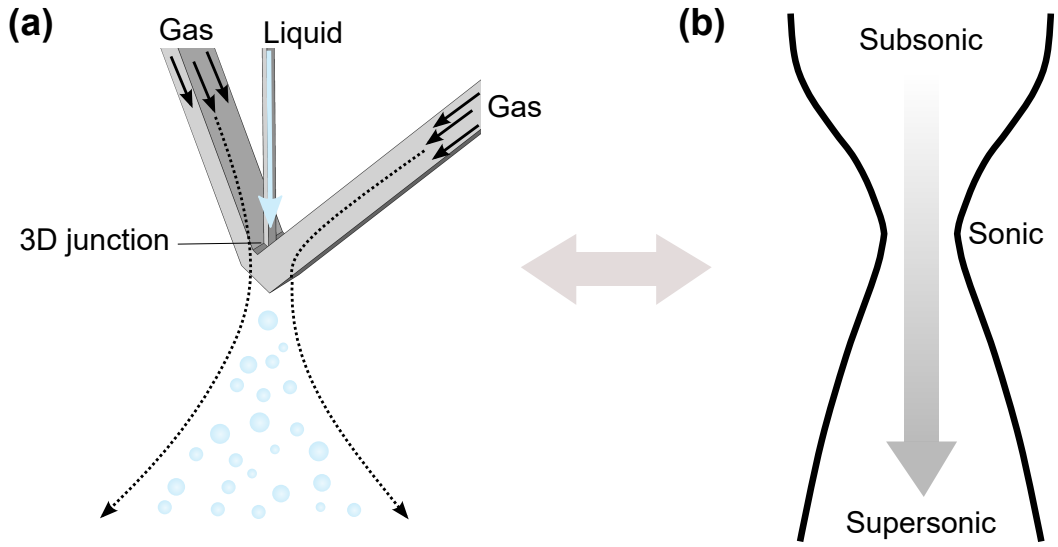

Fig. 3.1 Supersonic microfluidic-spray nozzle. a) Schematic of the 3-dimensional nozzle atomising the liquid with a supersonic pressurised gas flow through a constriction. b) The gas flow through the device can be explained using the de Laval converging-diverging nozzle model. The gas flow within the microfluidic device is choked, reaching sonic speeds at the device throat. Subsequently, gas is accelerated to supersonic speeds due to the rapid pressure drop at the nozzle outlet. This setup causes atomisation of the liquid, which is continuously introduced at the nozzle throat. The 3-dimensional junction avoids liquid contact with the spray orifice.

Moreover, I investigate the drop-drying mechanisms and estimate that the deposited sessile drops evaporate in 1 - 9 ms after landing on the surface. Finally, the spray device is used for depositing 140 nL of heterogeneous protein solution on mica for atomic force microscopy imaging.

3.3 Materials and methods

3.3.1 Microfluidic-spray nozzle fabrication

The nozzle design and initial experiments were carried out by Dr Jerome Charmet.

The devices were fabricated using a standard polydimethylsiloxane (PMDS) soft-lithography approach [86, 181]. The masters for the replica moulding of PDMS were produced with a 2 step SU-8 photolithography process, as described in Section 2.2.3 and depicted in Figure 3.2a. The first master consisted of a two-mask design comprising a 20 µm $\times$ 25 µm solution

channel and a second layer with 50 µm × 100 µm channels for the gas. The second master has only the gas channels. After mixing PDMS and casting it onto the lithography masters, it was cured at 65° C for 2 h. The PDMS replica of each master was then cut, and the connection holes were formed with the help of a biopsy punch. The PDMS parts were sonicated for 3 min in isopropanol, blow dried with N_2, and placed in an oven at 65°C for 10 min. The two PDMS elements were then activated using O_2 plasma (Diener etcher, Femto, 40% power, 30 s) and put in contact with each other, after a drop of methanol had been deposited on one of the surfaces. The methanol was used to give enough time before the bonding took place to position the features precisely [182, 183], such that the two gas-transporting channels are aligned. The PDMS device was then cut at the nozzle outlet with a razor blade. Finally, the sealed chips were plasma bonded to a clean glass slide and were ready to use. Figure 3.2b shows an optical image of the fabricated devices. A controlled flow of 100 - 300 µL/h rates was driven through the solution inlet using a syringe pump (Harvard Apparatus PHD2000). The other inlet was connected to a pressurised N_2 cylinder with a pressure regulator able to achieve pressures of 0 - 5 bar; however, typically 3 bar pressure was used for spray atomisation. A colour-enhanced picture is shown in Figure 3.2c. This fabrication strategy gave a yield of 50 % successful devices.

3.3.2 Droplet-size measurement

The size distribution of drops, generated by the spray nozzle, was measured using a Spraytec laser-scattering system (Malvern, UK). The measurement integration time was 10 s during the continuous spray operation. The nozzle was held 2 cm above the laser beam.

3.3.3 Preparation of monomeric Aβ42 and α-synuclein solution

These sample-preparation procedures were developed and carried out by Sean Chia.

Solutions of Aβ42 were prepared by dissolving the lyophilized protein in 6 M GuHCl. Monomeric forms were purified from the presence of potential oligomeric species and salts using a Superdex 75 10/300 GL column (GE Healthcare) at a flow rate of 0.5 mL/min, and were eluted in 20 mM sodium phosphate buffer, pH 8 supplemented with 200 µM EDTA and 0.02% NaN_3. The centre of the peak was collected and the Aβ42 concentration was determined from the absorbance of the integrated peak area using $\varepsilon_{280}v = 1490\,\mathrm{L\,mol^{-1}cm^{-1}}$ [184]. Recombinant α-synuclein was synthetized in E. coli and then purified by previously accepted protocols [185]. The monomeric protein samples were filtered (>95%) in a 50 mM

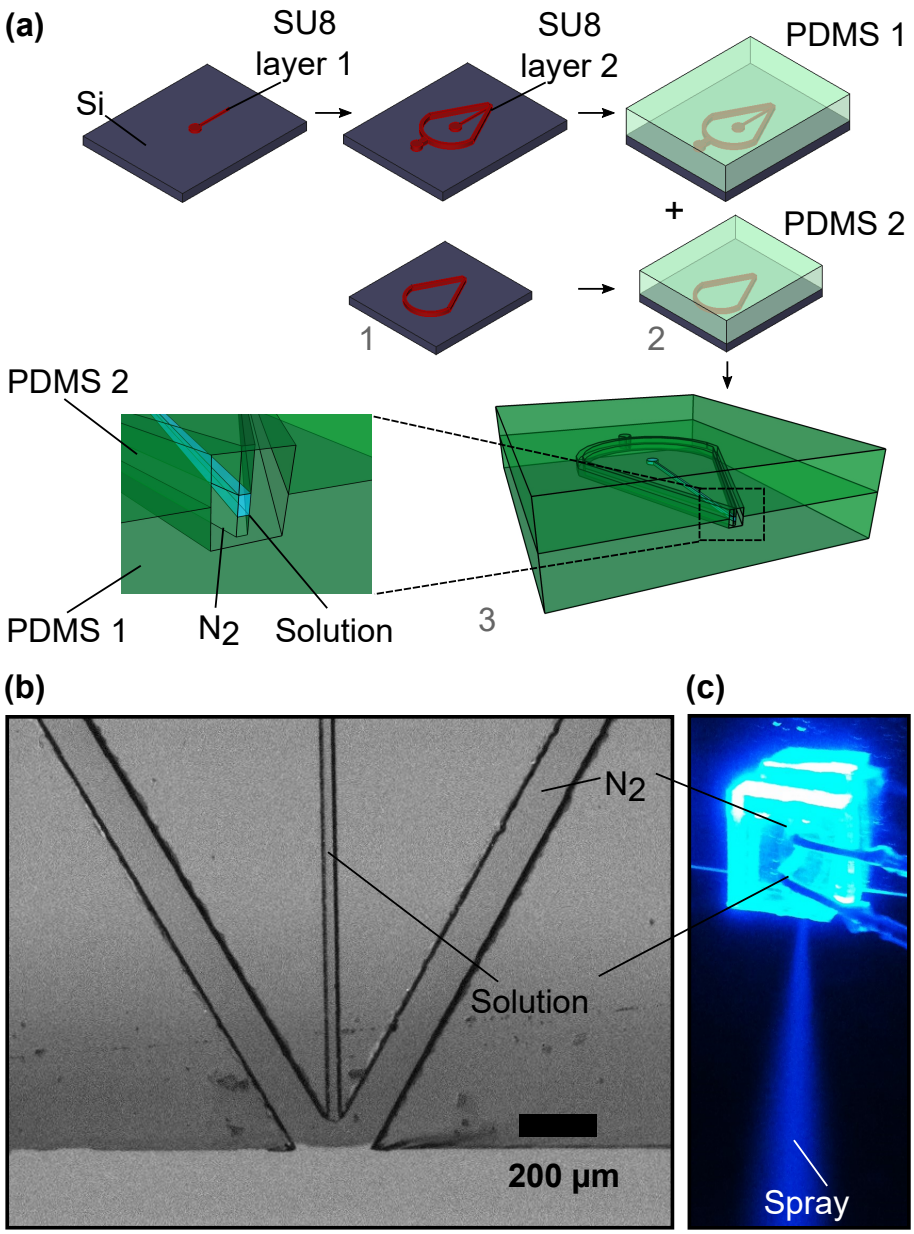

Fig. 3.2 Supersonic microfluidic spray nozzle. The liquid droplets are generated at the device outlet where the fluid channel is surrounded by gas flow from all directions. (a) The general fabrication steps consist of two-layer photolithography (step 1), soft-lithography of two parts (step 2), and assembly (step 3). (b) An optical image of the spray nozzle which has two inlets: one for a liquid to be sprayed and another for an inert gas. (c) A picture taken during the continuous device operation.

TRIS buffer, NaCl 150 mM, 7.5 pH and incubated at 37° C to form prefibrillar and fibrillar aggregates. The solutions were subsequently loaded into a syringe and a volume of 140 nL was spray deposited on a mica surface at a flow of 100 µL/h in 5 s for AFM imaging at a distance of 4 cm away from the surface.

3.3.4 AFM measurements

The AFM measurements and analysis were carried out by Dr Francesco Simone Ruggeri.

Atomic force microscopy was performed on a mica substrate. AFM images were acquired with NX10 (Park systems) and a Nanowizard 2 (JPK) systems operating in tapping mode and equipped with a silicon tip (µmasch, 2 N/m) with a nominal radius of 10 nm. Image flattening and statistical analysis were performed by SPIP (Image Metrology) software.

3.4 Results and discussion

3.4.1 Supersonic gas-flow model

I used the choked-flow de Laval nozzle model to explain the operation of the spray device [186]. The flow of gas, at an upstream stagnant pressure p_0 through the narrow constriction (microfluidic channel in our case) into a wide exit at a pressure p_e, depends on the pressure difference, $\Delta p = p_0 - p_e$. At low pressure differences, Δp, the flow could be approximated as laminar; however, on increasing Δp, the gas velocity increases at the nozzle throat until it reaches the local speed of sound and chokes the flow [186]. Further increase of the upstream pressure p_0 would result in an increased flowing gas density at the throat but with a speed still limited by the sonic limit.

The critical pressure difference for the choked flow to occur is when p_e is lower than the critical pressure p_c given by [187]:

$$p_c = p_u \left(\frac{2}{\gamma + 1} \right)^{\frac{\gamma}{\gamma - 1}} \tag{3.1}$$

where $\gamma = c_p / c_v$ is the ratio of constant-pressure and constant-volume specific heats of the gas. For nitrogen and air, $\gamma = 1.4$, giving $p_c = 0.528 p_0$. Hence, for a spray nozzle, operating

under normal atmospheric conditions $p_e = p_a = 1$ bar, choked flow will occur if $p_0 > 1.9$ bar or $\Delta p > 0.9$ bar. We usually operate the nozzle at Δp between $2-3$ bar; therefore, for normal supersonic spray nozzle operation, the gas flow is choked.

The sonic gas flow experiences sudden divergent expansion just outside the nozzle throat, thus achieving supersonic speeds at the vicinity of the nozzle orifice. The linear velocity v_e of the gas exiting the nozzle under the assumption of an ideal gas behaviour [188] is:

$$v_e = \sqrt{\frac{RT}{M} \cdot \frac{2\gamma}{\gamma - 1} \cdot \left[1 - \left(\frac{p_e}{p_u}\right)^{(\gamma-1)/\gamma}\right]} \tag{3.2}$$

where v_e is the gas exit velocity, R is the universal gas constant, M is the gas molar mass. Using the relationship above, we estimate the nitrogen gas maximum exit speed to be $v_{3bar} = 450$ m/s under the usual spray operating condition ($\Delta p = 3$ bar). As soon as the supersonic gas jet exits the nozzle, it experiences a sonic shock wave, leading to a sudden pressure and density change, thus introducing high shear forces to the emerging liquid jet.

3.4.2 Spray operation

In this section, I investigate the nozzle operation. The nitrogen pressure at the device gas inlet was controlled with a pressure regulator and water solution was injected into the nozzle with a syringe pump. To visualise the drop formation at the nozzle, I used a high-speed camera (V310, Phantom, USA) operated at 25,000 frames per second and 1 µs exposure time. The imaging was first done by focusing the camera inside the device (see Figure 3.3a). I observed that the spray was operating in a dripping mode: first, a drop of $30-50$ µm built up at the gas-stagnation point until it was large enough and the drag force due to the sonic gas flow formed a liquid jet. The frequency of droplet formation at $Q = 100$ µL/h and the pressure 2 bar was around 700 Hz. By measuring the diameter of the emerging liquid stream on the high-speed images, I could also estimate the average liquid jet to have a diameter of $d_{jet} \approx 10$ µm.

To observe the jet-to-droplet transition during a jetting event, the camera was focused outside the device just below the nozzle orifice. The pressure at the gas inlet was varied between 0.4 bar and 2 bar and the jet break-up was observed, as shown in Figure 3.3b. Qualitatively, I observed a transition from a few large generated drops at a pressure of 0.4 bar to multiple, much smaller spray droplets due to the supersonic shock-wave front at pressures higher

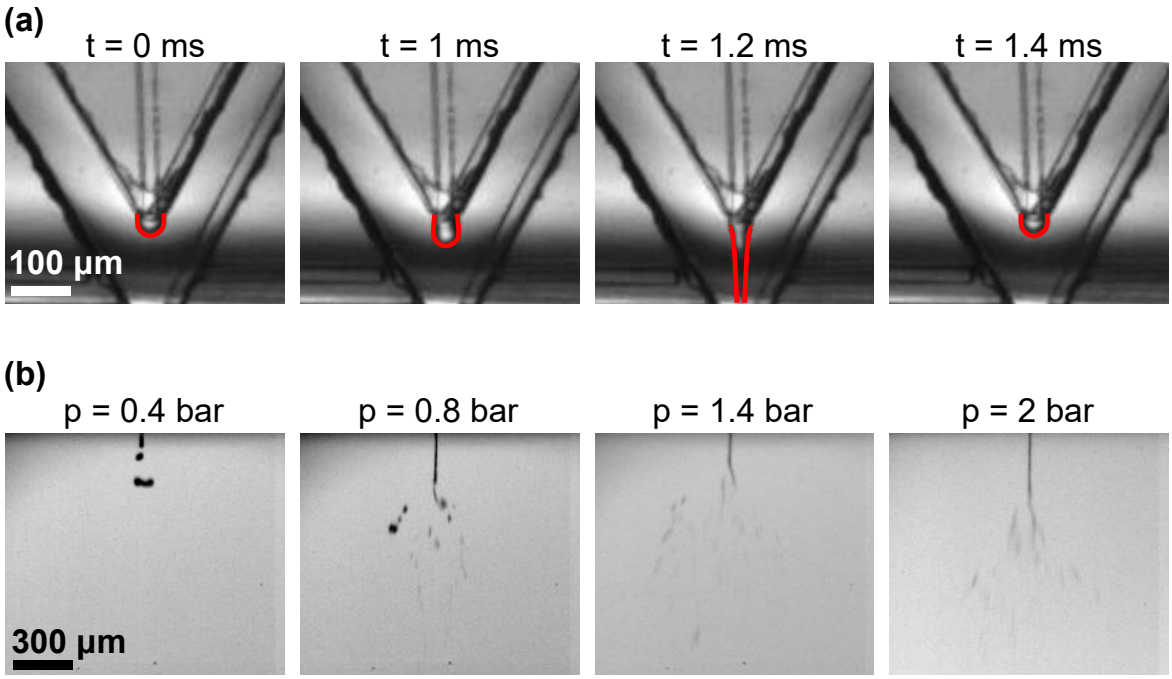

Fig. 3.3 Nozzle operation for water solution flowing at 100 µL/h. (a) At a pressure of $\Delta p = 2$ bar, the device is observed to operate in a dripping regime: a droplet at the liquid outlet is formed and increases in size until it is elongated and ejected through the device orifice with a frequency of ~ 700 Hz . (b) The generated jet breaks into droplets outside the device due to the instabilities caused by high shear forces. The spray is studied as a function of the gas pressure: at low pressures, a small number of large droplets is generated; however, qualitatively smaller drops are generated for increased gas pressure.

than $\Delta p \approx 0.9$ bar. Finally, the imaging area was focused 3 cm below the nozzle and the droplet speed was measured to be $v_d \approx 20$ m/s by considering the smear on one image frame l_{smear}/t_{fr}.

3.4.3 Drop-size distribution measurement

To quantify the drop-size distribution, I have used a recently developed Spraytec laser-scattering system [189]. I investigated the generated drop distributions while varying gas pressure and liquid flow rate, as shown in Figure 3.4. First, I fixed the liquid flow to 200 µL/h and varied the gas pressure Δp between 1.5 bar and 3 bar. As expected, the drop diameter decreased for increasing gas pressures from about 8 µm to 5 µm. Then, I fixed the pressure to 3 bar and investigated the nozzle operation at varying liquid flow rates ranging between 200 µL/h - 400 µL/h and observed a slight generated drop diameter increase from 5.3 µm

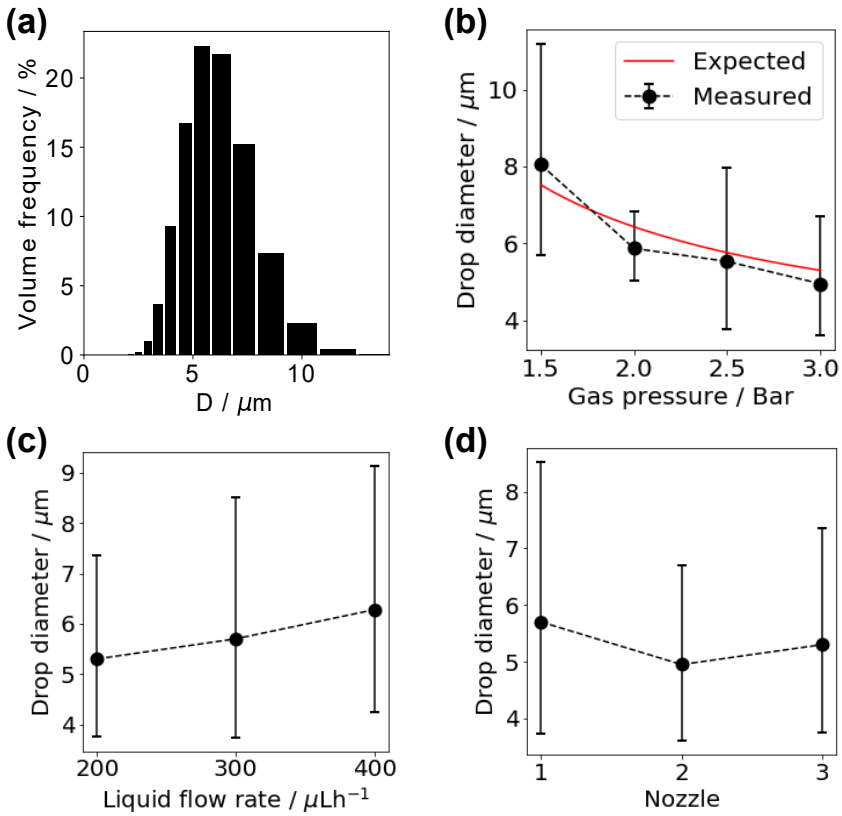

Fig. 3.4 Drop-size distributions measured 2 cm away from the nozzle orifice. (a) The measured size distribution of droplets at $\Delta p = 3$ bar and $Q = 200$ µL/h. (b) Variation in drop-size as a function of gas pressure shows a decreasing trend, as expected. (c) Drop diameter increases slowly with increasing liquid flow rate, indicating a bias towards larger generated drop sizes. (d) Nozzle-to-nozzle variation is tested at $\Delta p = 3$ bar and $Q = 200$ µL/h, giving an average drop diameter of 5.3 µm.

to 6.3 µm . Every spray device is custom made and may have a slightly different geometry due to the errors in manual fabrication. Therefore, I finally investigated the device-to-device variation at $\Delta p = 3$ bar and $Q = 200$ µL/h. The average median droplet size was found to be 5.3 ± 0.4 µm, as shown in Figure 3.4. The variation in the median, however, was insignificant compared to the broad drop distribution.

3.4.4 Drop-size distribution prediction

To predict the size of the generated drops, I consider the shear stress, caused by the large difference in speeds between the emerging gas and the formed liquid drops $\Delta v = v_g - v_d \approx v_g$.

The shear forces destabilise the liquid-gas interface forming surface waves - the Rayleigh - Taylor type of instability - eventually leading to the jet breakup [178]. I estimated the sizes of the drops by considering the balance between the aerodynamic shear stress and the surface tension on the generated drops:

$$\frac{1}{2}C_d\rho_g\left(v_g - v_d\right)^2 = \frac{2\gamma}{R_d} \tag{3.3}$$

where ρ_g and v_g are the gas density and speed, R_d and v_d are the generated drop radius and speed, γ is the surface tension, C_d is the coefficient of drag of around 0.47 for smooth spheres at high Reynolds numbers [190]. By considering that the drop speed was much slower than the gas speed $v_d \ll v_g$, I estimated the diameter of the generated droplets to be:

$$d_d = \frac{8\gamma}{C_d\rho_g v_g^2} \tag{3.4}$$

This relation gave an estimate for the generated drop size between $5-8$ µm at gas pressures between $1.5-3$ bar, which was comparable to the measured droplet diameters, as shown in Figure 3.4b.

3.4.5 Drop drying time

The total drop drying time involves two drying mechanisms: drying during the time of flight and evaporation after landing on the deposition surface. I could estimate that the boundary layer thickness during the flight of the drop was $\delta \approx 4.91\sqrt{\frac{\nu_w R_d}{v_g}} \approx 1.6$ µm [136]. The Peclet number (ratio of the rate of advection to the rate of diffusion) for the water-molecule transfer across the boundary layer was $Pe = \frac{\delta v_g}{D_w} \approx 25$; here $\nu_w = 1.5\cdot 10^{-5}$ m^{2}s^{-1} is the water kinematic viscosity, $D_w = 2.8\cdot 10^{-5}$ m^{2}s^{-1} is the water-molecule diffusion constant. Therefore, I deduced that the droplet in-flight evaporation rate is convection driven and limited by the rate at which water molecules leave the droplet surface. The Maxwell kinetic theory of evaporation gives the average number of molecules leaving a unit surface area [191]:

$$\frac{dN}{dt}\frac{1}{A} = -\frac{p_{vap}}{\sqrt{2\pi m_{H_2O} k_B T}} \tag{3.5}$$

where p_{vap} is the vapour pressure, m_{H_2O} is the water molecule mass, k_B is the Boltzmann constant and T is the absolute temperature. Considering the molecule-evaporation rate through a thin layer of drop surface area A and density ρ_w, I could estimate the droplet

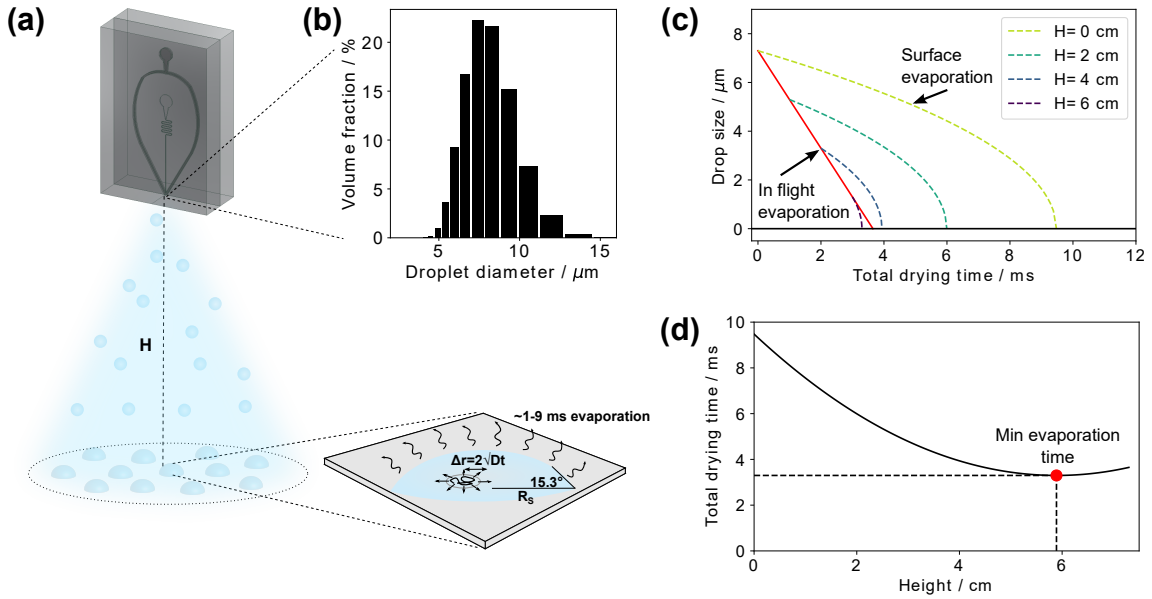

Fig. 3.5 Sessile-drop surface drying after the spray deposition. (a) The microfluidic nozzle spraying distance determines the drop surface drying time. Drops of initial distribution between $5.7-9.5$ µm (b) dry in $1-9$ ms, depending on the deposition distance (c). The minimum total drop drying time can be achieved at a distance of $H = 5.9$ cm away from the surface, leading to the total drying time of 3.3 ms between the drop spray generation and complete drying.

diameter shrinking rate:

$$\frac{dD}{dt} = -\frac{2p_{vap}\sqrt{m_{H_2O}}}{\rho_w\sqrt{2\pi k_B T}} \tag{3.6}$$

For water droplets at normal atmospheric conditions with vapour pressure $p_{vap} = 962$ Pa at a relative humidity 40 % and temperature 20° C, I could estimate the droplet shrinking rate to be approximately $\alpha = 2$ µm/ms.

The average measured drop size of 5.3 µm and a distance 2 cm away from the nozzle ($t_{flight} = 1$ ms, considering the average 20 m/s droplet speed) gave the median generated drop size of $D_0 = 7.3$ µm ranging from 5.7 µm and 9.5 µm ($10-90$ %). The original drop-size distribution is presented in Figure 3.5b. The most likely drop diameter during the time of flight can be expressed as a function of distance H from the nozzle:

$$D_a = D_0 - \alpha\frac{H}{v_d} \tag{3.7}$$

Considering the droplet distribution, they would completely dry around 10 cm away from the nozzle. However, if the deposition surface was closer, a partially dried droplet of diameter D_a landed on the surface with a contact angle of approximately $\theta \approx 15.3^\circ$ which was obtained from contact-angle measurements. The surface sessile drop diameter is $D_s \approx 2.7D_a$, assuming a constant droplet volume during the landing process and that the sessile drop is thin compared to its radius. To find this, I considered that the spherical drop of radius R_a and volume $4\pi R_a^3/3$ forms a sessile drop of surface radius R_s, contact angle θ and volume $\sim \pi R_s^3\theta/4$ [192].

In contrast to drying during the time of flight, the drop evaporation rate on the surface is limited by water-molecule diffusion from the surface since the gas velocity at the substrate surface is close to zero [193, 194]. However, the surface area of evaporation is increased upon landing; therefore, the evaporation may become faster on the surface compared to the evaporation in-flight. The droplet shrinking rate on the surface can be explained by the d^2 law of evaporation $D_s^2 = D_i^2 - \beta t$; here D_s is the droplet surface diameter, D_i is the initial surface drop diameter, β is the drying constant and t is time [194]. I have measured the droplet evaporation time by using a high-speed camera and found that, when spraying at a distance of 2 cm away from the surface, the droplet drying time was around 5 ms, giving $\beta = 4.1 \cdot 10^{-8}$ m^{2}s^{-1}. The droplet drying time on the surface t_{dry} can be expressed as a function of the spray-deposition distance:

$$t_{dry} = \frac{D_i^2}{\beta} = \frac{(D_0 - \alpha H/v_d)^2}{\beta} \tag{3.8}$$

For example, droplets deposited at a distance of $H = 1$ cm would evaporate in 7 ms, whereas droplets landing 5 cm away from the nozzle would evaporate in 0.9 ms on the surface, as illustrated in Figure 3.5c. If the total drying time needs to be minimised, one should place the nozzle at a distance of $H_{min} = 5.9$ cm, leading to an average drop-drying time $t_{min} = 3.3$ ms, of which 0.35 ms is spent on the surface (see Figure 3.5d).

3.4.6 Protein sample deposition for AFM imaging

Manual sample deposition and the AFM measurements were carried out by Dr Francesco Simone Ruggeri, initial spray experiments were carried out by Dr Jerome Charmet.

Finally, the spray drop generation and understanding of the drop drying behaviour was used to deposit biomolecules on an AFM imaging surface. In general, molecules in solution upon

attachment to the surface due to electrostatic and van der Waals forces, undergo 2-dimensional surface diffusion, on average travelling a distance:

$$\Delta r = 2\sqrt{D_{surf} t_{dry}} \tag{3.9}$$

where I estimated the surface diffusion constant of biomolecules to be $D_{surf} \approx 0.2 \pm 0.1$ $\mu m^2 s^{-1}$, based on previously reported DNA surface diffusion rate [195]. Considering sample deposition at 4 cm away from mica substrate, the surface drying time is approximately 2 ms, giving a typical surface molecular diffusion distance in the range $\Delta x \approx 40 \pm 20$ nm.

Typically, samples on AFM-imaging substrates are deposited manually, which is highly user dependent and requires long operational times, ranging from tens of seconds to minutes, leading to micron-scale diffusion distances [196]. For biological sample measurements in ambient environments, as shown in Figure 3.6a, the procedure can be summarized in the steps of: 1) deposition of a microliter size droplet on the substrate; 2) water rinsing; and 3) drying with a gas flux or an aspiration system [197].

Common AFM-imaging surfaces are negatively charged mica or positively charged glass [198]. The long deposition and manual preparation time can cause self-assembly and reorganization of the sample molecules on the surface. It is demonstrated in Figure 3.6b how α-synuclein monomers self-organized along the crystallographic directions of the surface of the mica lattice, which is highly undesirable for protein-mixture characterisation in aggregation-related disease studies [199, 200]. Moreover, the rinsing and drying steps could cause selective molecule absorption. In Figure 3.6c, I show that the manual deposition of a heterogeneous aggregated solution of Aβ42 protein, composed of protofibrillar and oligomeric aggregates. Only the oligomeric species were observed on the surface after the manual deposition; thus, the effect of selective absorption masked the effective heterogeneity of the deposited protein solution.

Microfluidic spray deposition, however, was able to overcome the issues discussed above by shortening the molecular diffusion time on surface to a few milliseconds with no need for a washing step. I spray-deposited α-synuclein and Aβ42 protein solutions at 4 cm away from the mica surface, thus achieving a surface drying time of ~ 2 ms and demonstrated that protein self-organization and the differential adsorption on mica surface can be avoided, as shown in Figure 3.6e and Figure 3.6f.

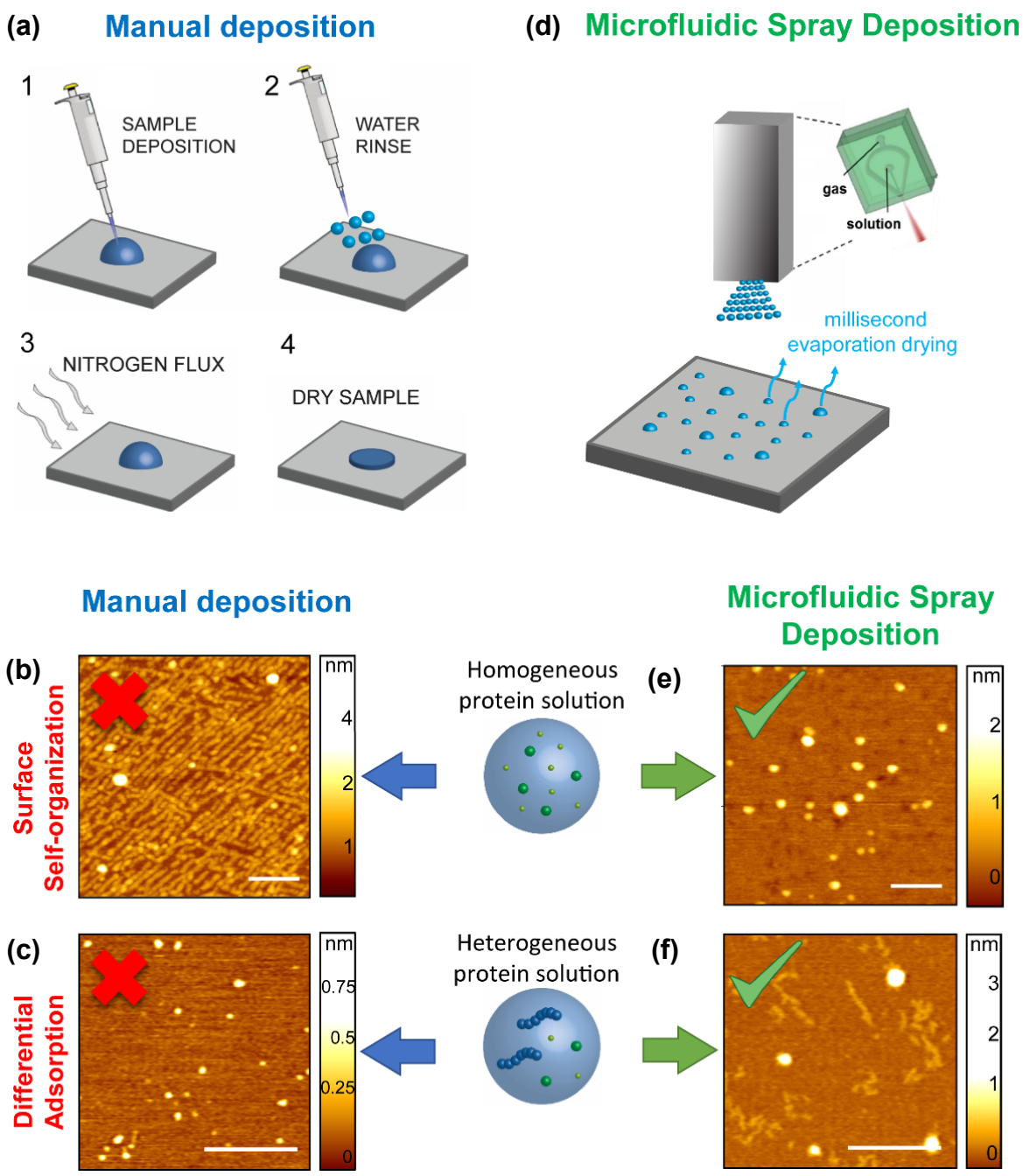

Fig. 3.6 Standard manual vs. single-step deposition by a microfluidic spray device. AFM sample preparation by (a) conventional manual deposition. This method may cause the (b) self-organization of monomeric α-synuclein along the crystallographic lattice of the mica substrate (scale bar 100 nm). (c) Furthermore, manual deposition typically enables only a partial depiction of a heterogeneous Aβ42 aggregated solution on a mica surface because of differential adsorption (scale bar 100 nm). While, (d) single-step microfluidic spray deposition (e) conserves the molecular architecture and assembly state of proteins in solution and (f) enables the analysis of the full content of the heterogeneous protein mixture (scale bars 200 nm).

3.5 Conclusions

In this chapter, I have described the design of a microfluidic spray nozzle which produced aqueous drops with micron-sized diameters. The pressurised gas flow through the nozzle was modelled as a choked flow through a converging-diverging de Laval type nozzle [186], reaching supersonic speeds at the spray orifice. The supersonic gas flow exerts high shear forces on the emerging liquid, thus atomising it into drops of 7 µm in diameter. I characterised the nozzle operation and measured the emerging drop-size distributions under varying pressures and flow rates. After landing on a surface, drops increase their surface-to-volume ratio due to surface wetting and evaporate in $1-9$ ms, depending on the spraying distance. I have investigated different drop-drying regimes and estimated the minimum total evaporation time. Finally, I have used the microfluidic nozzle to deposit α-synuclein and Aβ42 proteins on mica, achieving average millisecond-scale drop evaporation. This approach helped to avoid protein surface self-assembly and the differential adsorption, thus allowing for an unbiased sample characterisation.

Chapter 4

Label-free biosensing with microcantilevers integrated into microfluidic systems

4.1 Summary

Microelectromechanical systems (MEMS) have enabled the development of a new generation of sensor platforms. Acoustic-sensor operation in liquid, the native environment of biomolecules, causes, however, significant degradation of sensing performance due to viscous drag and relies on the availability of capture molecules to bind analytes of interest to the sensor surface. Here, I describe a strategy to interface MEMS sensors with microfluidic platforms through an aerosol spray. The sensing platform comprises a microfluidic spray nozzle and a micro-cantilever array operated in dynamic mode within a closed-loop oscillator. A solution containing the analyte is sprayed uniformly through pico-litre droplets onto the micro-cantilever surface; the micron-scale drops evaporate rapidly and leave the solutes behind, adding to the mass of the cantilever. This sensing scheme results in a 50-fold increase in the quality factor compared to operation in liquid, yet allows the analytes to be introduced into the sensing system from a solution phase. It achieves a 370 femtogram limit of detection and I demonstrate quantitative label-free analysis of inorganic salts and model proteins. These results demonstrate that the standard resolution limits of cantilever sensing in dynamic mode can be overcome with the integration of spray microfluidics with MEMS.

Parts of this work previously appeared in:

***Tadas Kartanas**, Victor Ostanin, Pavan Kumar Challa, Ronan Daly, Jerome Charmet, and Tuomas PJ Knowles. Enhanced Quality Factor Label-free Biosensing with Micro-Cantilevers Integrated into Microfluidic Systems. Analytical chemistry **89**, 11929-11936 (2017).*

4.2 Introduction

The development of platforms for biosensing has been the subject of extensive research efforts for a number of years. However, fundamental challenges remain in developing devices to meet the need for sensitive, quantitative and high-throughput [201] sensing which is required to unlock many key applications including in vitro diagnostics [202]. Micro-electromechanical systems (MEMS), which can be mass produced and fully integrated with microelectronics, are promising candidates for low-cost, high-resolution gravimetric biosensing [60, 203]. However, even though they can reach mass resolutions down to the zeptogram level under high-vacuum conditions [204], such transducers suffer high losses when operated in a viscous liquid environment, degrading their gravimetric sensitivity and reducing the quality factor [73, 74, 205, 206]. Indeed, using a first-order approximation and neglecting changes in the material stiffness upon analyte adsorption, the sensitivity is given by:

$$\frac{\Delta f}{\Delta m} = -\frac{f_0}{2m_0} \tag{4.1}$$

where m_0 is the mass and f_0 is the resonant frequency of the resonator. Using this simple equation, the changes in the resonant frequency Δf can be related to the mass changes Δm on the surface of the resonator. High sensitivity can thus be achieved by reducing the transducer size to minimise its mass and maximise the resonant frequency. The quality factor Q is an important measure directly related to the sensor limit of detection (LOD), as it quantifies the sharpness of the resonance peak and sets a limit on the minimum detectable frequency shift. The typical quality factor of MEMS sensors in vacuum can be as high as $10^4 - 10^6$ [207, 208] whereas it drops down to $100 - 1000$ [209, 210] in air and can be lower than 10 in liquids [211–214]. This low Q-factor, which causes a wider resonance peak, significantly limits the minimum detectable mass by the sensor. Moreover, the effective mass of the resonator increases in liquids, thus further reducing the transducer sensitivity [206, 215]. Finally, the interpretation of the sensor readouts in liquid is not straightforward as the frequency shifts are caused by both the gravimetric loading and the increased viscous drag [73].

Another technical barrier potentially frustrating the more widespread entry of micro/nano sized sensors into the market as bio-sensors [216] is their problematic integration with sample

delivery and preparation techniques using small sample volumes [60, 77, 217]. A commonly used approach to address the integration challenge is to functionalise the resonator surface with capture molecules [218], which target specific proteins, and measure the resonator frequency shifts in liquid-flow cells. This approach leads to a number of possible issues. In particular, the surface capture molecule design is a complex and costly process and many key disease biomarkers, for example for Alzheimer's disease [219, 220], still need specific labels to be developed. In the case of conventional biosensing, including surface-plasmon resonance (SPR) [221] and quartz-crystal microbalance (QCM) flow cells [222, 223], standard capture molecules are required and the presence of a surface can influence the measured affinity values and, hence, the mass measurements. Moreover, the flow cell needs a careful design, taking into account the analyte diffusion and convection towards the sensor; this optimisation is needed to maximise the reaction rate between the capture molecules and the biomarker [224].

A particularly innovative and elegant solution to address MEMS sensor integration and Q-factor losses when operating in liquid is to integrate a narrow channel inside the cantilever [225] and measure the buoyant mass of the analytes that flow through the channel. Such suspended nanochannel resonators have enabled the measurement of masses down to the attogram scale in liquid [226, 227], and more recently have achieved an increased throughput [228]. However, their fabrication still remains complex and the setup requires a vacuum package to minimize the viscous losses [205].

Here, I explore a fundamentally different approach to high Q-factor sensing of analytes in liquids by spraying droplets onto a gravimetric sensor using microfluidics, as illustrated in Figure 4.1. The micrometer scale droplets evaporate rapidly, leaving the dry solute on the sensor surface and thereby decreasing its resonant frequency. The relationship between the increased mass of the sensor and the frequency shift is given by Equation 4.1. This detection scheme in air is designed to suffer less from the decrease in the sensor resolution due to the viscous losses inherent to measurements in liquid [73]. To explore the potential of this approach, I have built an AFM-like [229] MEMS cantilever resonant-frequency measurement setup and integrated it with a 3D microfluidic spray fabricated for the purpose of the study using soft-lithography techniques [84]. The spray nozzles work by creating a Rayleigh-Taylor type of instability [166] with the help of pressurized gas flowing past a narrow fluid outlet. Similar nozzles were previously used for drug formulation [179], microbubble generation [135], and amorphous nanoparticle production [136]. Dry mass sensing in air is on a conceptual level a tightly controlled and, thus, more robust version of one of the earliest biosensing dip-dry-measure formats [230]. This work, to my knowledge,

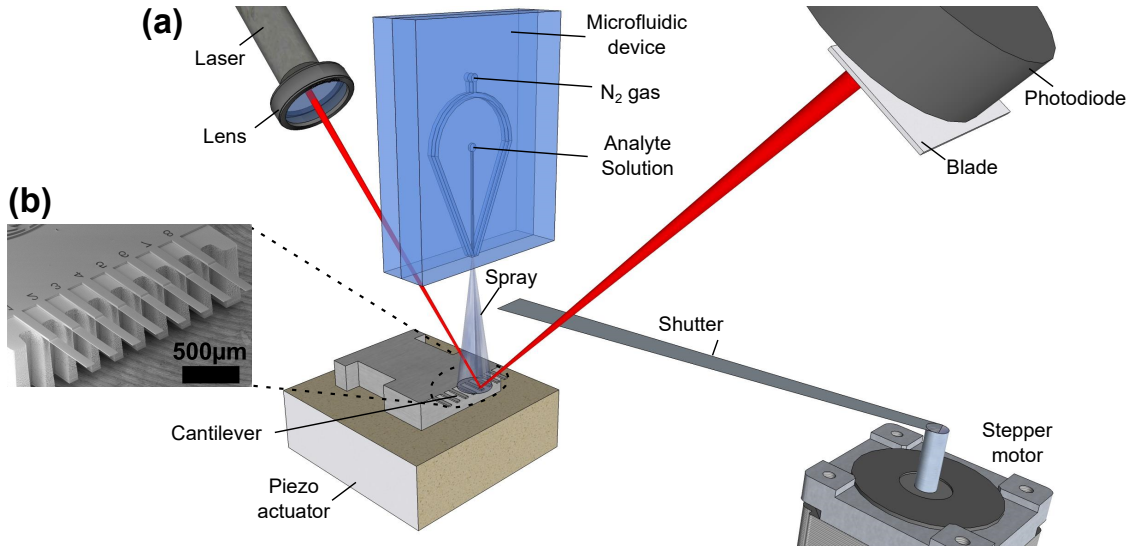

Fig. 4.1 A scheme of the dry mass sensing setup. A 3D microfluidic spray nozzle, positioned above a MEMS sensor (SEM image shown in (b)), uniformly sprays micrometer-sized rapidly evaporating droplets onto the cantilevers, thus, gradually increasing the sensor mass and decreasing its resonant frequency. A laser beam is focused onto a MEMS cantilever which is in turn excited by a piezo ceramic actuator. The resulting motion of the laser beam is detected with a single channel photodiode. The shutter stops the spray; the cantilever is locked in the lowest transverse oscillation mode with a positive feedback loop, and the resonant frequency is measured with a frequency counter reading the time-dependent signal from the photodiode.

is the first attempt combining the benefits of microscale flow processing with MEMS high Q-factor in-air measurement.

4.3 Materials and methods

4.3.1 Nozzle fabrication

The microfluidic nozzle was fabricated using a two-PDMS-layer method, as described in Section 3.3.1. However, a slightly larger nozzle containing two inlets on one chip was designed and fabricated using the same procedure. The nozzle design is shown in Section 4.4.7.

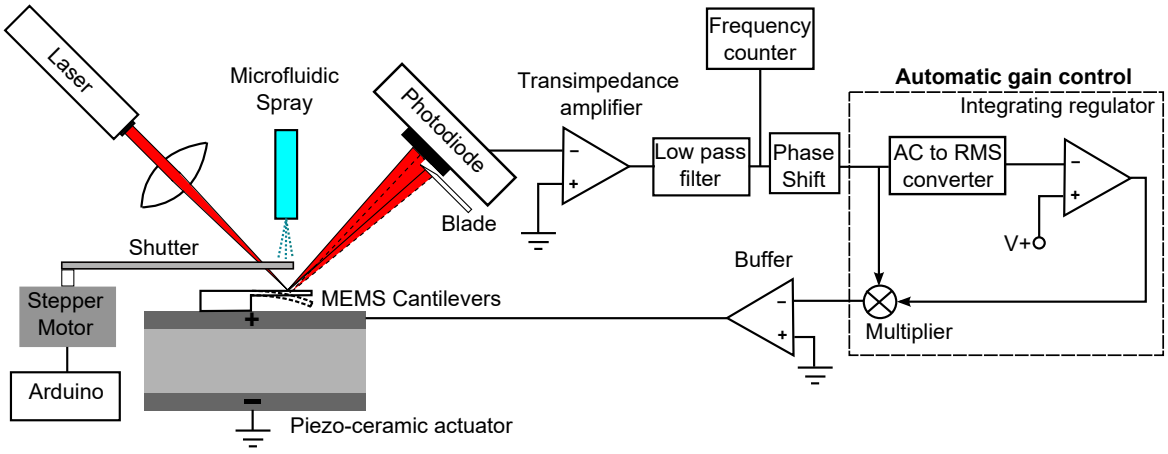

Fig. 4.2 A schematic of the oscillator setup. A laser beam is focused onto a MEMS cantilever which is excited by a piezo ceramic actuator. The resulting motion of the laser beam is detected with a single channel photodiode by covering half of the diode. The resonator is locked in the lowest transverse oscillation mode with a positive feedback loop comprising a transimpedance amplifier, a phase shifter, an automatic gain control and a buffer driving the piezo actuator. A microfluidic spray, positioned above the sensor, allowed a uniform deposition of analytes, transported to the surface of the sensor via fast-drying droplets. The mass deposited resulted in a continuous frequency decrease which was monitored with a frequency counter.

4.3.2 Cantilever resonant-frequency measurement setup

The positive feedback loop system was designed in collaboration with Victor Ostanin.

A schematic of the sensor platform is shown in Figure 4.2. The cantilevers were excited with a piezo ceramic actuator from ThorLabs (TA0505D024W). The cantilever chip was clamped to the piezo actuator which was in turn fixed to an xyz-micrometer stage. A 1 mW (635 nm) laser beam was focused on the cantilever surface; the position of the reflected beam was detected with a single channel photodiode from ThorLabs (SM1PD1A) with a half of the diode covered. The cantilever oscillation results in a variation of the reflected beam position and, therefore, the exposed area on the photodiode. This arrangement consisting of a single photodiode was significantly simpler than the multi-quadrant photodiode setups conventionally used for this purpose, however with a slightly increased noise level. In addition, an analogue feedback loop was implemented to keep the chosen cantilever oscillating at its resonant frequency. The frequency was recorded with a frequency counter (TTi TF930) using 1 s running average and the continuous frequency-measurement data acquisition was monitored by a Raspberry Pi 2.

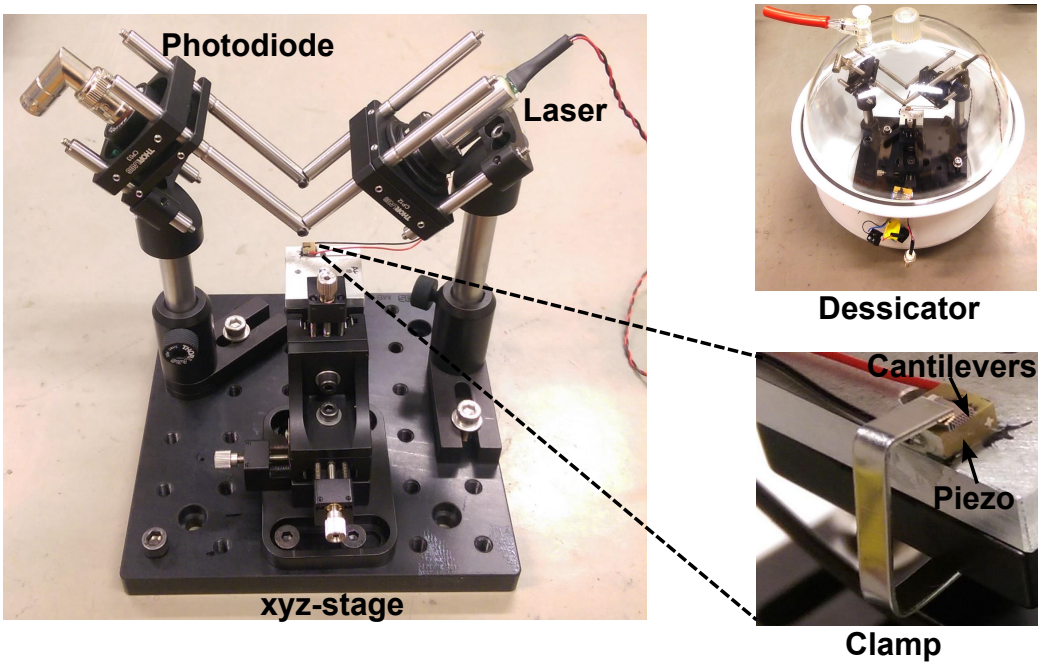

Fig. 4.3 A picture of the setup. The platform dimensions allow it to be placed in a desiccator to avoid disturbances from an external air flow. The cantilevers are clamped to the piezo actuator which allows for an easy cantilever-changing procedure between multiple spraying experiments.

The positive feedback loop consisted of a transimpedance operational amplifier (AD845), a low-pass filter (RC network), a 45° phase shifter (RC network), an automatic gain control circuit containing an AC-to-RMS converter (AD845 and MPY634), an integrating regulator (AD845), a multiplier (MPY634), and, finally, a buffer (AD845) was used to drive the piezo ceramic actuator which induced the cantilever oscillations. The system was placed in a desiccator to isolate any air flow from the cantilever surroundings. A picture of the optical setup is shown in Figure 4.3.

4.3.3 MEMS cantilever-mass prediction

The resonant frequency of a cantilever in vacuum is given by:

$$f_n = \frac{\alpha_n^2}{2\pi}\sqrt{\frac{E_Y H_c^2}{12\rho_c L_c^2}} \tag{4.2}$$

where α_n is the n-th excitation mode shape constant, E_Y is Young modulus, ρ_c is the density, H_c is the thickness and L_c is the length of the cantilever [231]. Silicon OCTOSENSIS dynamic-mode cantilevers containing eight cantilevers per chip were purchased from Micromotive MIKROTECHNIK (see Figure 4.1). The cantilever dimensions were $L_c = 500 \pm 4$ µm, $W_c = 90 \pm 2$ µm, $H_c = 5 \pm 0.3$ µm with the errors indicating manufacturing process tolerances. For a cantilever operating in the first mode ($\alpha_0 = 1.875$, $E_Y = 180$ GPa, $\rho_c = 2330$ kg/m^3), the resulting prediction for the mass of the cantilever is $m_0 = 524 \pm 34$ ng and the resonant frequency $f_0 = 28.4 \pm 1.8$ kHz, after combining the errors of the physical cantilever size in quadrature. As a result, the cantilever resonant frequency varied between $27 - 31$ kHz from device to device due to the manufacturing uncertainties. The resonant frequency of each sensor was measured prior to every experiment so that the sensor mass could be estimated. The fractional error due to the cantilever thickness is one order of magnitude larger than the error in length and width so the cantilever resonant frequency is dominated by the changes in its thickness. Hence, I estimated the cantilever thickness from the resonant frequency measurement using the relationship below:

$$H_c = f_0 L_c^2 \frac{2\pi}{1.875^2} \sqrt{\frac{12\rho_c}{E_Y}} \tag{4.3}$$

giving the corresponding mass:

$$m_0 = \rho_c L_c W_c H_c = \rho_c f_0 W_c L_c^3 \frac{2\pi}{1.875^2} \sqrt{\frac{12\rho_c}{E_Y}} \tag{4.4}$$

and the error in a particular cantilever mass:

$$\Delta m = m_0 \sqrt{\left(\frac{3\Delta L_c}{L_c}\right)^2 + \left(\frac{\Delta W_c}{W_c}\right)^2 + \left(\frac{0.01}{f_0}\right)^2} \tag{4.5}$$

where 0.01 Hz is the error in the frequency measurement within the dry mass-sensing setup presented in Section 4.4.1.

4.3.4 Shutter integration and frequency extraction

Spraying onto a cantilever surface introduced instabilities due to the droplets landing and evaporating on the surface, as well as perturbations from the nitrogen flow. These factors together meant that the resonant frequency could not be recorded accurately during the continuous spraying interval. Therefore, a remotely controlled mechanical shutter, actuated

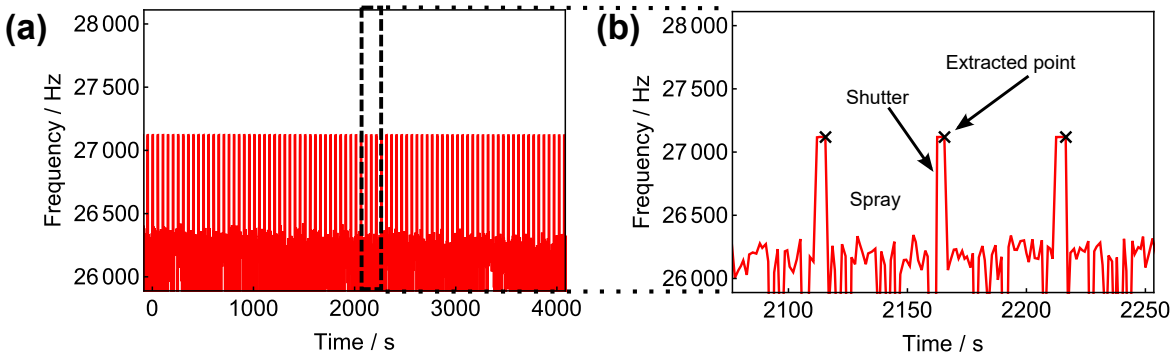

Fig. 4.4 Frequency extraction during the microfluidic spray experiments. (a) Usual set of data throughout the spraying experiments. (b) The frequency is unstable during the microfluidic liquid spray on cantilevers. The spray is stopped for 5 s with a mechanical shutter so that the resonant cantilever frequency could be measured. The last stable frequency measurement is extracted for each of the closed shutter intervals.

using a stepper motor, was included to stop the spray for 5 s, allowing stable frequency readouts to be acquired during the closed interval. The analyte was sprayed onto the cantilevers for 45 s (90 % of the time). Typically, three to four frequency points were measured and the last reading was extracted before the shutter was opened allowing for further spraying, as shown in Figure 4.4. This procedure yielded frequency measurements every 50 s.

4.3.5 Response curve and phase-measurement setup

The cantilever chip was glued to the piezo actuator and placed in a closed chamber with a transparent window for the laser beam. The resonator response curve and the feedback-loop phase noise [232], describing the noise level in the system, were measured in air and water. For the measurements in liquid, the chamber was filled with deionised water. The laser beam position was adjusted with the micrometer stage to account for the change in the refractive index. The resonator was tested in an open-loop configuration using a lock-in amplifier SR830 from Stanford Research Systems, as illustrated in Figure 4.5. For the response curve measurements, scans around the resonant frequency, in steps of 10 Hz, were performed using a 100 ms time constant. Then, the resonant cantilever frequency was selected and the loop-phase variation over time was measured using a 1 s time constant to match it with the frequency-counter time constant.

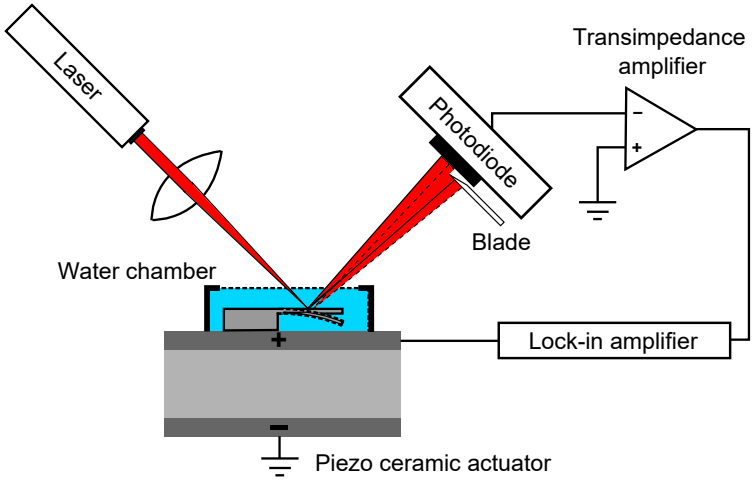

Fig. 4.5 Response curve and phase-noise measurement setup. The cantilevers are fixed to the piezo ceramic actuator and placed in a sealed chamber which can be filled with water. The micro-meter stage position needs to be adjusted due to the beam refraction in water. The reflected cantilever beam is detected by a photodiode and its electrical output amplified by a transimpedance operational amplifier (AD845) and connected to a lock-in amplifier.

4.4 Results and discussion

4.4.1 System limit of detection in air

The Q-factor is the main parameter determining the sensitivity level of an acoustic resonator. In this section, I present the characteristics of the sensing platform and evaluate the advantage of the sensor operation in air versus water.

The sensor LOD, usually denoted as the minimum detectable added mass (Δm_{min}), is inversely proportional to the Q-factor [230]:

$$LOD = \Delta m_{min} \propto \frac{m_0}{Q} \tag{4.6}$$

Allan deviation [233] is a measure of frequency stability in clocks and oscillators due to system-related noise processes, avoiding frequency drifts and temperature effects:

$$\sigma_y(\tau) \cong \left[\frac{1}{2(N-2)\tau^2} \sum_{k=1}^{N-2} \left(f_{k+2} - 2f_{k+1} + f_k\right)^2 \right]^{\frac{1}{2}} \tag{4.7}$$

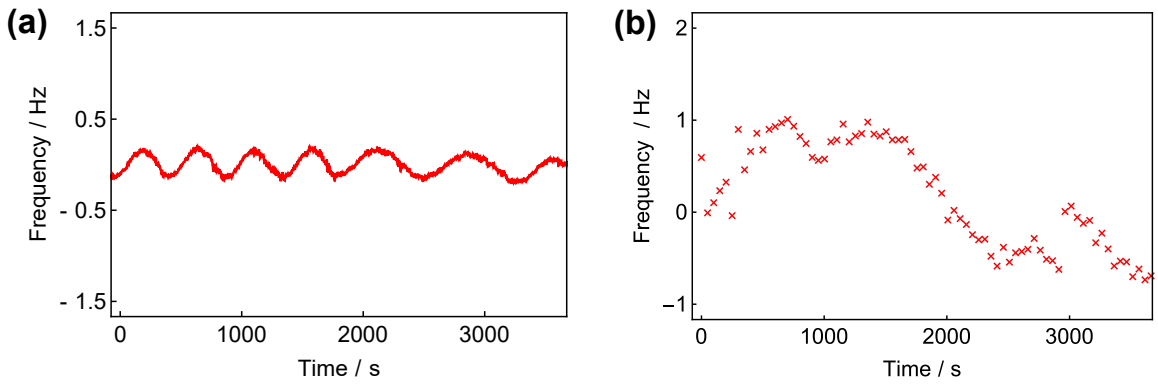

Fig. 4.6 Frequency stability of the system in air for 1 hour; (a) without any disturbances (centre frequency 27785 Hz); and (b) while spraying deionised water (measurements taken every 50 s, centre frequency 27120 Hz). The periodic frequency variation in (a) can be related to the ambient temperature variation caused by operation of the air conditioner.

where f_k, f_{k+1} and f_{k+2} are three consecutive frequency measurements with a gate time τ; N number of frequency measurements. First, the system frequency noise was characterised without the microfluidic spray, as shown in Figure 4.6a. The sensor platform was operated in air for 1 h, and the frequency was recorded with the frequency counter. The Allan deviation [233] with a gate time of 1 s gave a 0.01 Hz frequency noise level, which corresponds to 370 fg using Equation 4.1. This is the ultimate platform LOD.

The dry mass sensing experiments in air with a microfluidic spray introduces disturbances due to air pressure, humidity and temperature fluctuations. Therefore, the sensor LOD will be lower for real-time frequency measurements. Control measurements while spraying deionised water were performed to determine the sensor stability under these conditions, as shown in Figure 4.6b. The frequency noise was measured to be 0.32 Hz which corresponds to 12 pg and was the noise level for the continuous dry-mass sensing experiments in air. Potentially, the frequency-measurement stability could be enhanced even further by performing the cantilever-frequency measurement under low-vacuum conditions or allowing for longer cantilever equilibration times.

4.4.2 Advantage of cantilever operation in air versus water

To probe the advantages of operating the cantilevers in air, I measured the response curves and phase-noise in water and air, as shown in Figure 4.7. The quality factors were obtained by fitting the measurements to the frequency response of an oscillator in the harmonic limit

[210]:

$$A(\omega) = \frac{A_0 \omega_0^2}{\sqrt{\left(\omega^2 - \omega_0^2\right)^2 + \omega^2 \omega_0^2 Q^{-2}}} \tag{4.8}$$

where $\omega = 2\pi f$ is the angular driving frequency, A_0 is the amplitude of the response, Q is the quality factor, and $\omega_0 = 2\pi f_0$ corresponds to the cantilever resonant frequency. The Q-factors obtained were $Q_{water} \approx 5$ and $Q_{air} \approx 250$, with resonant frequencies $f_{water} = 10.2$ kHz and $f_{air} = 27.8$ kHz, respectively. The phase noise [232], which describes the system phase stability within a feedback loop at resonance, was also measured both in water and air, as shown in Figure 4.7b. The phase noise in water was $\Delta\phi_{water} = 0.044^\circ$ and it was measured to be $\Delta\phi_{air} = 0.01^\circ$ in air. The frequency noise can be expressed as follows:

$$\Delta f = \left(\frac{d\phi}{df}\right)^{-1} \Delta\phi \tag{4.9}$$

where $d\phi/df$ is the phase versus frequency gradient at resonance and $\Delta\phi$ is the phase noise. Using the measured phase as a function of frequency, gradients were measured to be -73.3 mDeg/Hz and -0.97 Deg/Hz for water and air, respectively, as shown in Figure 4.7e and Figure 4.7f. The frequency noise in water and air was found to be 0.61 Hz and 0.01 Hz, respectively. The ratio between the frequency noise levels was $\Delta f_{water}/\Delta f_{air} \approx 60$ and it was very similar to the ratio of the quality factors ($Q_{air}/Q_{water} \approx 50$). These results show that, indeed, the mass-sensing approach in air improved the LOD of the sensor by 2 orders of magnitude compared to operation in water [215].

4.4.3 Saline solution detection

I first sprayed deionized water on the MEMS cantilevers and confirmed that it caused a negligible frequency change, as shown in Figure 4.8. The standard deviation of the frequency signal was measured to be 0.3 Hz over a 2000 s measurement. I then sprayed a 500 µM NaCl solution onto the cantilevers at a flow rate of 50 µL/h. I observed that the frequency decreased due to the dry mass of NaCl accumulating on the surface, as depicted in Figure 4.8. The frequency trend gradient was evaluated and used to estimate the mass deposition rate. The frequency decreased by 27 ± 0.32 Hz over 2000 s, thus corresponding to a salt mass of 1.00 ± 0.03 ng deposited on the cantilever. The mass deposited on the sensor during one 45 s spraying interval is 24.9 ± 0.8 pg. In order to verify the masses obtained using the frequency measurements, I compared the values with the estimates based on the total amount of salt sprayed. Throughout 45 s, the total NaCl amount released by the microfluidic spray

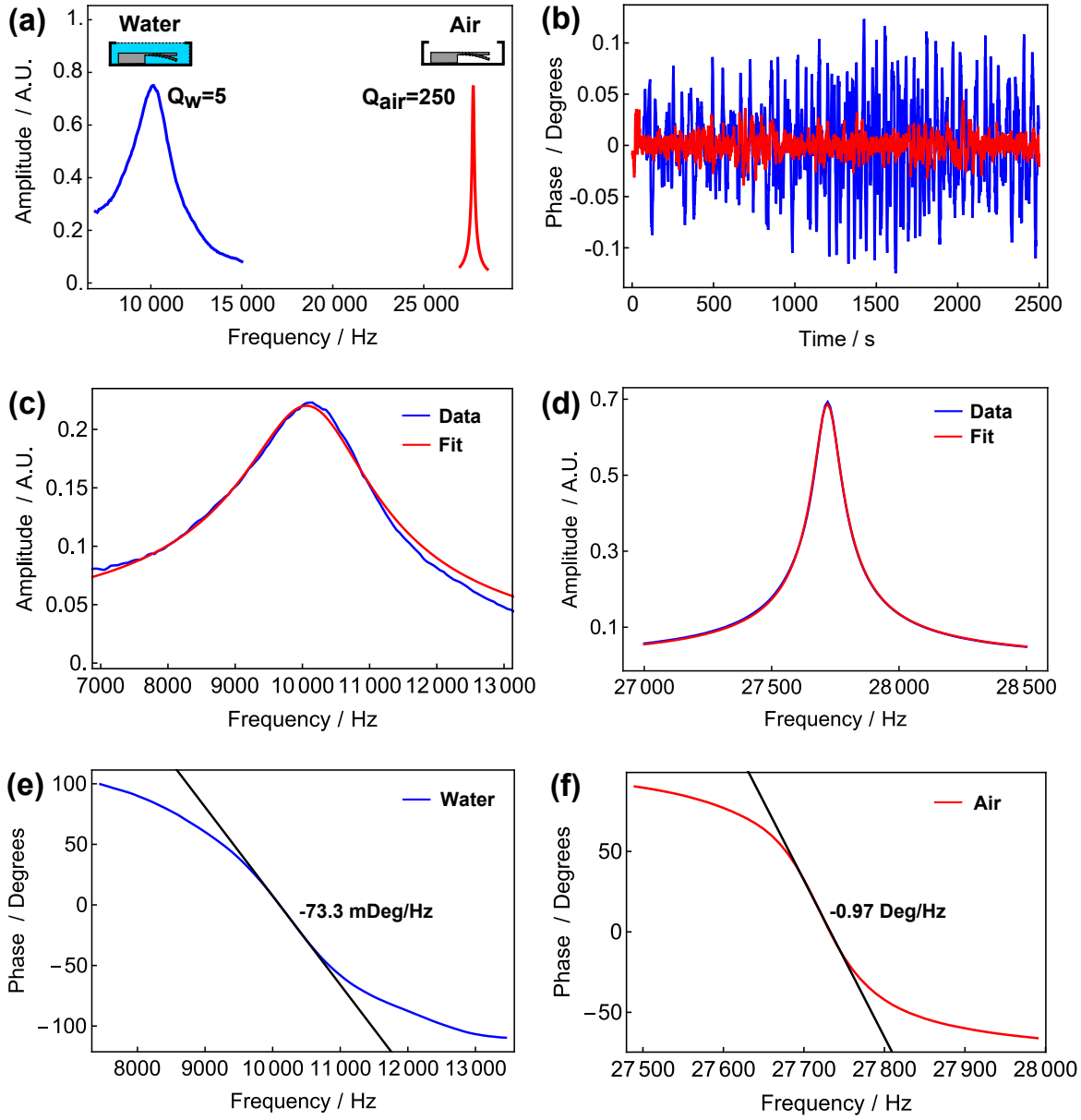

Fig. 4.7 Cantilever resonance characteristics in water and air. (a) Normalized cantilever response around resonance; the quality factor of the cantilevers is 250 in air compared to 5 in water, leading to (b) a much lower phase noise level in air. The response curve fits to a damped harmonic oscillator equation in water (c) and air (d). Similarly, the phase decrease gradient is smaller in water (e) versus air (f) indicating a broader resonance peak in an aqueous environment.

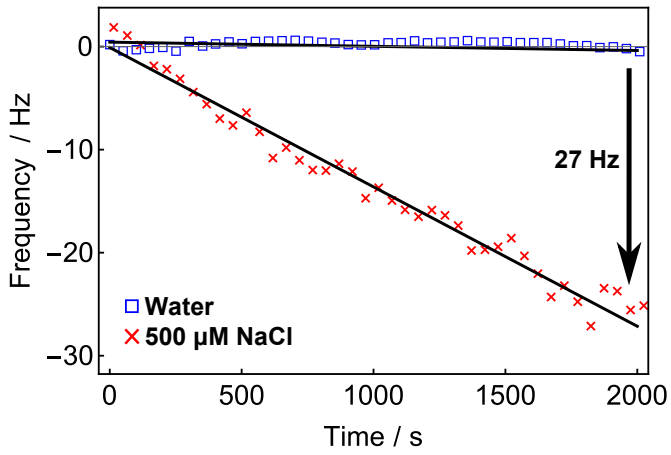

Fig. 4.8 Resonant-frequency variation of the cantilever while spraying deionized water and NaCl solution. The frequency (referenced to 27 734 Hz) decreases by 27 Hz over 2000 s as a result of spraying 500 µM NaCl salt on the sensor at a 50 µL/h flow rate.

device was 18.3 ng, but only a fraction of the liquid was captured on the cantilevers: the spray diameter was about 6.5 ± 0.5 mm at the cantilever levelled 2 cm away from the spray, whereas the area of a single cantilever $A_c = 45000$ µm^2. Taking this factor into consideration, the total mass reaching the sensor corresponded to 25 ± 4 pg, which agrees with the measured value within the errors.

4.4.4 Concentration-sensitive BSA detection

I next verified that this approach could be applied to determine the dry mass of proteins in aqueous solution. To this effect, I prepared 100 and 500 nM BSA protein solutions and deposited them on a cantilever at a 50 µL/h flow rate, as shown in Figure 4.9a. First, I observed that the fluctuations in the frequency were further reduced for the BSA solution compared to NaCl experiments. This finding may be explained by the fact that BSA adheres to surfaces under neutral pH conditions [234] and, therefore, protein molecules already deposited on the cantilever were not displaced (or displaced less) by the droplets landing subsequently. In the case of NaCl, the droplets landing on the cantilever may dissolve and displace the salt crystals deposited previously. The 100 nM solution gave a -3.2 mHz/s decrease gradient, whereas it was -18.3 mHz/s for the 500 nM solution. I also sprayed deionized water to determine the error in the gradients for the continuous mass-sensing experiments and obtained a trend with a gradient of -0.4 mHz/s. As expected, the 500 nM protein solution gave a steeper frequency drop, with a ratio between the two different concentrations of 5.8 ± 0.8, taking

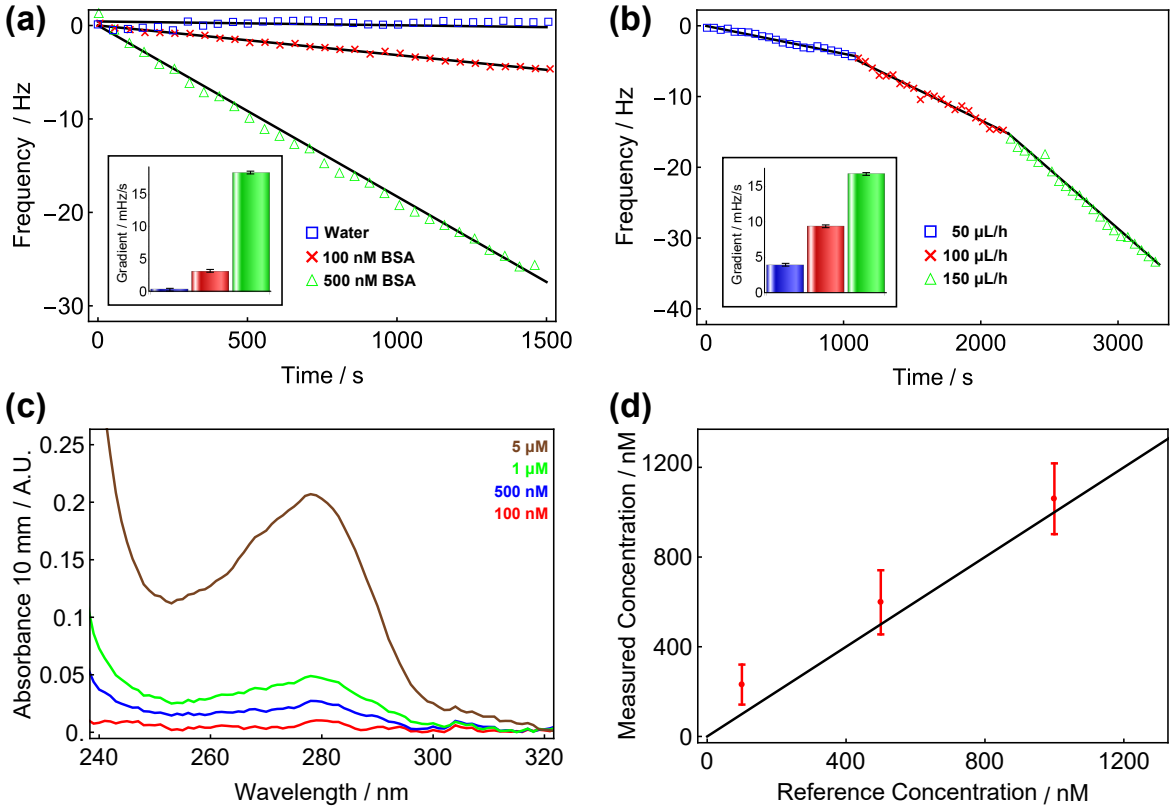

Fig. 4.9 Frequency shift induced by the deposition of BSA. (a) The comparison between deionized water and BSA at different concentrations and a fixed flow rate of 50 µL/h (start frequency 27 165 Hz). (b) The frequency downshift induced by a 100 nM BSA solution sprayed at different flow rates (start frequency 27 132 Hz). (c) The UV absorption spectra of BSA for different concentrations using NanoDrop 2000. (d) The concentration measurement of dilute BSA solutions, based on an absorption value at 280 nm.

into account the error in gradient while spraying water. The experimental procedure might have introduced some systematic errors: two different spray nozzles were used, and the alignment of the nozzles above the sensors was a little different. However, these errors were not significant, and only a small variation from the expected ratio of 5 was observed.

4.4.5 Sensing BSA at different flow rates

Next, I explored whether it was possible to deliver the analytes on the sensor at different volumetric flow rates. To demonstrate this objective, 100 nM BSA solution was sprayed at multiple flow rates: 50, 100 and 150 µL/h. The data in Figure 4.9b shows that indeed the frequency shift was related to the liquid spray rate. The measured gradients were

-3.9 ± 0.4 mHz/s, -9.4 ± 0.4 mHz/s, and $-16 : 8 \pm 0.4$ mHz/s, respectively, giving ratios of 1 : 2.4 : 4.3. The small difference from the expected result of 1 : 2 : 3 was likely to arise from the fact that the spray angle and, thus, the droplet density distribution within the spray area, changes slightly at different flow rates. Note that this behaviour was not an obstacle for mass sensing with a fixed flow rate since the spray area remained constant during an experiment.

4.4.6 BSA concentration measurement with UV absorption

To compare the results with conventional quantification by UV absorption, I measured UV absorption spectra of BSA at different concentrations, ranging from 100 nM to 5 µM, with a NanoDrop 2000, as shown in Figure 4.9c. Absorption values at 280 nm using a 10 mm optical path showed that the NanoDrop 2000 performed well down to 1 µM whereas the measurement was less accurate at lower concentrations. The measured concentrations of 100 nM and 500 nM BSA solutions were 230 ± 100 nM and 600 ± 160 nM, respectively. The error bars depict the variation in the estimated concentration obtained from ten UV-absorption measurement repeats, as shown in Figure 4.9d.

4.4.7 Lysozyme concentration measurements with calibration

Finally, I performed absolute protein-concentration measurements in a label-free manner. For this purpose, I designed and fabricated a microfluidic spray device with two inlets allowing for the simultaneous spray of two fluids, as depicted in Figure 4.10a. A calibration step was readily implemented into the system by first spraying a known concentration solution on a cantilever, recording the deposition gradient, and then repeating the experiment with the analyte of interest without changing the spray alignment. First, I performed the experiment with a 0.05 mg/mL NaCl calibration step followed by 0.2 mg/mL lysozyme deposition as shown in Figure 4.10b. The measured gradients were -9.76 ± 0.4 mHz/s and -40.1 ± 0.4 mHz/s, respectively, giving a ratio of 1 : 4.11 and a concentration estimate of 0.205 mg/mL. Further, I performed a second experiment but instead using a 0.033 mg/mL BSA solution for calibration, followed by 0.1 mg/mL lysozyme, as shown in Figure 4.10c. The measured gradients were -6.31 ± 0.4 mHz/s and -20.0 ± 0.4 mHz/s, giving a ratio of 1 : 3.17 and a concentration estimate of 0.105 mg/mL. These experiments demonstrated that the dry mass-sensing platform is not only a very sensitive label-free single analyte detection technique but also could yield accurate concentration measurements.

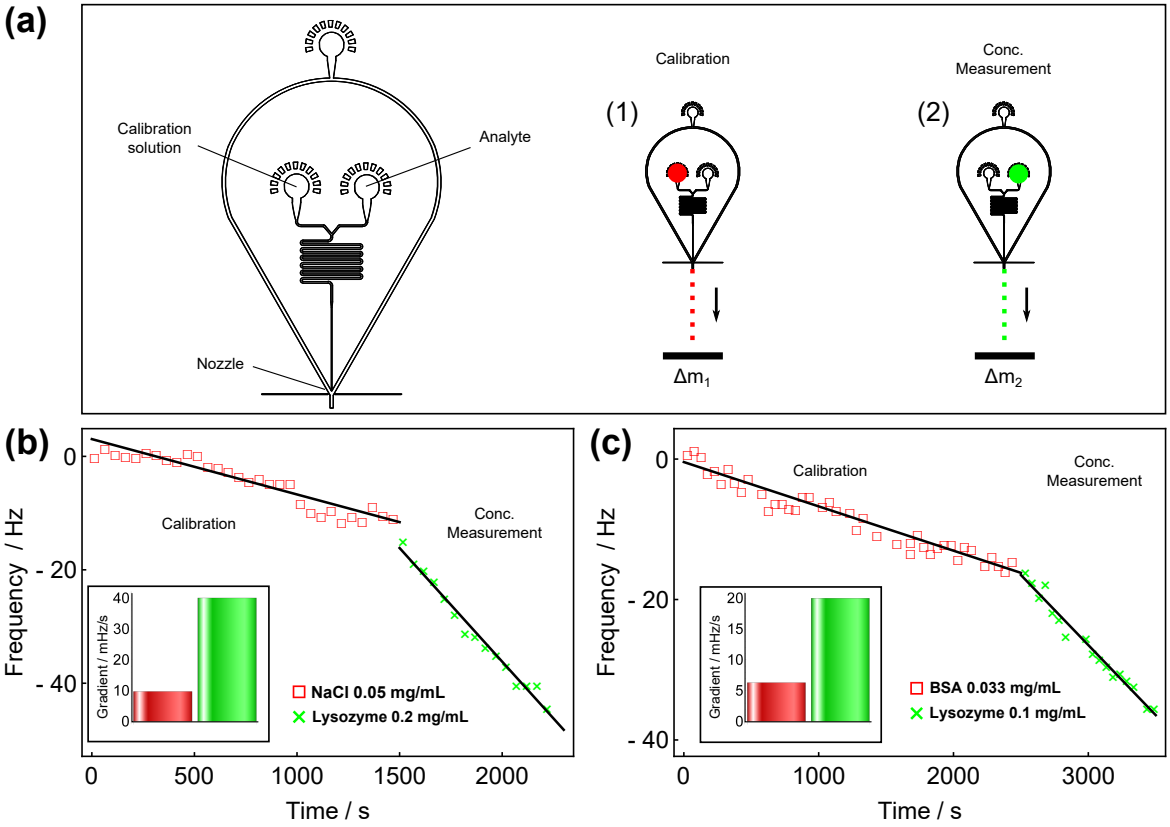

Fig. 4.10 Label-free absolute protein-concentration measurements. (a) A spray device designed for the experiment and the measurement scheme. (b) 0.2 mg/mL lysozyme concentration measurement; the calibration step is performed with a 0.05 mg/mL NaCl solution. (c) The calibration step performed with a 0.033 mg/mL BSA followed by a 0.1 mg/mL lysozyme-solution concentration measurement.

4.5 Conclusions

In this chapter, I have presented a path to address the limitations to MEMS biosensing originating from the low quality factor of micro/nano acoustic resonators operated in liquids. The resonant-frequency measurement system of a MEMS cantilever was built and combined with the microfluidic spray nozzle delivering rapidly evaporating droplets to the cantilever surface. The dry mass of the solute deposited on the surface after the evaporation was calculated by measuring the decrease in the sensor resonant frequency. The system was a demonstration of a flexible interface between the current state-of-art microfluidics and MEMS devices.

The dry mass-sensing approach improved the quality factor by two orders of magnitude relative to operation in liquid, leading to a 370 fg gravimetric limit of detection. I demonstrated mass sensing with a 500 μM NaCl solution, measuring a mass of 24.9 ± 0.8 pg during a 45 s interval. Moreover, I have shown with 100 nM and 500 nM BSA protein solutions that this label-free mass-detection principle was also sensitive to the analyte concentration as well as the sample delivery rate to the MEMS surface. Finally, I determined the mass concentration of a lysozyme solution by performing a calibration step with a sample of known concentration.

The sensing scheme presented in this chapter is in principle compatible with a wide range of gravimetric sensors and, therefore opens up new perspectives for high-resolution biosensing using ultra-sensitive micro/nano-mechanical sensors. It is compatible with many gravimetric sensors and could enable label-free detection of molecules at extremely low concentrations. Since the spray nozzle is based on lithography-enabled microfluidic-fabrication techniques [77], the integration of upstream microfluidic separation [93, 235, 236], mixing [237], or filtering [238] is a suitable route to allow for selective analyte detection. More generally, dry mass sensing could be used in laboratory settings for the concentration measurements of single analytes, replacing or complementing ultraviolet visible light (UV-vis) spectrometers that are typically limited to a concentration of a few micrograms per milliliter and are also analyte dependent. This versatile mass-detection approach may have numerous applications, including analysis of samples of unknown concentration as well as offering other novel possibilities for the label-free sensing community. It will potentially be a very useful complementary tool to protein-sensing techniques exploiting optical [239], biochemical, and electrochemical phenomena [101, 103].

Chapter 5

Label-free protein detection using liquid chromatography combined with QCM

5.1 Summary

Label-free protein detection enables novel diagnostic platform development. However, the interface between standard protein-separation techniques and micro-resonator platforms is often challenged by only a qualitative mechanical-sensor performance in liquids. In this chapter, I describe a strategy to make dry mass sensing a selective protein-measurement strategy. I couple liquid chromatography with a quartz-crystal microbalance (QCM) by using a microfluidic spray dryer. A buffer solution containing a standard protein mixture is first separated on a size-exclusion column. A specific protein fraction is then selected, desalted and subsequently spray-dried onto the QCM for absolute mass analysis. First, I show how to establish a continuous flow interface between the chromatography column and the spray device via a flow-splitter. I then demonstrate gravimetric protein detection with the majority of the sample being fractionated. Finally, I demonstrate that this protein-sensing method is concentration sensitive with a 1 µg/mL limit of detection and, therefore, can be used for quantitative label-free protein-mixture analysis.

5.2 Introduction

Quantitative label-free biomolecular detection is an integral part of a number of industrial processes, as well as basic applied research, in fields ranging from physics to chemistry

and medicine [64, 240–243]. Currently available protein-diagnostic instruments are often challenged to operate with a high dynamic range, detect a variety of biomarkers and yet be scalable and cost efficient [244, 245]. The development of accurate label-free protein detection on micro-technology platforms opens up numerous possibilities for novel instrumentation as well as advancing our understanding of biology [46, 246–248].

Mechanical mass detection is a conceptually simple and robust protein-sensing technique with the potential for unprecedented detection sensitivities shown to be as low as 7 zeptograms [60, 204]. Acoustic resonators, such as cantilevers, can be mass produced and fully integrated within low cost ultra-sensitive sensor platforms [244]. However, such gravimetric sensors are usually difficult to implement in practice for molecular-diagnostics purposes due to their deteriorated sensitivity in liquids as well as the necessity for a specific surface functionalisation enabling protein-selective detection [73, 74, 205, 206, 218]. One of the most commercially successful sensor devices - the quartz-crystal microbalance (QCM) - is an established mass-detection technique for sub-nanogram level of sensitivity [249, 250]. There is a variety of acoustic electromechanical sensors operating in liquids [251–253], integrated with microfluidic flow cells [254, 255] or containing flow-through channels embedded in the sensor [225, 227, 228]. To use the full capabilities of acoustic-sensor performance, there have been a few attempts at dry biological matter detection in a gaseous environment; however, the latter methods lack measurement selectivity or mixture separation [256–258].

Protein separation is necessary for scalable label-free biosensor platforms, extending beyond the detection of a single analyte in solution [259, 260]. There is a variety of established protein-separation techniques, such as capillary electrophoresis [82], liquid chromatography [261] and free-flow electrophoresis [116]. Liquid chromatography (LC) is by far the most widespread protein-separation method in biological research [261], relying on the interaction between the chromatography column stationary phase and the analyte within the liquid mobile phase. The most effective LC methods are size-exclusion [262], reversed phase [263], ion-exchange [264] and affinity chromatography [265].

Here, I present a general strategy to combine conventional protein-separation techniques and micro-resonators. I couple a size-exclusion column with QCM detection through a microfluidic spray nozzle continuously spray-drying the solution on the sensor, as depicted in Figure 5.1. The spray nozzle nebulises the liquid into micron-sized drops [137, 257], and thus enhances the liquid evaporation rate which is essential for continuous surface spray drying. To perform a selective protein sensing within conventional physiological buffers, I incorporated a desalting step [266] after separation and demonstrate a concentration-sensitive dry-mass detection of a standard protein in a mixture. Similar dry-sensing approaches

have been previously presented [256, 257]; however, this is the first demonstration of such detection with separation and desalting steps prior to the dry-mass analysis.

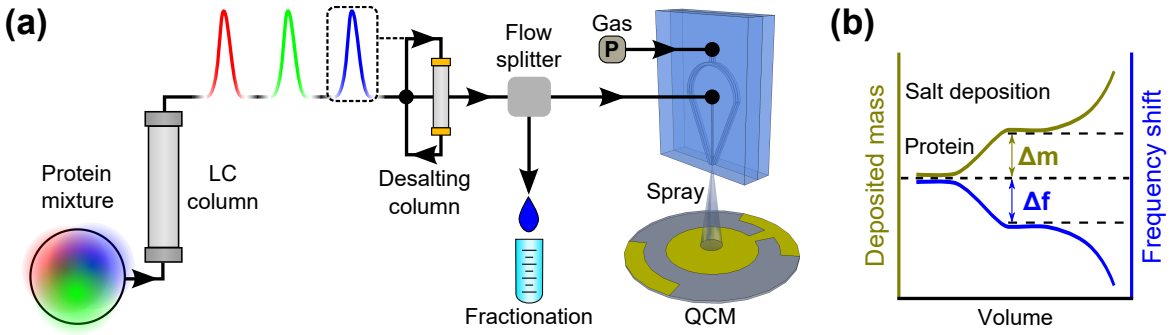

Fig. 5.1 Integration of an LC purification column with gravimetric QCM detection. (a) The protein mixture is separated on the LC column and a specific fraction is selected and injected into a protein-desalting column. The desalted protein fraction then flows via a splitter to a microfluidic nebuliser continuously spray-drying the solution on a QCM. (b) The QCM sensor records a decreasing resonant frequency indicating continuous mass deposition on the surface. The desalted protein fraction causes a sharp frequency decrease followed by a delayed buffer salt deposition enabling selective label-free gravimetric protein-mass detection.

5.3 Materials and methods

In brief, I have combined liquid chromatography with a QCM via a microfluidic nebuliser, as shown in Figure 5.1. A flow-splitter was used to match the high-flow liquid chromatography with the microfluidic spray, operating at an order of magnitude smaller flow rate, allowing for simultaneous sample fractionation and gravimetric analysis. To detect the mass of proteins within physiological buffers, I incorporated a standard desalting column after the main LC column, thus allowing for selective concentration-sensitive protein detection.

5.3.1 Device fabrication

The microfluidic devices were fabricated using a soft-lithography-based [181] two-PDMS layer method, as described in Section 3.3.1. The device contains two inlets: one inlet for the nebulising nitrogen gas and one for the liquid, as shown in Figure 5.2. The liquid channel length was $L_{in} = 8.1$ mm with a cross section of $25 \times 20\ \mu m^2$ and the two curved gas channels

of length $L_{gas} = 8.4$ mm had a cross section of 100×100 μm^2. The device with a non-wetting 3D junction was made by plasma bonding two PMDS complementary replicas with tall gas channels on each side and the smaller height liquid channel on one of the replicas [257]. Finally, the assembled PDMS device was cut with a razor blade to produce the device orifice. This configuration allowed for the emerging liquid to be surrounded by a gas flow to transport the fluid outside the nozzle through a jet without wetting the PDMS surface. The device gas inlet was connected to a compressed nitrogen cylinder with a pressure regulator typically set to 3 bar and the liquid inlet was connected to an outlet of a flow-splitter.

5.3.2 LC sample separation and desalting

To demonstrate the functionality of the method, I have selected a mixture of three proteins from a high molecular-weight standard kit (GE Healthcare, 28-4038-42): bovine thyroglobulin (670 kDa), rabbit aldolase (158 kDa) and chicken ovalbumin (43 kDa). The proteins were diluted in a 7.3 pH PBS buffer of total volume 40 μL. The concentration of thyroglobulin was varied between $0.5 - 2$ mg/mL, while the concentration of aldolase and ovalbumin was fixed to 1 mg/ml.

A 7.3 pH PBS buffer was used for the sample elution through a Superdex 200 Increase 3.2/300 column (GE Healthcare, UK). The LC flow was varied around a typical value of 25 μL/min and controlled by an ÄKTA Pure System (GE Healthcare, UK). I monitored the eluting sample absorbance at 280 nm with a 10 mm path-length absorption monitor U9-M (GE Healthcare, UK) and the solution conductivity was measured with a conductivity monitor C9 (GE Healthcare, UK). Protein desalting was carried out with a water-filled HiTrap desalting column (GE Healthcare, 17-1408-01), connected in bypass with the main flow path. Once the protein to be desalted was injected into the desalting column, the flow was connected to the microfluidic flow-splitter.

5.3.3 Flow-splitter

A microfluidic flow-splitter comprising of a Y split (P-512, IDEX Health & Science) with carefully pre-cut polyether ether ketone (PEEK) capillaries (IDEX Health & Science) and a flow sensor MF2 (Elveflow) was built, splitting only a fraction (typically $\sim 15\%$) of the flow coming from chromatographic separation into the microfluidic spray device, as shown in Figure 5.2c. The fractionator output was made of a capillary with $L_f = 32.4$ cm and 67.8 μm ID, giving a hydraulic resistance $R_2 = 5.57 \cdot 10^{14}$ Pa·s/m^3 (calculated using Equation 1.4).

The capillary connecting the splitter to the spray was of length $L_s = 10$ cm and 125 µm ID, giving a hydraulic resistance of $1.5 \cdot 10^{13}$ Pa·s/m^3 (calculated using Equation 1.4). However, the on-chip resistance of the narrow liquid channel could be estimated to be $8.8 \cdot 10^{14}$ Pa·s/m^3, which was calculated using Equation 1.5. Therefore, the resistance on the spray device should dominate the total hydraulic resistance R_1 of the liquid flow path to the spray.

Assuming the pressure at the splitter is P_T, the total flow Q_{LC} is distributed between the spray nozzle (pressure P_S, flow Q_1 and resistance R_1) and the fractionator outlet (atmospheric pressure P_0, flow Q_2 and resistance R_2). By flow conservation at the splitter:

$$Q_{LC} = Q_1 + Q_2 = \frac{P_T - P_S}{R_1} + \frac{P_T - P_0}{R_2} \tag{5.1}$$

Then, the liquid flow to the spray can be expressed as:

$$Q_1 = \frac{P_T - P_S}{R_1} = \frac{R_2}{R_1 + R_2} Q_{LC} - \frac{P_S}{R_1 + R_2} \tag{5.2}$$

indicating a linear relationship between Q_1 and Q_{LC}. Using the values stated above, I estimated the gradient and the intercept to be $R_2/(R_1 + R_2) = 0.38$ and $-P_S/(R_1 + R_2) = -740$ µL/h, respectively.

5.3.4 QCM setup

I used commercially available 5 MHz resonant-frequency QCM crystals (Stanford Research Systems 100RX1, Cr/Au) for the gravimetric analysis. Crystal resonant-frequency monitoring was performed with a frequency counter (Stanford Research Systems QCM200) with a gate time of 1 s, leading to a frequency stability of 0.1 Hz in a stabilised environment. The first electrode of the QCM sensor has an area of 1.37 cm^2; however, the active electrode oscillation area is confined to 0.40 cm^2 by the geometry of the second electrode. The Sauerbrey [249] equation can relate the change in the resonant crystal frequency Δf_q to the mass changes on the surface Δm_q:

$$\Delta f_q = \frac{2 f_q^2}{A \sqrt{\rho_q \mu_q}} \Delta m_q \tag{5.3}$$

were f_q is the resonant frequency of the crystal and ρ_q and μ_q are the density and shear modulus of quartz, respectively, giving the mass sensitivity coefficient $\Delta f / \Delta m = 0.1415$ Hz/ng. The sensor crystals could be easily reused by washing them with soap and isopropyl alcohol after each use.

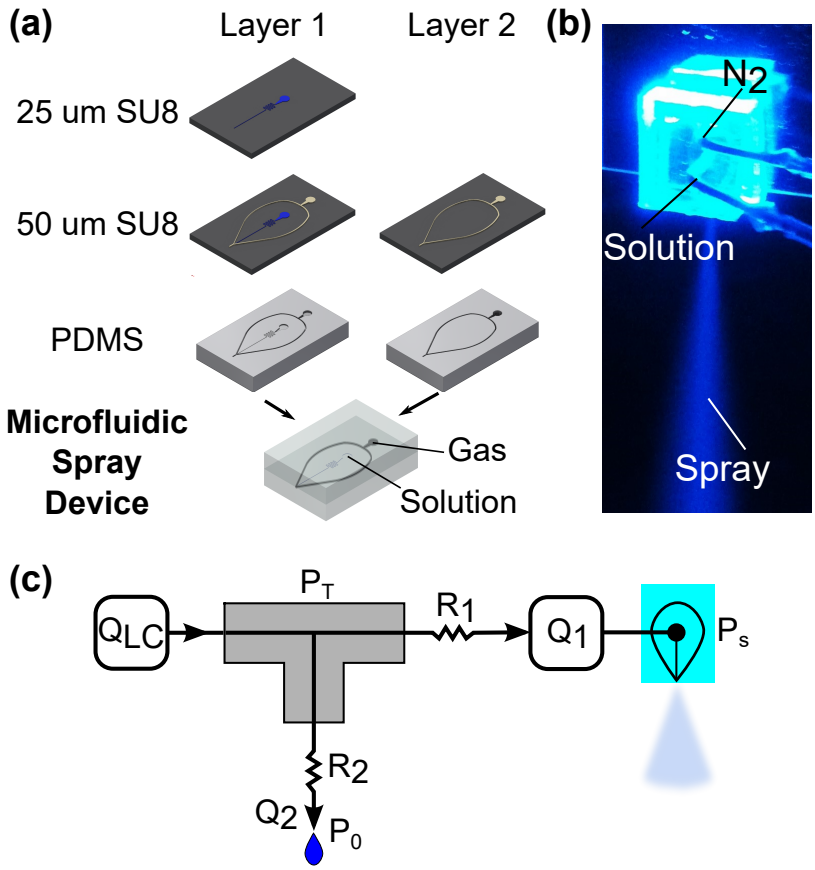

Fig. 5.2 (a) The microfluidic spray device fabrication steps consist of two complementary photo-lithographically defined SU-8 mould production (step 1), PDMS soft-lithography of the moulds (step 2), and assembly of the two PDMS replica layers via plasma bonding (step 3). (b) Optical image of the microfluidic spray nozzle in operation (illuminated by a blue LED). The device has two inlets: one for the compressed gas and one for the solution to be nebulised. (c) Flow-splitter schematics. The splitter has two manufacturer calibrated capillaries determining the fraction of the total flow incoming from LC separation, split between the spray nozzle and the fractionation outlet. The flow Q_1 through the spray nozzle is monitored with a flow sensor.

5.4 Results and discussion

5.4.1 Online spray control

LC separation typically operates at $0.1 - 1$ mL/min flow, while an average microfluidic device flow is around $1 - 10$ µL/min, presenting a mismatch over a few orders of magnitude. In this section, I explain how I used a flow-splitter to couple the two types of systems.

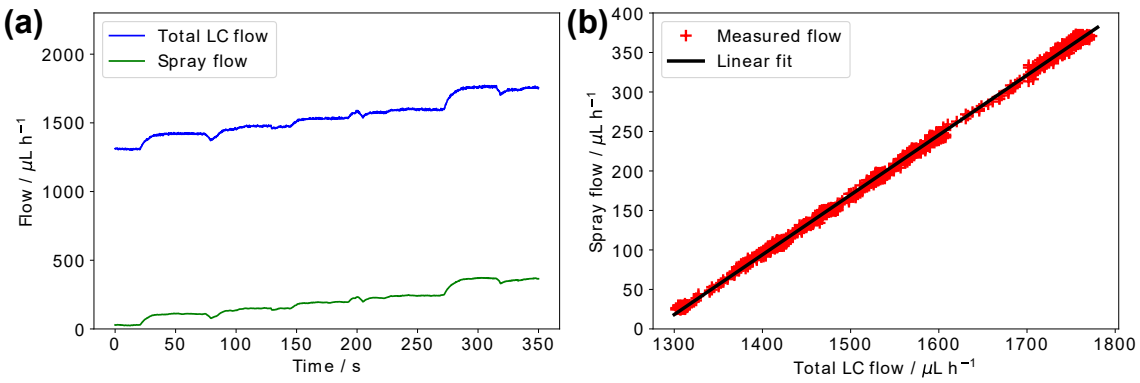

Fig. 5.3 Flow-splitter performance and calibration. (a) Flow from the LC column is varied and the flow through the spray nozzle, connected to a 3 bar pressure, is monitored. (b) Plotting the spray nozzle liquid flow versus the total flow reveals a linear relationship, allowing for flow calibration and the split ratio prediction.

The total flow incoming to the splitter was varied between 1300 µL/h and 1800 µL/h and I measured the flow to the spray nozzle, as shown in Figure 5.3a. I observed a direct correlation between the two flows; therefore, by plotting the flow through the spray nozzle versus the total flow, I detected a linear relationship, as presented in Figure 5.3b. The least-square fit gave an estimate for the gradient $R_2/(R_1+R_2) = 0.7578 \pm 0.0006$ and the intercept $-P_S/(R_1+R_2) = -967 \pm 1$ µL/h . I could thus observe a difference of the latter values from the initially expected parameters for the gradient and intercept of $m = 0.38$ and $c = -740$ µL/h. This discrepancy occurred due to the fact that, at high pressures, PDMS deforms; thus the nozzle liquid channel expanded which significantly reduced the on-chip resistance. Assuming that the PEEK capillary resistance R_2 did not change, I obtained a value for the spray inlet hydraulic resistance to be $R_1 = 1.8 \cdot 10^{14}$ Pa·s/m^3 which was about 5 times smaller than the expected value, indicating about 120% channel cross-sectional area expansion (hydraulic resistance scales as $\sim 1/A^2$). Then using the corrected R_1 value, I estimated the pressure at the nozzle orifice to be $P_S = 2$ bar, showing that there is about 1 bar gas pressure gas drop along the gas flow path on-chip. Overall, I have established a predictable, linear flow-splitting performance; nevertheless, I still monitored the spray flow during all the experiments due to a slight device-to-device variation.

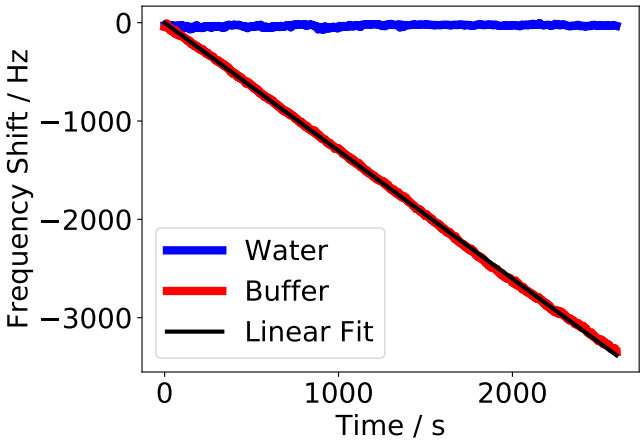

Fig. 5.4 QCM mass-deposition calibration. A 0.4 mg/ml NaCl solution is sprayed at a known flow rate on the sensor, thus resulting in a linear frequency decrease trend. This indicates a constant mass deposition rate and a linear frequency response to mass loading for the dry mass of deposits in air.

5.4.2 Detection of calibration solution

QCM sensors are known to have a complex frequency response as a function of mass loading in liquids [74]. However, in this case, I covered the sensor surface with a uniform film of deposits, thus creating a linear response. I verified this by spraying a 0.4 mg/mL NaCl buffer solution at a constant rate while observing the sensor frequency change, as shown in Figure 5.4. I observed a linear frequency decrease trend with a gradient of -1.3015 ± 0.0006 Hz/s, which gave a mass deposition rate of 9.2 ± 0.004 ng/s when using the frequency-to-mass relationship (Equation 5.3). The flow through the spray nozzle was measured to be $Q_s = 141.5 \pm 8.4$ µL/h; thus, the expected mass deposition rate was 15.7 ± 0.93 ng/s. Taking the ratio of the two, I obtained the calibration factor of 58.5 ± 3.5 % which originates from the fact that not all of the mass, deposited on the surface, landed on the sensitive QCM electrode area.

5.4.3 Separation and desalting

I first separated thyroglobulin, aldolase and ovalbumin mixture (all proteins at a concentration of 1 mg/mL) at a flow of 26 µL/min, as shown Figure 5.5a. I then bypassed the flow between volumes 0.9 mL and 1.3 ml and injected the purified thyroglobulin solution into a water-filled desalting column. The protein was desalted and eluted from the desalting column

approximately between 1.1 mL and 2 mL of the desalting volume after the flow bypass. The volume range was determined by taking 99 % of the total protein amount. I confirmed that the buffer salts were delayed by the desalting column with a conductivity measurement, as illustrated in Figure 5.5b. Then, the purified and desalted protein solution was injected into the flow-splitter, resulting in a flow through the spray device of $Q_s = 215.2 \pm 9.5$ µL/h, giving a ratio of 13.8 ± 0.61 % of the total sample being spray dried on the QCM and about 86 % of the total sample fractionated. As expected, I observed a rapid QCM resonant-frequency decrease due to the protein deposited on the sensor surface between previously determined volumes of 1.1 mL and 2 mL. Then, a gradual deposition of the buffer salts was observed, as shown in Figure 5.5c, confirming that the protein solution was desalted. As a result, I measured the QCM frequency shift between volumes of 1.1 mL and 2 mL to be 488 ± 33 Hz, indicating a detected mass amount of 3.45 ± 0.23 µg.

5.4.4 Label-free thyroglobulin detection

I verified that this protein-selective detection method is sensitive to protein concentration. Four protein mixtures with thyroglobulin concentrations varying between 0.5 mg/mL to 2 mg/mL were prepared and thyroglobulin purification, desalting and dry-mass detection was carried out. The desalted protein peak deposited on the QCM caused frequency decreases of 264 ± 51 Hz, 488 ± 33 Hz, 700 ± 29 Hz and 875 ± 38 Hz for thyroglobulin concentrations of 0.5, 1, 1.5 and 2 mg/mL, respectively (see Figure 5.6a). The frequency shifts correspond to the detected dry mass of protein of 1.87 ± 0.36 µg, 3.45 ± 0.23 µg, 4.95 ± 0.20 µg and 6.19 ± 0.27 µg, respectively.

To estimate the predicted protein amount landing on the sensor surface, I considered the total mass within 40 µL of the injected sample and multiplied it by the previously obtained 0.138 ± 0.006 flow-splitting ratio and a fraction of 0.585 ± 0.035 landing on the sensitive QCM area. Thus, the expected proportion of the total injected protein sample is 8.1 ± 0.6 % giving a gradient of 3.23 ± 0.24 µL in the detected mass versus the protein concentration plot, as shown in Figure 5.6b. By plotting the measured values together with the predicted gradient, I could conclude that the measured protein masses agreed well with the predicted protein amounts.

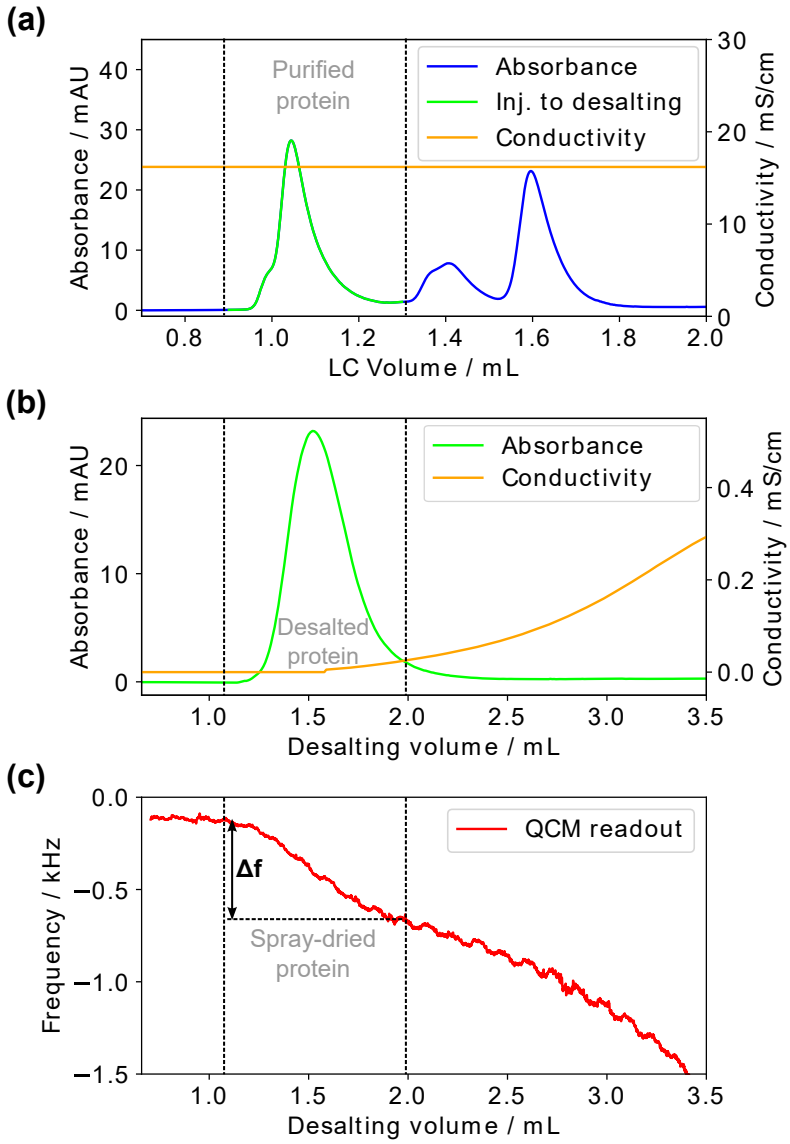

Fig. 5.5 Protein mixture separation and desalting. (a) Thyroglobulin, aldolase and ovalbumin mixture is separated on the LC column in PBS buffer. (b) The first well-separated peak, identified as thyroglobulin, is selected and injected into a protein-desalting column. The buffer salts are delayed, as expected, showing a delayed gradual conductivity increase. (c) Finally, I deposit the desalted protein solution onto a gravimetric QCM sensor showing a non-linear mass deposition rate. The first frequency jump is caused by the desalted protein and the subsequent frequency decrease trend arises due to the delayed buffer salt deposition. As the salt concentration increases, so does the rate of the QCM frequency change.

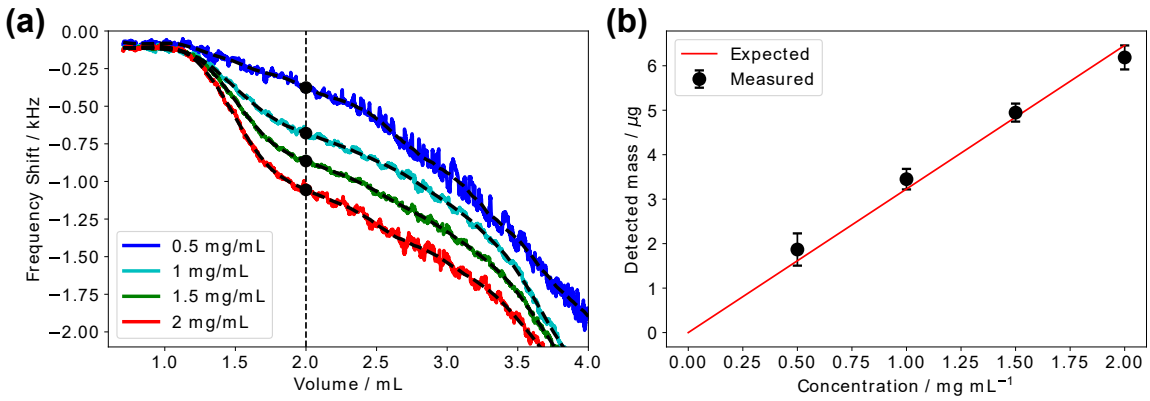

Fig. 5.6 Selective label-free gravimetric thyroglobulin detection. a) The QCM frequency response during the desalted thyroglobulin deposition depends on the initial protein concentration within the mixture. b) By quantifying the deposited thyroglobulin amount and plotting it against the initial protein concentration, we observe a linear trend. The predicted mass is estimated by using the previously obtained flow-split ratio and the spray calibration.

5.4.5 Limits of detection

Finally, I quantified the LOD of the method presented in this chapter, by estimating the variation of the amount of the water droplets on the sensor surface. I measured the standard deviation of frequency fluctuations, compared to a smoothed frequency trend, and obtained a standard deviation of around $f_{noise} = 30$ Hz. The frequency change was obtained by taking the difference between two points, each with an error of 30 Hz, so the total error in the difference was $30\sqrt{2} \approx 42$ Hz which corresponded to the minimum measurable mass of 0.3 µg. By combining this value with the protein calibration obtained above, I estimate the smallest reliably detectable protein concentration presented in this study to be 0.1 mg/mL. However, by improving on the desalting performance and gating the spray deposition time followed by sensor equilibration, the minimally detectable frequency shift is approximately 0.1 Hz (specified by the manufacturer), leading to a 1 µg/mL detection level.

5.5 Conclusions

This work presents a path for performing a selective label-free protein sensing using micromechanical sensors. I combined liquid chromatography with gravimetric QCM detection via a microfluidic spray nozzle. To this effect, I separated a standard protein mixture containing

three model proteins - thyroglobulin, aldolase and ovalbumin. I then selected thyroglobulin as my gravimetric analysis target. After a subsequent buffer-desalting step, I fractionated 86 % of the total sample while using only 14% of the total volume for gravimetric QCM analysis. I demonstrated an on-line chromatography and microfluidic spray combination using a carefully calibrated flow-splitter. The mass-detection principle was verified to be linear to the mass loading with an inorganic salt solution. I then demonstrated that the measurement of the purified and desalted thyroglobulin is quantitative by varying its concentration within the mixture. Finally, based on the minimal frequency noise, I estimated the limit of concentration detection for this label-free protein detection method to be 1 μg/mL.

The sensing scheme presented here is compatible with a wide variety of acoustic gravimetric sensors and opens up opportunities for selective label-free protein detection. A different protein-separation technique could be used, for example, micro-free flow electrophoresis [117], which could be even integrated onto the spray chip and make the whole system footprint significantly smaller. Finally, it would be possible to carry out the spray deposition and QCM detection in a depressurised chamber to enhance evaporation as well as improve the sensor quality factor.

Chapter 6

Multidimensional protein characterisation using LC combined with microfluidics

6.1 Summary

Extensive biophysical characterisation of heterogeneous protein mixtures remains challenging in modern protein science and relies heavily on the quality of separation and purification of individual species. However, proteins are highly dynamic complex polymer systems; therefore, instant measurements of major mixture component characteristics are critical. In this chapter, I describe how analytical microfluidics can be combined with liquid chromatography to characterise biomolecules of a complex mixture in the condensed phase directly after the separation. First, I separate the mixture with a size-exclusion chromatography column and then distribute the flow between a sample fractionation outlet, recovering 90% of the sample volume, and multiple microfluidic devices measuring the molecular size, electrophoretic-mobility and effective charge of the separated species. I demonstrate the operational principle of our approach with a mixture of three standard unlabelled proteins varying in size and charge. Then, I extend the analytical potential of the system by analysing a mixture of streptavidin, biotinylated BSA and fluorophore Atto-488, which forms stable labelled intermediates with diverse biophysical properties. The multidimensional results of this new platform show that I can characterise heterogeneous mixtures and identify the molecules abundant in the mixture.

Parts of this work previously appeared in:

GB 1815360.1 (application filed 2018) Improvements in or relating to profiling of particles using microfluidic devices.

6.2 Introduction

Understanding protein-protein interactions is a key problem in modern proteomics. To probe and predict these interactions, we need to be able to determine individual, fundamental biophysical properties of proteins, such as isoelectric point [267], hydrodynamic-radius [268], hydrophobicity, molecular weight, stoichometry of binding partners and binding affinity.

One of the most powerful methods capable of identifying components of heterogeneous mixtures is mass spectrometry, which transfers an analyte from liquid to gas phase and separates the mixture components according to their mass-to-charge ratio. The most popular Bottom Up approach, entailing enzymatic or chemical digestion of proteins prior to mass spectrometry, suffers from protein-identification inference problems [269]. On the other hand, Top Down mass spectrometry solves these problems with the denatured intact protein injected into the detection chamber and it allows for the detection of a large number of the proteins present in human cells [269, 270]. Although these conditions are gentle enough to preserve covalent bonds, most of the biologically relevant non-covalent protein-protein and protein-ligand interactions are diminished. Finally, due to the measurement in the gas phase, mass spectrometry provides only limited information about the properties of native proteins [271].

A separation step before the mass-spectrometry analysis can greatly improve the measurement resolving power. One of the most widespread methods for the separation of proteins, protein complexes and peptides in their native state is liquid chromatography (LC) [261]. It relies on controlling the interaction between the chromatography column stationary phase and the analyte within the mobile phase. The most widespread of existing LC methods - size-exclusion [262], reversed phase [263], ion-exchange [264] and affinity chromatography [265] - have been combined with the Bottom Up mass spectrometry and used for mapping out physiological protein complexes from endogenous samples [272, 273].

There is a great variety of other protein-characterisation methods able to determine protein properties in solution. Such examples could be nuclear magnetic resonance spec-

troscopy [274], circular dichroism [29], isothermal titration calorimetry [275], fluorescence spectroscopy [276], dynamic light scattering [277], multi-angle light scattering [278], gel electrophoresis [279] and analytical centrifugation [280]. When combined with molecular-separation techniques (on-line and off-line), the latter methods can yield the full characterisation of individual components and complexes in heterogeneous solutions. Unfortunately, most of the currently existing analytical methods can only measure a single attribute, such as molecular mass, Stokes radius or charge, at a time and this reduces the molecular profiling throughput. Therefore, a number of experiments are needed to fully characterise protein mixture in terms of the most common biophysical properties.

Microfluidics, also known as Lab-on-chip, is an interdisciplinary field involving manipulation and control of small quantities of fluids, usually in the range of picoliters to microliters, in microfabricated structures [77]. Microfluidic systems have superior properties to bulk flow-measurement techniques and can greatly reduce the measurement time, cost, sample volume, while increasing throughput and measurement capabilities. Such examples are diffusional sizing [101, 102, 281, 282], free-flow electrophoresis [117, 118, 283, 284] , capillary electrophoresis [285] and microscale thermophoresis [286]. Due to the compact footprint, microfluidic systems can be used to parallelise protein-characterisation experiments greatly reducing the measurement time and improving reliability.

Here, I present an interface which combines LC protein separation with microfluidics, enabling simultaneous sample fractionation and multidimensional separated molecule characterisation on one chip. The platform contains a scalable microfluidic flow adapter, which matches the two system flows over a few orders of magnitude and distributes the incoming flow from an LC column to a sample fractionation outlet and an arbitrary number of parallel microfluidic analytical devices. LC has already been combined with various analytical techniques via flow splitting or direct coupling: LC - mass spectrometry [287], LC - nuclear magnetic resonance spectroscopy [288], LC - capillary electrophoresis [289], LC - free flow electrophoresis [290] and LC - droplet microfluidics [291].

In this particular study, I demonstrate coupling between an LC column with two microfluidic devices simultaneously measuring the hydrodynamic-radius [99, 101, 102, 281, 282, 292], the electrophoretic-mobility and the effective charge [117, 118, 283, 284, 293], as depicted in Figure 6.1. Similar microfluidic devices have been demonstrated to work separately or in series [294]; however, this is the first attempt coupling LC with a highly paralellised microfluidic analytical device performing simultaneous protein size and effective charge measurements on a single chip.

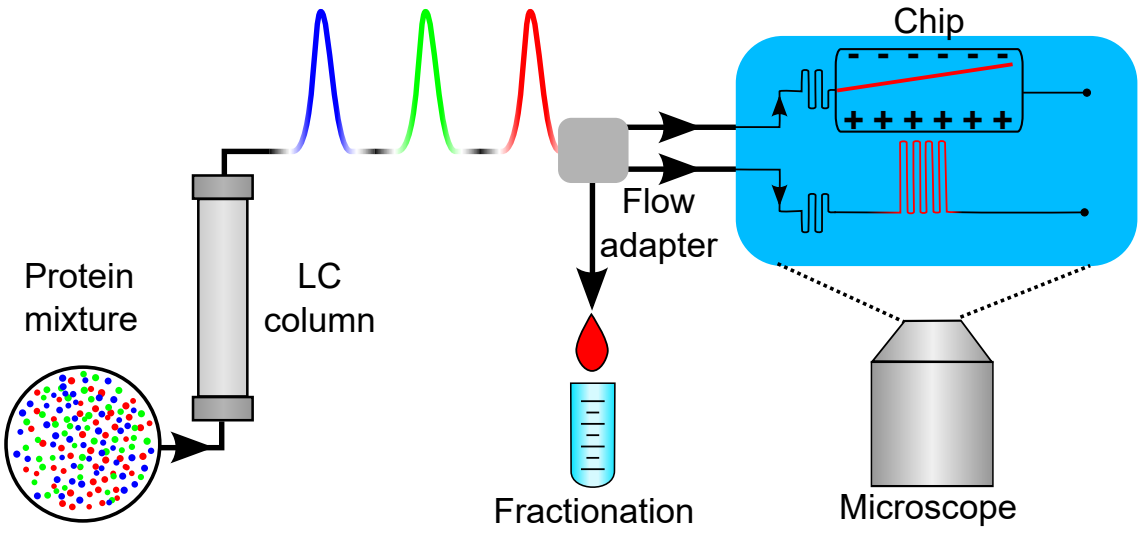

Fig. 6.1 Integration of an LC purification column with analytical microfluidics. The protein mixture is separated on the LC column and connected to a low-flow microfluidic chip via a flow adaptor. A small proportion of the sample is used for continuous measurements of hydrodynamic-radius and effective charge, while the majority of the sample is fractionated for post-separation uses.

6.3 Materials and methods

6.3.1 Analyte mixtures

To demonstrate the functionality of the method, I selected a mixture of three proteins varying in size and isoelectric point (pI): bovine thyroglobulin ($M_w = 670$ kDa, $pI = 4.5$, GE Healthcare, 28-4038-42), chicken conalbumin ($M_w = 76$ kDa, $pI = 6.7$, GE Healthcare, 28-4038-42,) and chicken lysozyme ($M_w = 14.3$ kDa, $pI = 9.3$, Sigma-Aldrich, L6876) as depicted in Figure 6.2a. The proteins were diluted in a 100 mM sodium HEPES buffer (7.3 pH) at a ratio of 4.6 : 33 : 110 µM, respectively. The total sample volume was 40 µL.

The second system that I used to generate a heterogeneous sample was based on streptavidin-biotin complex formation - one of the strongest known non-covalent interactions between a protein and a ligand. I prepared the mixture by incubating Streptavidin (Prospec, Israel, PRO-791), biotinylated bovine serum albumin (Generon, UK, 7097-5) and a biotinylated Atto-488 (ATTO-TEC GmbH, Germany) dye at a ratio of 1 : 1 : 3 (20 : 20 : 60 µM, total volume 40 µL) for 1 h at room temperature in 10% phosphate buffered saline solution (0.1xPBS, 7.3 pH). The mixture was expected to form seven distinct complexes with sizes ranging from 1 kDa to 300 kDa, as shown in Figure 6.2b. Five of the complexes (I-V) contained an

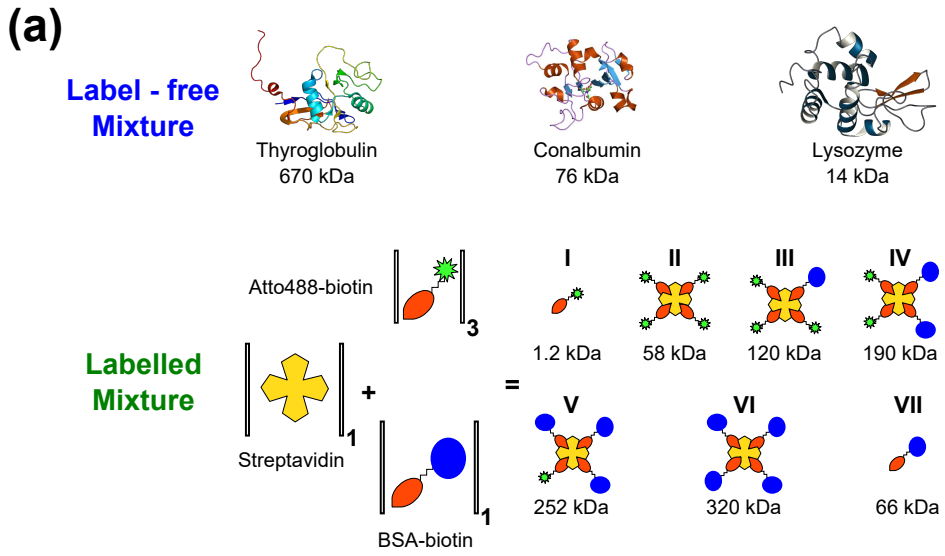

Fig. 6.2 Protein mixtures used for system functionality demonstration. (a) The label-free mixture contained thyroglobulin, conalbumin and lysozyme. (b) The second heterogenous 7-component mixture, which is prepared by mixing streptavidin, biotinylated BSA and Atto-488 molecules, contains five Atto-488 labelled complexes (molecules I-V).

Atto-488 fluorophore and, therefore, the latter molecules were the focus of detection and analysis.

6.3.2 LC separation

Two different buffers were used for the sample elution through the column. First, I used a 100 mM sodium HEPES buffer (7.3 pH) for the label-free sample characterisation and streptavidin-biotin mixture was eluted in a 0.1xPBS (7.3 pH) buffer. Both buffers also contained 0.01% Sodium azide and 0.1% Tween to reduce sample sticking to microfluidic channels. A Superdex 200 Increase 3.2/300 column (GE Healthcare, UK) at a flow of 10 µL/min was used on an ÄKTA Pure System (GE Healthcare, UK). I monitored the eluting sample absorption at 280 nm and 500 nm wavelengths simultaneously with a 10 mm path-length absorption monitor U9-M (GE Healthcare, UK). The absorption intensity was used for matching the molecular elution volume with the image sequence on a fluorescence microscope. The flow from the LC separation was connected to the microfluidic flow adapter.

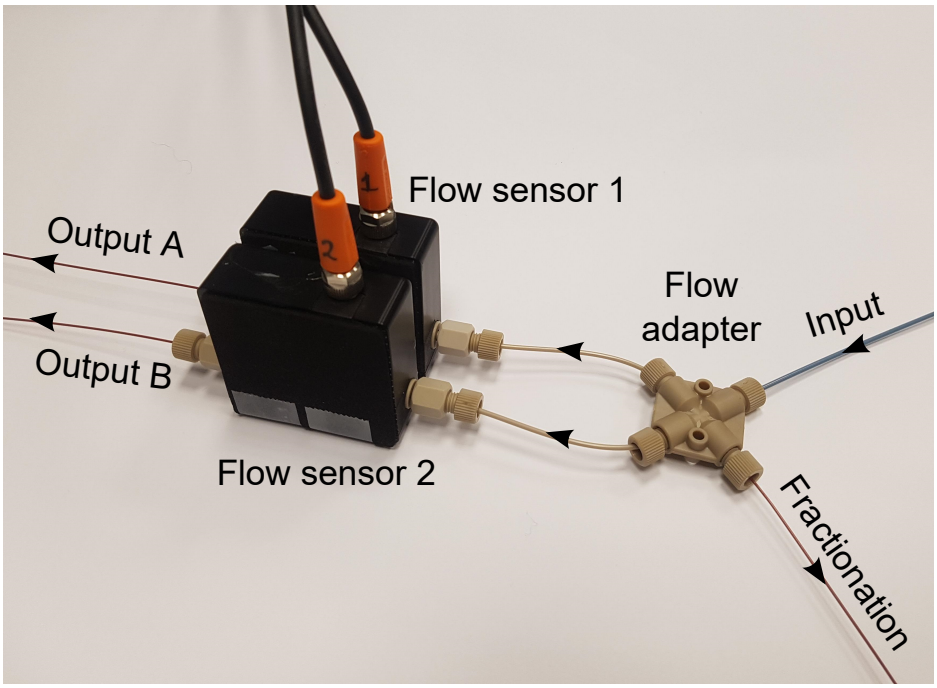

Fig. 6.3 Microfluidic flow adapter matching the flow between LC and microfluidics over two orders of magnitude. The flow is split between the fractionation outlet and outputs A and B; the flow through the outlets A and B is monitored with flow sensors.

6.3.3 Microfluidic flow adapter

A microfluidic junction (P-722, IDEX Health & Science, USA) with carefully pre-cut polyether ether ketone (PEEK) capillaries (IDEX Health & Science, USA) and flow sensors was built, directing only a fraction of the flow coming from chromatographic separation into multiple microfluidic devices, as depicted in Figure 6.3. The lengths of the capillaries were as follows: the fractionator output was made of a capillary with $L_f = 10.2$ cm and 125 µm ID and the outputs A and B were made of two capillaries ($L_1 = 10$ cm with 125 µm ID and $L_2 = 8.1$ cm with 67.8 µm ID. Outputs A and B were connected to microfluidic devices operating at flow rates close to a few 100 µL/h. In general, the flow from the LC protein separation can be in the range of 10 µL/min - 1 mL/min (600 µL/h - 60 ml/h), depending on the pressure and column used and, therefore the capillary resistances have to be fine tuned for the desired flow-splitting ratio.

6.3.4 Microfluidic chip design and operation

The microfluidic device was custom designed for fitting two distinct analytical blocks in one fluorescence-microscope field of view. The first block - the diffusional-sizing device - had a long diffusion channel of length $L_D = 43$ mm, width of $W_D = 300$ µm and height of $H_D = 55$ µm, as shown in Figure 6.4. The positions for the diffusion-profile acquisition were chosen to allow a high sizing dynamic range and fixed to distances of 3.1 mm, 8.8 mm, 12.4 mm, 17.9 mm, 21.5 mm, 36.7 mm and 40.3 mm from the sample injection point. I injected a degassed co-flow buffer (same as the LC mobile phase) at a 290 µL/h flow rate with a neMESYS syringe pump (CETONI GmbH, Germany) into port 5 of the device. Then Outlet A from the microfluidic flow adapter was connected to the sample inlet (port 6) on the diffusional-sizing device. I recorded the injected sample diffusion-profile and performed a fit to the numerical diffusion simulations [102, 295]. By combining liquid chromatography and diffusional sizing in-line, I was able to separate the mixture and determine the diffusion constant D (and the hydrodynamic-radius) of the separated mixture components eluting from the column.

The second component of the microfluidic chip was a free-flow electrophoresis device with liquid electrodes [117]. It was designed to create up to 30 V/cm transverse electric fields on chip while avoiding bubble formation and electrolysis product build up. I injected a highly conductive 3 M KCl electrolyte solution to ports 1 and 4 (see Figure 6.4a) at flow rates of 150 µL/h. A degassed buffer (same as the LC mobile phase) was injected at the port 2 at a flow rate of 300 µL/h using the neMESYS syringe pump and, finally, the output B from the fluidic adapter was connected to port 3 of the free-flow electrophoresis device. Hollow metal 1.5 mm ID electrodes were inserted into device ports 8 and 9 where a power supply (EA Elektro-Automatik 6230207, Germany) was connected to the chip via a multimeter (Agilent 34410A, USA) recording a current flowing through the circuit (see Figure 6.6). By measuring the sample deflection in the electrophoresis chamber in a transverse electric field, I estimated the electrophoretic-mobility of a charged particle μ_e, which will be explained in the following section.

The two microfluidic devices were operated continuously and a measurement of the hydrodynamic-radius, electrophoretic-mobility and charge were obtained for every 3.3 µL of the eluting sample (every 20 s) from the column, while still fractionating 90% of the total volume.

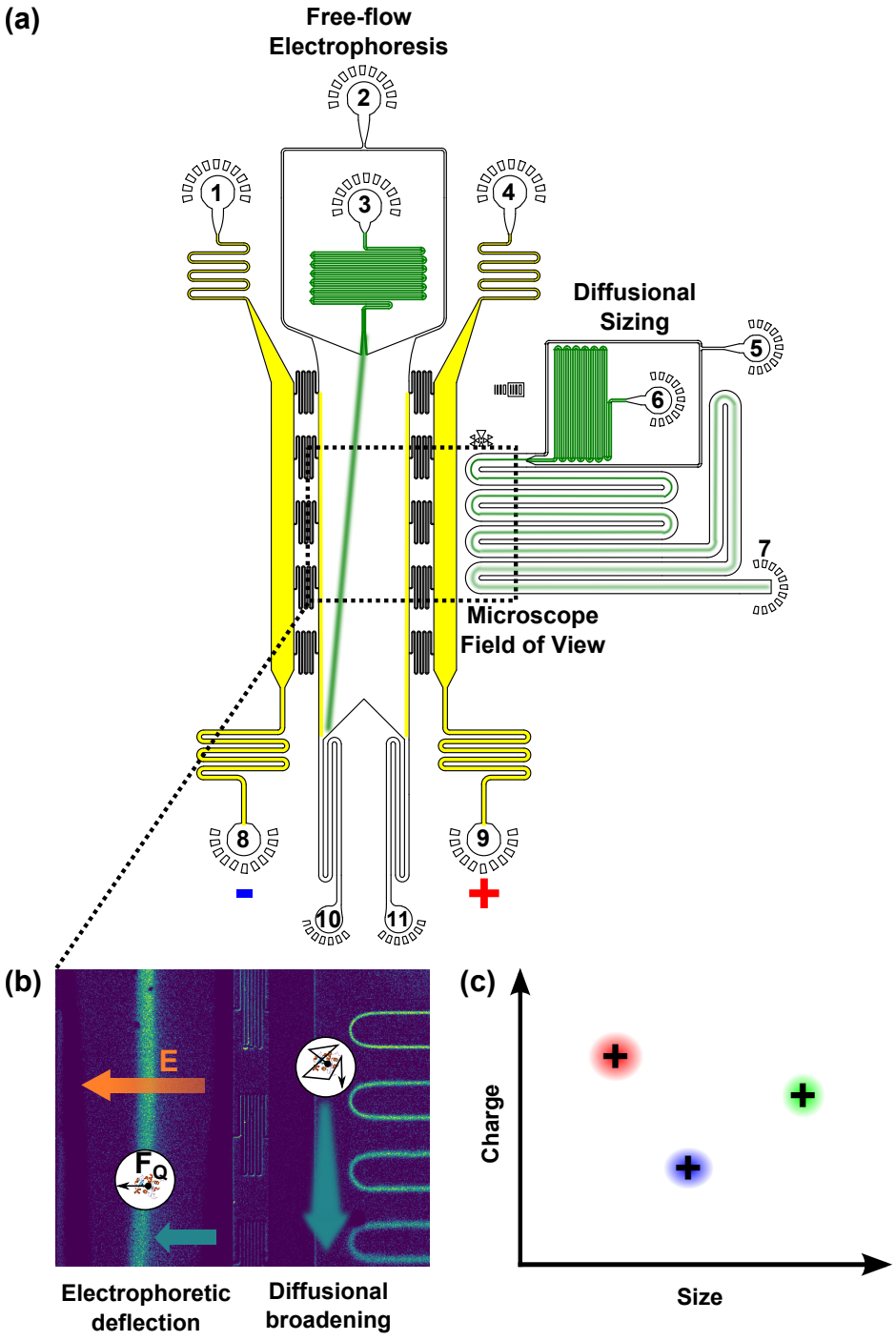

Fig. 6.4 (a) The microfluidic chip containing two functional blocks: diffusional sizing and free-flow electrophoresis. The device has 11 ports and is used for continuous on-line measurements of individual molecule hydrodynamic-radius, electrophoretic-mobility and effective charge using a single field-of-view device. (b) Microscope image of the microfluidic chip measuring protein hydrodynamic-radius and electrophoretic-mobility. (c) The latter measurements can be combined to yield an effective charge estimate. The mixture component characteristics can be visualised in a continuous 2-dimensional charge versus size map of the species present in the mixture.

6.3.5 Diffusional Sizing

The diffusional-sizing method simulations and fitting has been developed by Quentin Peter.

The hydrodynamic-radii analysis had two important parts: the diffusion-profile extraction and the profile fitting. The image processing started by removing the background using image alignment in the Fourier plane. The curve, caused by the non-uniform illumination intensity, was removed by multidimensional polynomial fitting. The channel edge positions and image rotation angle were detected and corrected automatically using an FFT-based technique [296]. The noise was then reduced by spatial averaging along the channel before extracting the profiles at 7 predefined positions along the diffusion channel. Then, a set of basis functions, predicting the diffusion profiles of predefined sizes (diffusion coefficients), was generated with a high-performance algorithm [104, 295, 297]. Finally, a fit deconvolving the measured experimental profiles into a linear combination of the simulated basis functions was computed using a least-squares error algorithm. The fit interpolation yielded the average eluting analyte hydrodynamic-radius with the associated error. An example of a profile fit to the experimentally measured diffusion flow pattern is shown in Figure 6.5. The main profile diffusion simulation equations are presented in Appendix C.

6.3.6 Electrophoresis device calibration and mobility analysis

I performed the mobility measurements, while recording the current flowing through the circuit I at a voltage of $V_0 = 60$ V applied to the electrophoresis device electrodes. To calibrate the device, I filled the device electrophoresis chamber with the conductive electrolyte solution, effectively shorting the chamber ($R_{ch} \approx 0$), and measured the current I_0 while applying the same voltage V_0. Then, considering Ohm's law, I deduced $V_0 = I(R_{elec} + R_{ch})$ and $V_0 = I_0 R_{elec}$ (see Figure 6.6). The voltage drop across the electrophoresis chamber could be expressed as:

$$\Rightarrow V = IR_{ch} = V_0 - IR_{elec} = V_0 - IV_0/I_0 = V_0(1 - I/I_0). \tag{6.1}$$

The distance along the direction of flow d_e (the deflection measurement position) can be expressed, considering fluid flow in the chamber, as:

$$d_e = v_{along} t = \frac{Q}{h_e w_e} t \tag{6.2}$$

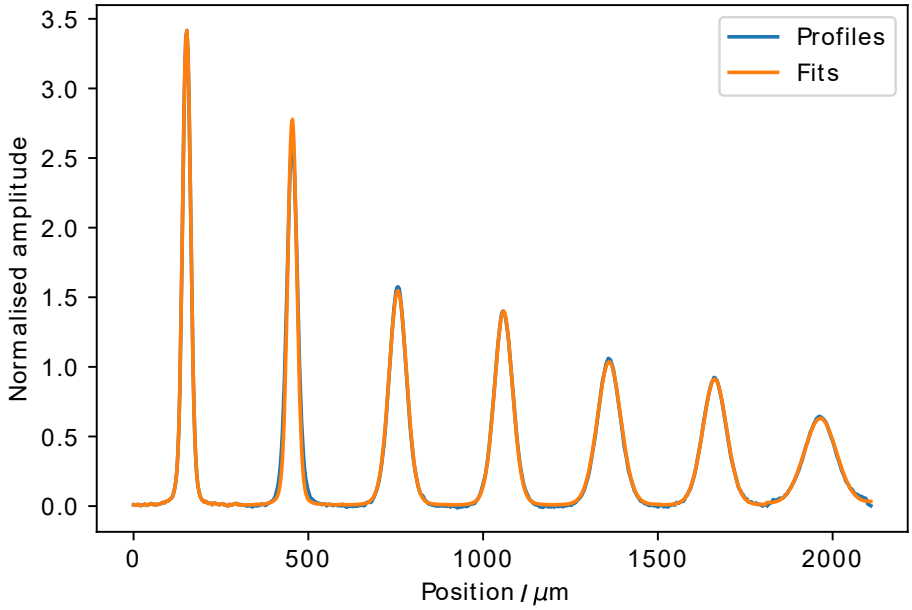

Fig. 6.5 An example of a numerical fit to an experimentally measured diffusion flow pattern. The least-squares error algorithm generates an estimate of the analyte hydrodynamic-radius.

where v_{along} is the molecule convection velocity along the chamber, w_e is the chamber width, h_e is the chamber height, t is the elution duration in the electrophoresis chamber and Q is the total flow rate. Finally, the electrophoretic-mobility can be expressed as:

$$\mu_e = \frac{v_e}{E} = \frac{x}{tE} = \frac{xw_eQ}{Vd_eh_ew_e} = \frac{Q}{Vd_eh_e}x = \frac{Q}{V_0(1-I/I_0)d_eh_e}x \tag{6.3}$$

where v_e is the transverse electrophoretic velocity, E is the electric field strength and x is the electrophoretic deflection. In this scenario, I measured the experimental parameters to be: $Q = 337$ µL/h, $V_0 = 60$ V, $d_e = 2880$ µm, $h_e = 55$ µm, $I = 0.267 \pm 0.002$ mA, $I_0 = 0.283 \pm 0.001$ mA. I estimated the mobility by applying $V_0 = 0$ V and $V_0 = 60$ V in alternating order. In this way, I could estimate the sample electrophoretic deflection, x, between the two consecutive images which gave an estimate of μ_e.

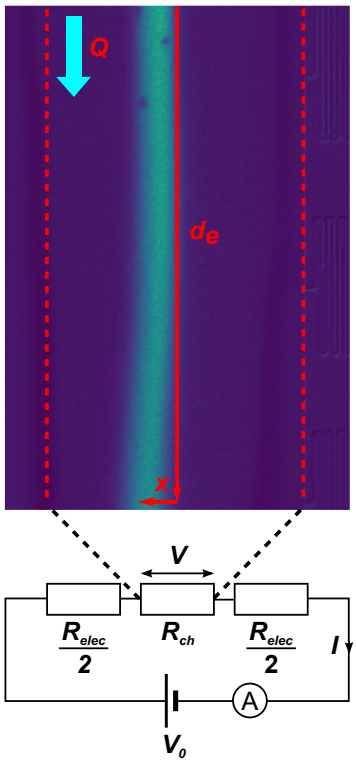

Fig. 6.6 The electrophoresis-device equivalent electronic circuit. During the calibration step, the chamber electric resistance can be neglected, allowing R_{elec} estimation. Due to a high electrode resistance of $R_{elec} \sim 250$ kΩ, I had only ~ 5 % voltage drop across the main electrophoresis chamber.

6.3.7 Size and charge calculations

The diffusion coefficient D quantifies the fluctuations of a particle under Brownian motion and is described by the Stokes-Einstein equation [298]:

$$D = \frac{k_B T}{6\pi\eta R_h} \tag{6.4}$$

where η is the viscosity of the solution, R_h is the hydrodynamic-radius and k_B and T are the Boltzmann constant and absolute temperature, respectively.

The measured diffusion constant D and the electrophoretic-mobility μ_e can be used to estimate the complex charge:

$$q = \frac{k_B T}{D}\mu_e \times \frac{1+\kappa R_h}{f_1(\kappa R_h)} \tag{6.5}$$

where κ is the inverse Debye length and f_1 is a function of R_h that describes the effect of the electric-field distribution around the particle [299]. For most of the proteins in high salt buffers, $f_1(\kappa R_h) \approx 1$ since $\kappa R_h \ll 1$. Hence, the expression for the protein charge can be simplified by the Nernst-Einstein relation [298]:

$$q = Ze = \frac{k_B T}{D}\mu_e = 6\pi\eta R_h \mu_e \tag{6.6}$$

6.3.8 Microfluidic chip fabrication

The devices were fabricated using a standard polydimethylsiloxane (PMDS) soft-lithography approach [86]. The master for the replica moulding of PDMS was fabricated with a single step SU-8 photolithography process as described in Section 2.2 [181]. After mixing PDMS (Sylgard184, Dow Corning, two components 10 : 1 ratio and degassed) and casting it onto the photo-lithographically defined structure, it was cured at 65°C for 1 h. A carbon black nanopowder (Sigma-Aldrich) was added to the PMDS before curing to create black devices, thus minimizing background noise and the unwanted autofluorescence from PDMS under 280 nm LED illumination during the measurements. The PDMS replica of each master was then cut, and the connection holes were made with a biopsy punch. The PDMS device was sonicated for 3 min in isopropanol, blown dry with N_2 gas, and placed in an oven at 65°C for 10 min. Finally, the replica was activated using an O_2 plasma at a 40 % power for 30 s (Diener etcher Femto, Germany) and bonded to a clean quartz slide (Alfa Aesar, $76.2 \times 25.4 \times 1.0$ mm).

6.3.9 Fluorescence-microscope setups

Two different fluorescence microscopes were used for the experiments: an intrinsic fluorescence microscope for a label-free protein detection and a green-label epifluorescence-measurement setup. First, the autofluorescence measurements of proteins containing the aromatic amino acid tryptophan were done on a quartz-based intrinsic fluorescence visualisation platform [104]. In short, the proteins were illuminated with a 25 mW 280 nm LED (M280L3, Thorlabs, UK) through an excitation filter (FF01-280/20-25, Semrock, USA) centered at $\lambda_{ex} = 280 \pm 10$ nm and a dichroic mirror (FF310-Di01-25x36, Semrock, USA). Then the fluorescence from the sample was collected through an emission filter (FF01-357/44-25, Semrock, USA) centered at $\lambda_{em} = 357 \pm 22$ nm and, finally, focused onto a EMCCD camera (Rolera EMC2, QImaging, Canada).

The green epifluorescence microscope (see Figure 6.7), optimised for the Green Fluorescent Protein (GFP) / Alexa-488 detection, consisted of a 490 nm LED (M490L4, Thorlabs, UK), an excitation filter at 482 ± 9 nm, a dichroic mirror ($350 - 488$ nm / $502 - 950$ nm) and the emission filter at 520 ± 14 nm (filter set MDF-GFP2, Thorlabs, UK). The microscope had a micrometer stage for accurate chip positioning in the field of view of a 2.5x objective, and the pictures were taken with a CCD camera (Retiga R1, QImaging, USA). A raw background-corrected fluorescence image of a sample under test is shown in Figure 6.1b.

6.3.10 Time matching

There was a slight delay between the molecule-absorption measurement after the LC separation and the detection on chip. The delay volume from the absorption-measurement cell to the flow adapter was 70 µL and the volume from the flow adapter to the chip detection channel was around 8 µL, causing $20 - 30$ min delay time, depending on the system flow. I matched the elution volume with the microscope-image sequence by comparing the absorption intensity on the absorbance detector (280 nm and 500 nm) and the fluorescence intensity of the eluting sample on chip.

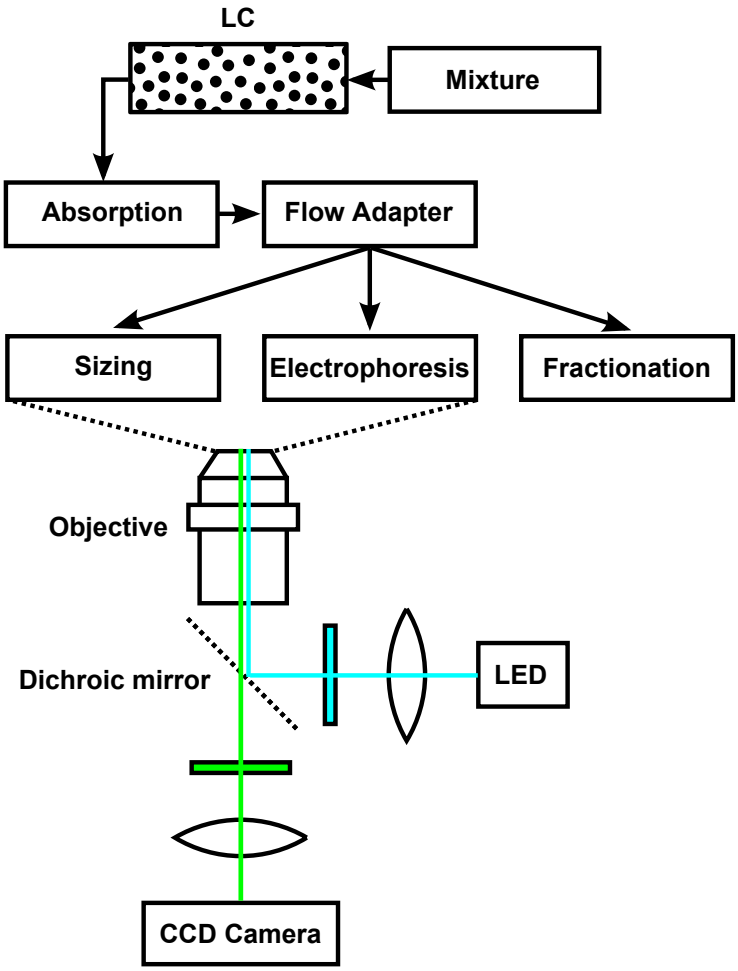

Fig. 6.7 Simplified schematic of the whole detection setup. A sample mixture is separated with an LC column. About 10% of the total flow is directed to the microfluidic-diffusional sizing and free-flow electrophoresis devices which are monitored continuously with a fluorescence microscope.

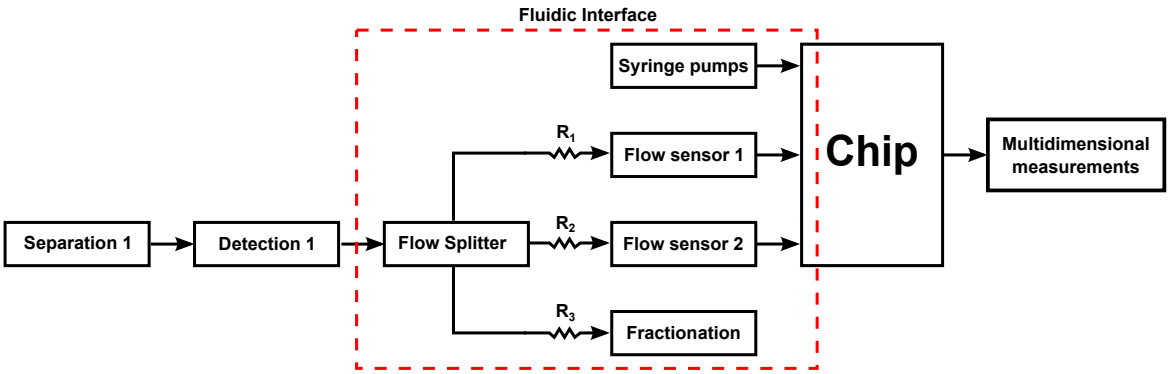

Fig. 6.8 The flow adapter interface contains a 4-way fluidic channel with calibrated PEEK capillaries acting as hydrodynamic resistors. The ratio of the capillary hydrodynamic resistance determines the fluidic adapter flow-splitting ratio, which can be monitored with flow sensors.

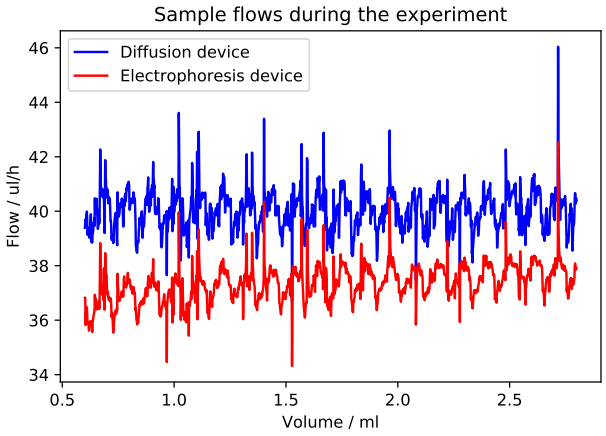

Fig. 6.9 The flow at the diffusional size and the electrophoresis devices is constant within a few percent variation.

6.4 Results and discussion

6.4.1 Flow control

The flow adapter interface, depicted in Figure 6.8, enabled a standard LC fractionation and simultaneous multidimentional eluting molecule characterisation. The LC separation on ÄKTA Pure was driven by two high-pressure pumps maintaining a relatively stable flow of 10 µL/min = 600 µL/h with a $1-5$ % fluctuation level, depending on the buffer and the age of separation column. The microfluidic flow adapter with carefully adjusted hydraulic resistances was distributing the incoming fluid from the LC absorption cell between two microfluidic sample inlets and a fractionation outlet. The flow rates at the chip ports 3 and 6 were measured to be 40.0 ± 0.7 µL/h and 37.4 ± 0.7 µL/h, respectively (diffusional sizing and the electrophoresis device sample inlets). The flow stability of the device inlets is shown in Figure 6.9. The rest of the post-LC separation fluid (about 90 %) was collected via the fractionation outlet.

6.4.2 Label-free protein characterisation

A mixture of three unlabelled proteins (thyroglobulin, conalbumin and lysozyme) was completely separated into three major peaks at volumes 1.06 mL, 1.52 mL and 2.12 mL, respectively, with a minor conalbumin oligomer peak at 1.34 mL, as shown in Figure 6.10a. I continuously monitored the hydrodynamic-radius R_h, electrophoretic-mobility μ_e and the effective charge q during the sample elution from the column. To estimate the biophysical properties of the separated molecular species more accurately, I determined their corresponding elution volume ranges, setting a 10 % maximum peak intensity threshold (see Figure 6.10a). Thyrolobulin, conalbumin and lysozyme sizes were measured to be 7.86 ± 0.30 nm, 3.96 ± 0.14 nm and 2.20 ± 0.14 nm with effective charges of -19.4 ± 1.3 e, -0.8 ± 0.3 e and 6.3 ± 0.4 e, respectively. The results are summarised in Figure 6.10c. The latter measurements agreed with already widely accepted biophysical values [117, 300, 301]. To represent the results more clearly, I then binned the data while weighting the importance of the points with respect to the absorption intensity at 280 nm, as shown in Figure 6.10b. Thus, I demonstrated a complete three-protein mixture separation and label-free characterisation, which could be represented by the distinct clusters in the 2-D molecular size versus effective charge map.

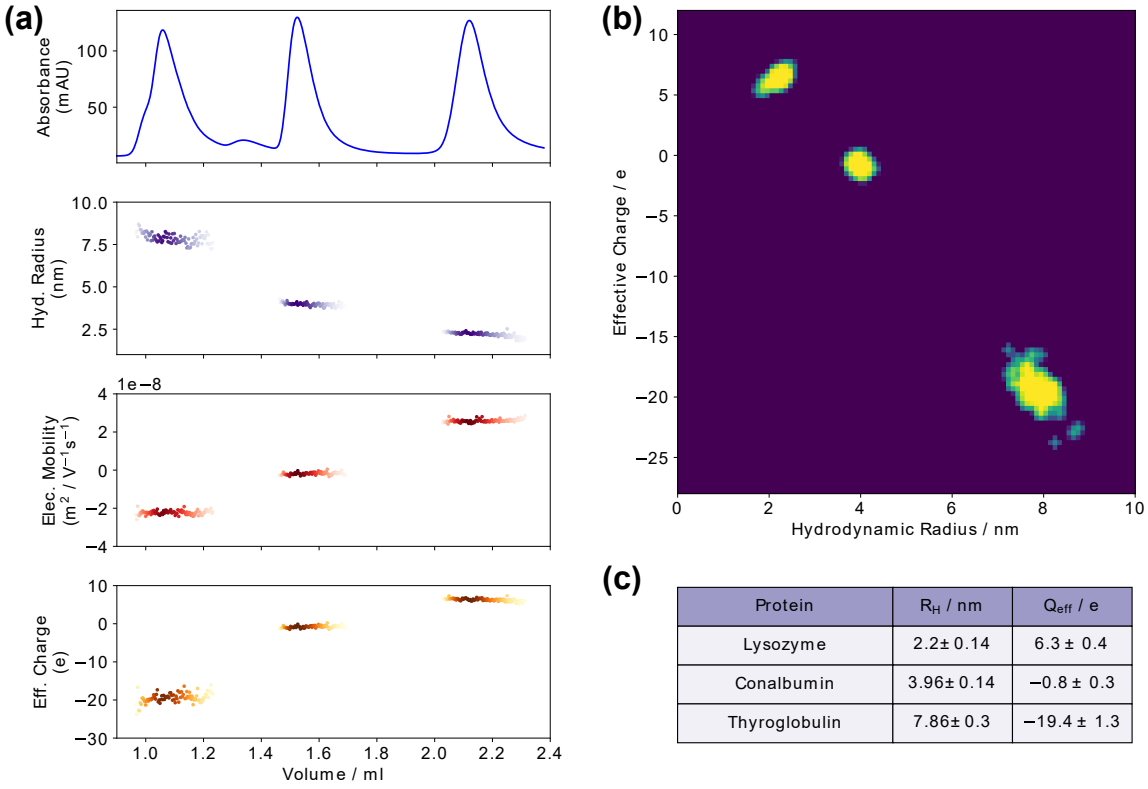

Protein	R_H / nm	Q_{eff} / e
Lysozyme	2.2± 0.14	6.3 ± 0.4
Conalbumin	3.96± 0.14	−0.8 ± 0.3
Thyroglobulin	7.86± 0.3	−19.4 ± 1.3

Fig. 6.10 Label-free thyroglobulin, conalbumin and lysozyme multidimensional biophysical characterisation. (a) The mixture is well separated into three major peaks and the eluting molecule size, electrophoretic-mobility and effective charge is measured continuously. (b) Then the individual measurements conducted every 20 s are weighted, based on the molecular absorption at 280 nm, and binned, revealing 3 major populations in the mixture, as expected. (c) Summary of the protein measured characteristics.

6.4.3 Labelled sample separation

The LC separation of the Atto-488 labelled streptavidin-biotin-based system resulted in multiple sample elution peaks, as shown in Figure 6.11a. Only the Atto-488 labelled molecules (complexes I-V) were detected by the green fluorescence microscope. The first major peak with the elution volume between 1 ml and 1.5 ml had three sub-peaks which could not be separated completely due to insufficient resolution at the given molecular weight range of our selected column. However, using a 2nd derivative analysis of the absorption at 500 nm, I estimated the approximate elution volumes for streptavidin with one, two and three BSA molecules to be 1.05 ml, 1.15 ml and 1.3 ml, respectively, as shown in Figure 6.11b. The second major peak with the elution volume between 1.6 ml and 1.9 ml could be identified to be streptavidin with four Atto-488 dye molecules and, finally, the last well-defined peak with the elution volume between 2 ml and 2.3 ml was the free biotinylated Atto-488 dye.

6.4.4 Heterogeneous-labelled analyte separation and characterisation

I then used the elution volume ranges to estimate the size and effective charge of the complexes with the corresponding confidence intervals (see the full data in Figure 6.12a). Furthermore, for better result visualisation, I plotted the effective charge versus the molecular size map, where the intensity of each point was binned and weighted with respect to the 500 nm absorption intensity, summarising the biophysical properties of the five Atto-488 labelled molecular complexes abundant in the mixture, as shown in Figure 6.12b.

The charge of a biotinylated Atto-488 dye was measured to be -0.99 ± 0.11 e which agreed with the expected charge of -e close to neutral pH conditions [302]. Streptavavidin with four bound dyes resulted in the size of 3.51 ± 0.13 nm and an effective charge of around -2.83 ± 0.28 e. BSA under normal pH conditions is known to have an effective charge of around -7e [117]. Therefore, the expected effective charge of the streptavidin-BSA complexes III-V (see Fig. 6.2b) is $-9e$, $-15e$ and $-21e$, respectively. The measured charges of the complexes III-V, -13.5 ± 0.9 e, -17.5 ± 1.3 e and -24.2 ± 1.3 e, respectively, agreed qualitatively with the predictions. The negative bias could be explained by the fact that the complexes were not separated completely and there was a small proportion of higher molecular mass species at the time of the measurement on chip. The properties of the eluting molecules are summarised in Figure 6.12c.

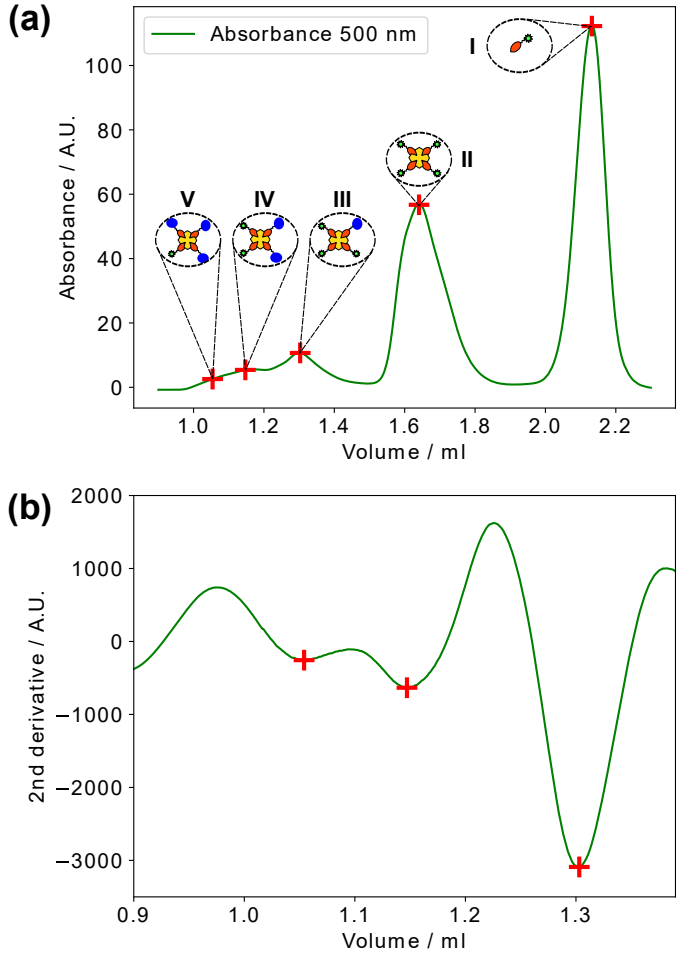

Fig. 6.11 Poorly separated species peak determination. (a) Streptavidin, BSA and Atto-488 dye-complex absorbance at 500 nm just after the LC separation. I can identify three distinct regions in the spectra representing the 5 different labelled molecular complexes. (b) 2nd derivative of the spectrum between 1-1.5ml reveals 3 most significant sub-peaks. To detect the minima from the 2nd derivative I applied a Savitzky-Golay filter two times with 251 points: the original spectrum and the second derivative of the spectrum.

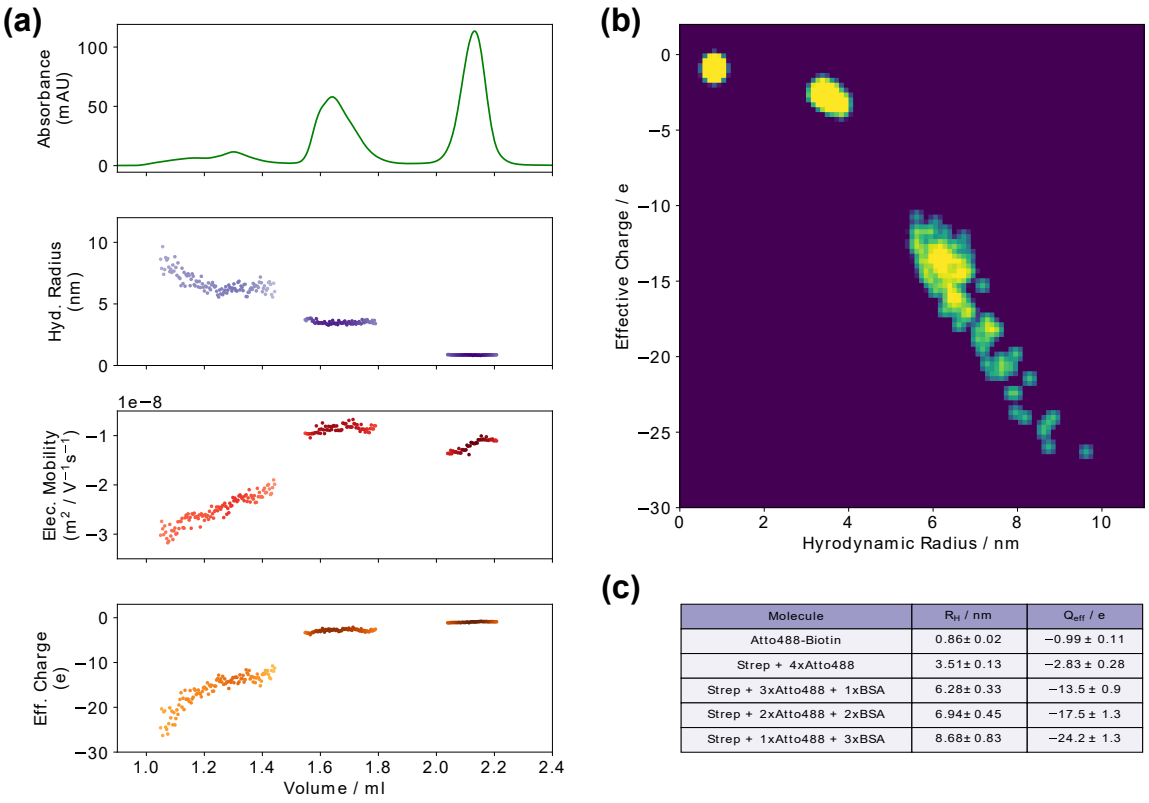

Molecule	R_H / nm	Q_{eff} / e
Atto488-Biotin	0.86± 0.02	−0.99 ± 0.11
Strep + 4xAtto488	3.51± 0.13	−2.83 ± 0.28
Strep + 3xAtto488 + 1xBSA	6.28± 0.33	−13.5 ± 0.9
Strep + 2xAtto488 + 2xBSA	6.94± 0.45	−17.5 ± 1.3
Strep + 1xAtto488 + 3xBSA	8.68± 0.83	−24.2 ± 1.3

Fig. 6.12 The labelled heterogeneous streptavidin-BSA-Atto488 mixture characterisation. (a) The separation yielded 3 major peaks, with the first peak containing 3 overlapping peaks. The five identified labelled molecule complexes are characterised and 2-dimensional charge versus size maps is constructed (b). The points are binned and weighted, based on the absorption intensity at 500 nm. (c) After identifying the molecular elution volume ranges, the molecule biophysical properties are estimated.

6.5 Conclusions

To summarise, I established a direct coupling between size-exclusion chromatography with a parallelised microfluidic analysis, while being able to fractionate about 90 % of the total sample volume. The multidimensional characterisation of distinct complexes yielded their simultaneous size, electrophoretic-mobility and effective charge measurements. First, I demonstrated the operational principle of the approach by determining the biophysical properties of unlabelled standard proteins within a mixture. Then, I showed the potential of this analytical method with a heterogeneous labelled molecule mixture by analysing multiple partially separated peaks after chromatographic separation and predicting the effective charge and molecular size of complexes within the mixture.

This measurement strategy is expandable beyond the two microfluidic methods chosen here. Further analytical and separative techniques such as capillary electrophoresis or isoelectric focusing could be employed to investigate more complex forms of protein oligomerisation and protein-protein interactions. This unique protein analysis approach has a big potential to extend the characterisation of heterogeneous protein mixtures in the condensed phase and demonstrates a possible direction for building a scalable mass-spectrometry-equivalent device on a chip.

Chapter 7

Conclusions and future directions

7.1 Overall conclusions

The work described in this thesis demonstrates how soft-lithography-enabled microfluidic devices can enhance the state-of-the-art biomolecular detection and characterisation.

To begin with, I developed a microfluidic aerosol spray device for generating micron-sized drops. I explored the spray-generation conditions and identified that the nozzle architecture causes a supersonic gas flow, thus enabling reproducible liquid atomisation. Then, I investigated the drop-drying mechanisms in-flight and upon landing on a surface. As a result, I have been able to estimate that the drops evaporate in milliseconds, thus allowing for a continuous surface spray drying which avoids liquid build up on the surface. Finally, this unique control over the drop-drying times was used to an advantage when depositing heterogeneous protein mixtures on mica, allowing for their characterisation with atomic force probe microscopy.

The controlled surface spray-drying ability - a method to interface liquid processing and dry-phase surface measurements - led me to exploring whether this strategy could be used for biomolecular deposition on mechanical sensors for gravimetric analysis. Generally, not liquid but gaseous, or ideally a vacuum, environment is preferred for such sensors due to the high viscous damping in liquids. To realise this idea, I built a MEMS cantilever resonant-frequency monitoring platform and used the spray to deliver inorganic salts and proteins on the cantilever surface. Indeed, I observed the analyte build-up on the sensor causing the resonant-frequency changes. By monitoring these changes, I was able to show that this method is quantitative and sensitive to the analyte concentration. Finally, I used a

calibration solution to determine the mass concentration of an unknown protein solution. All of this was achieved in a label-free manner; thus the method could be used with any analytes, biomarkers and organic molecules which could not be detected otherwise.

However, dry-mass sensing from analyte solution was neither selective nor could detect proteins in the presence of buffer salts. Biomolecules, in general, are stable in buffers with a specific acidity or ionic strength. Buffer salt mass concentrations typically reach milligrams per millilitre; however, this is orders of magnitude larger than typical biomolecule in solution concentrations. To mitigate these challenges, I started exploring protein separation and desalting techniques. I chose liquid chromatography - one of the most widespread protein-purification techniques used in academia and industry. To this effect, I established a fluidic interface between the two systems and, therefore was able to perform online liquid aerosol spray from a size-exclusion column. Then, I incorporated an extra desalting step using a protein-desalting column. Finally, I combined all of the latter steps and demonstrated a standard protein purification from a mixture with a subsequent desalting and spray drying onto a mechanical sensor. This time, I have chosen a quartz-crystal microbalance for the gravimetric analysis simply because of its ease of use and a larger detection area. I was able to show that the method is quantitative and concentration sensitive, again in a label-free manner.

The ability to interface microfluidic analytics with an established protein-separation technique, has made me think more broadly. Could we not use this strategy to perform other kind of analyses on the protein mixtures? What about doing a *multidimensional* simultaneous analysis on a lab-on-chip system? I set an aim to develop a mass-spectrometry analogue on a chip for in-solution molecular characterisation yielding biophysical properties, such as size and charge. I extended the fluidic flow adapter interface for splitting the flow into multiple simultaneously-operating microfluidic devices. Then, I combined molecular size [101] and electrophoretic-mobility [117] measurement devices on the same chip and connected them online with a size-exclusion column. First, to validate this approach, I used a standard protein mixture and detected proteins on chip using their intrinsic fluorescence in the ultraviolet light [104]. Then, I demonstrated the ability to apply the same approach for a labelled heterogeneous protein mixture characterisation in a single experimental procedure.

The microfluidic methods, described in this thesis, are at a proof-of-concept stage. I envisage a broad range of applications, especially for the bulk flow protein separation combined with microfluidic analysis and the microfluidic surface spray deposition for atomic force microscopy. A variety of biological systems could be investigated. One such example could be studying protein systems prone to aggregate. Specifically, these methods could give

insights into the toxic oligomer formation, their charge and size distributions, at the early stages of aggregation. Also, protein post-translational modifications, such as phosphorylation and ubiquitination, are interesting phenomena to investigate the mechanisms, which cells use to protect themselves or to change the function of proteins.

7.2 Further directions

7.2.1 Microfluidic spray

The microfluidic spray device could include more functions, such as separation and desalting. Separation, such as free-flow or capillary electrophoresis, would enable selective protein surface deposition and could be used to advantage for a number of approaches. Protein desalting on chip would make an even bigger impact, allowing for biomolecule surface deposition as a preparation step for various surface-based spectroscopy techniques.

7.2.2 Gravimetric sensing

More effort could be dedicated to identifying an acoustic sensor with the largest sensitivity per unit area. Some possible examples are surface-acoustic-wave devices or ultra-high frequency QCMs. Integration of more functions on the spray chip, such as desalting and separation, could enable label-free selective-protein diagnostics, potentially sensitive to single molecules. Moreover, the detection sensitivity could be improved further by performing the frequency measurement under vacuum conditions,thus reducing the viscous damping. Finally, the molecular sensitivity could be enhanced even further if a high molecular weight label would be used.

7.2.3 Multidimensional protein characterisation

The experiments, described in this thesis, present a proof-of-principle method of what this approach could achieve. More functions could be added, such as iso-electric point measurement, by performing the electrophoretic-mobility analysis at different pH conditions. Moreover, the first separation step could be improved or even exchanged with say, capillary electrophoresis, potentially allowing all of the platform to be on the same chip. This would be a truly novel stand-alone mass spectrometry on chip analysis in the condensed phase.

More work could also be dedicated to labelling the proteins with different dyes fluorescing at different wavelengths, thus allowing for simultaneous multiple target characterisation in one step. Finally, this method also would benefit from a real-time software showing the molecular properties of the eluting molecules as they are eluting through the detectors, helping the user to make a decision on the purified fraction selection and fractionation.

Appendix A

Microfluidic device fabrication steps

The microfluidic device fabrication steps, as discussed in Chapter 2, are depicted in Figure A.1. The acetate mask with the device designs is placed on top of a Si wafer with spin-coated photoresist. After the UV exposure, the photoresist is developed with PGMEA and rinsed with isopropyl alcohol. The silicon wafer with the fabricated micron-sized features is used as a mould for imprinting the features into PDMS. After degassing, curing and cutting, the device ports are punched. The device is cleaned from the PDMS debris with sonication in isopropyl alcohol, followed by plasma bonding it to a glass slide. Finally, the device is interfaced with tubing and metal ports, depending on the function and application of the device.

Fig. A.1 Microfluidic-device fabrication steps.

Appendix B

Troubleshooting guide for microfluidics

In this section, I aim to give guidance for troubleshooting microfluidic experiments.

Problem: Bubbles are trapped in the channels or they appear during the experiment.

Suggestion: To minimise the possibility of trapping bubbles, design devices which do not have sharp corners. You can get best results if you use a freshly bonded chip as it will be more hydrophilic. Also, degassing the solution before use can prevent bubble formation during long experimental procedures. Finally, an effective way to get rid of bubbles is to press on the device for $\sim$ 1 min until the bubble disappears (PDMS is permeable to gas).

Problem: The device does not bond.

Suggestion: Make sure that the chip and the glass/quartz surfaces are clean. Bonding PDMS to quartz or PDMS to PDMS can be improved/speeded up by heating the bonded chips on a hotplate for several minutes.

Problem: Proteins stick to the channels.

Suggestion: You can make the channel surface slightly more hydrophilic by doing a 500 s long plasma treatment at 80 % power. Also, if possible, consider adding Tween to the protein solution.

Problem: Image background noise is too large.

Suggestion: Add a little bit of black carbon nanopower when mixing the PDMS.

Problem: The microfluidic device leaks.

Suggestion: There are various possible causes for this problem. First of all, use a new puncher and check whether it makes cracks around the device inlet ports. If yes, that means that the PDMS slab is too brittle; reduce the baking time and ensure the 10:1 mixing ratio. Secondly, the pressure on the device can be too high, either due to the large hydraulic resistance or too high a flow. You may want to estimate what the pressure is at the flow rate, at which the device is operating. One way to prevent leaking at higher pressures is to use metal Fisnar FIS5601169 connectors.

Problem: Flow is not stable on chip.

Suggestion: If the pressure on chip is high, syringe pumps may start oscillating. A good alternative is to use a pressure-driven flow. However, a way around it is to operate the device in a withdrawing mode using only one pump, while the solution is drawn from multiple inlets filled with gel loading tips. However, the problem may also lie at the device outlets, especially when there is more than one outlet. Make sure that the resistances at the device outlets are large or that the fluid is escaping the device at a constant height. Hydrostatic pressure, due to the liquid column at the device outlets, can cause a surprisingly large effect.

Problem: I have very little sample, how to fill a 1 ml syringe?

Suggestion: Design the device for the use in withdrawing mode or fill the syringe first with a liquid which does not mix with your solution (e.g. oil), and then load only a small amount of your protein solution in the tubing.

Problem: The SU-8 device height varies a lot along the Si wafer.

Suggestion: $5-10$ % error is acceptable; however, the photoresist spin-coating tends to cause artefacts at the wafer edges. Aim to design masks, leaving at least 1 cm from the edge of the wafer.

Appendix C

Diffusion profile simulations

First, I determine steady Poiseuille flow in a rectangular cross-section channel. The Navier-Stokes equation for incompressible flow:

$$\rho\left[\partial_t \mathbf{v} + (\mathbf{v}\cdot\nabla)\mathbf{v}\right] = -\nabla p + \eta\nabla^2\mathbf{v} + \rho\mathbf{g} \tag{C.1}$$

can be simplified considering time independence ($\partial_t\mathbf{v}$=0) and translational invariance (($\mathbf{v}\cdot\nabla)\mathbf{v} = \mathbf{0}$):

$$\eta\left[\partial_y^2 + \partial_z^2\right] v_x(y,z) = \partial_x p(x) \tag{C.2}$$

The analytical solution can be expressed as a quickly converging series:

$$v_x(y,z)\alpha \sum_{n\,odd}\sum_{m\,odd} \frac{1}{nm\left(\frac{n^2}{a^2}+\frac{m^2}{b^2}\right)} \sin\left(\frac{n\pi}{a}y\right)\sin\left(\frac{m\pi}{b}z\right) \tag{C.3}$$

where v_x is the Poiseuille flow; a and b are the channel dimensions in the y and z directions respectively.

Secondly, I consider the general convection-diffusion equation for the concentration $c(x,y,z)$ and diffusion coefficient D:

$$\frac{\partial c}{\partial t} = \nabla\cdot(D\nabla c) - \nabla\cdot(c\mathbf{v}) \tag{C.4}$$

By applying time invariance and neglecting diffusion in the x direction:

$$\partial_x c = \frac{D}{v_x}\left(\partial_y^2 + \partial_z^2\right) c \tag{C.5}$$

I integrate this equation numerically applying Neumann boundary conditions with a space step δx chosen with the Courant-Friedrichs-Lewy condition:

$$\delta x = \frac{1}{2D} min(\delta y, \delta z)^2 min(v_x) \tag{C.6}$$

The choice of δx is chosen so that the step matrix S is independent of D and Q, the flow rate. I then define the dimensionless step size $\delta x' = \delta x \cdot D/Q$; the number of steps to reach a distance L is:

$$N_{steps} = \frac{LD}{\delta x' Q} \tag{C.7}$$

The evolution of an initial detected concentration distribution c_0 is quickly calculated by repeated matrix squaring. Using $S_i = S^{2^i}$, the total number of matrix multiplications necessary is only $\approx log_2(N_{steps})$.

References

[1] Lynn Margulis and Dorion Sagan. *What is life?* Univ of California Press, 2000.

[2] Christian B Anfinsen, Edgar Haber, Michael Sela, and FH White. The kinetics of formation of native ribonuclease during oxidation of the reduced polypeptide chain. *Proceedings of the National Academy of Sciences*, 47(9):1309–1314, 1961.

[3] Christian B Anfinsen. Principles that govern the folding of protein chains. *Science*, 181(4096):223–230, 1973.

[4] Cyrus Levinthal. Are there pathways for protein folding? *Journal de Chimie Physique*, 65:44–45, 1968.

[5] Ehud Gazit. The "correctly folded" state of proteins: is it a metastable state? *Angewandte Chemie International Edition*, 41(2):257–259, 2002.

[6] Charles L Brooks, Martin Gruebele, José Nelson Onuchic, and Peter G Wolynes. Chemical physics of protein folding. *Proceedings of the National Academy of Sciences*, 95(19):11037–11038, 1998.

[7] John A Hardy and Gerald A Higgins. Alzheimer's disease: the amyloid cascade hypothesis. *Science*, 256(5054):184, 1992.

[8] John Hardy and Dennis J Selkoe. The amyloid hypothesis of Alzheimer's disease: progress and problems on the road to therapeutics. *Science*, 297(5580):353–356, 2002.

[9] Claudio Soto. Unfolding the role of protein misfolding in neurodegenerative diseases. *Nature Reviews Neuroscience*, 4(1):49, 2003.

[10] National Diabetes Data Group et al. Classification and diagnosis of diabetes mellitus and other categories of glucose intolerance. *Diabetes*, 28(12):1039–1057, 1979.

[11] Saniye Yumlu, Robert Barany, Magdalena Eriksson, and Christoph Röcken. Localized insulin-derived amyloidosis in patients with diabetes mellitus: a case report. *Human Pathology*, 40(11):1655–1660, 2009.

[12] John C Kendrew, G Bodo, Howard M Dintzis, RG Parrish, Harold Wyckoff, and David C Phillips. A three-dimensional model of the myoglobin molecule obtained by x-ray analysis. *Nature*, 181(4610):662–666, 1958.

[13] Helen M Berman, John Westbrook, Zukang Feng, Gary Gilliland, Talapady N Bhat, Helge Weissig, Ilya N Shindyalov, and Philip E Bourne. The protein data bank. *Nucleic Acids Research*, 28(1):235–242, 2000.

[14] José L Jiménez, Ewan J Nettleton, Mario Bouchard, Carol V Robinson, Christopher M Dobson, and Helen R Saibil. The protofilament structure of insulin amyloid fibrils. *Proceedings of the National Academy of Sciences*, 99(14):9196–9201, 2002.

[15] Adam Ben-Shem, Nicolas Garreau de Loubresse, Sergey Melnikov, Lasse Jenner, Gulnara Yusupova, and Marat Yusupov. The structure of the eukaryotic ribosome at 3.0 angstrom resolution. *Science*, 334(6062):1524–1529, 2011.

[16] Anthony WP Fitzpatrick, Galia T Debelouchina, Marvin J Bayro, Daniel K Clare, Marc A Caporini, Vikram S Bajaj, Christopher P Jaroniec, Luchun Wang, Vladimir Ladizhansky, Shirley A Müller, et al. Atomic structure and hierarchical assembly of a cross-β amyloid fibril. *Proceedings of the National Academy of Sciences*, 110(14):5468–5473, 2013.

[17] Sebastian Geibel, Erik Procko, Scott J Hultgren, David Baker, and Gabriel Waksman. Structural and energetic basis of folded-protein transport by the fimd usher. *Nature*, 496(7444):243, 2013.

[18] Heena Khatter, Alexander G Myasnikov, S Kundhavai Natchiar, and Bruno P Klaholz. Structure of the human 80s ribosome. *Nature*, 520(7549):640, 2015.

[19] David S Wishart, Brian D Sykes, and Fredric M Richards. The chemical shift index: a fast and simple method for the assignment of protein secondary structure through nmr spectroscopy. *Biochemistry*, 31(6):1647–1651, 1992.

[20] Kresten Lindorff-Larsen, Robert B Best, Mark A DePristo, Christopher M Dobson, and Michele Vendruscolo. Simultaneous determination of protein structure and dynamics. *Nature*, 433(7022):128, 2005.

[21] Carlos W Bertoncini, Rodolfo M Rasia, Gonzalo R Lamberto, Andres Binolfi, Markus Zweckstetter, Christian Griesinger, and Claudio O Fernandez. Structural characterization of the intrinsically unfolded protein β-synuclein, a natural negative regulator of α-synuclein aggregation. *Journal of Molecular Biology*, 372(3):708–722, 2007.

[22] Sandor Kasas and Giovanni Dietler. Probing nanomechanical properties from biomolecules to living cells. *Pflügers Archiv-European Journal of Physiology*, 456(1):13–27, 2008.

[23] Lilia A Chtcheglova, George T Shubeita, Sergey K Sekatskii, and Giovanni Dietler. Force spectroscopy with a small dithering of afm tip: a method of direct and continuous measurement of the spring constant of single molecules and molecular complexes. *Biophysical Journal*, 86(2):1177–1184, 2004.

[24] Jozef Adamcik, Jin-Mi Jung, Jérôme Flakowski, Paolo De Los Rios, Giovanni Dietler, and Raffaele Mezzenga. Understanding amyloid aggregation by statistical analysis of atomic force microscopy images. *Nature Nanotechnology*, 5(6):423, 2010.

[25] Jeffrey F Smith, Tuomas PJ Knowles, Christopher M Dobson, Cait E MacPhee, and Mark E Welland. Characterization of the nanoscale properties of individual amyloid fibrils. *Proceedings of the National Academy of Sciences*, 103(43):15806–15811, 2006.

[26] Tuomas P Knowles, Anthony W Fitzpatrick, Sarah Meehan, Helen R Mott, Michele Vendruscolo, Christopher M Dobson, and Mark E Welland. Role of intermolecular forces in defining material properties of protein nanofibrils. *Science*, 318(5858):1900–1903, 2007.

[27] Norma J Greenfield. Using circular dichroism spectra to estimate protein secondary structure. *Nature Protocols*, 1(6):2876, 2006.

[28] Norma J Greenfield and Gerald D Fasman. Computed circular dichroism spectra for the evaluation of protein conformation. *Biochemistry*, 8(10):4108–4116, 1969.

[29] Stephen W Provencher and Juergen Gloeckner. Estimation of globular protein secondary structure from circular dichroism. *Biochemistry*, 20(1):33–37, 1981.

[30] D Michael Byler and Heino Susi. Examination of the secondary structure of proteins by deconvolved ftir spectra. *Biopolymers: Original Research on Biomolecules*, 25(3):469–487, 1986.

[31] Parvez I Haris and Feride Severcan. Ftir spectroscopic characterization of protein structure in aqueous and non-aqueous media. *Journal of Molecular Catalysis B: Enzymatic*, 7(1-4):207–221, 1999.

[32] Priyabrata Pattnaik. Surface plasmon resonance. *Applied Biochemistry and Biotechnology*, 126(2):79–92, 2005.

[33] Eleftherios P Diamandis. Mass spectrometry as a diagnostic and a cancer biomarker discovery tool opportunities and potential limitations. *Molecular & Cellular Proteomics*, 3(4):367–378, 2004.

[34] Ruedi Aebersold and Matthias Mann. Mass spectrometry-based proteomics. *Nature*, 422(6928):198, 2003.

[35] Shao-En Ong and Matthias Mann. Mass spectrometry–based proteomics turns quantitative. *Nature Chemical Biology*, 1(5):252, 2005.

[36] Ole Nørregaard Jensen. Modification-specific proteomics: characterization of post-translational modifications by mass spectrometry. *Current Opinion in Chemical Biology*, 8(1):33–41, 2004.

[37] Eric S Witze, William M Old, Katheryn A Resing, and Natalie G Ahn. Mapping protein post-translational modifications with mass spectrometry. *Nature Methods*, 4(10):798, 2007.

[38] William J Baumol. *The cost disease: Why computers get cheaper and health care doesn't*. Yale University Press, 2012.

[39] Muin J Khoury, Michael F Iademarco, and William T Riley. Precision public health for the era of precision medicine. *American Journal of Preventive Medicine*, 50(3):398, 2016.

[40] Wentao Su, Xinghua Gao, Lei Jiang, and Jianhua Qin. Microfluidic platform towards point-of-care diagnostics in infectious diseases. *Journal of Chromatography A*, 1377:13–26, 2015.

[41] Allon M Klein, Linas Mazutis, Ilke Akartuna, Naren Tallapragada, Adrian Veres, Victor Li, Leonid Peshkin, David A Weitz, and Marc W Kirschner. Droplet barcoding for single-cell transcriptomics applied to embryonic stem cells. *Cell*, 161(5):1187–1201, 2015.

[42] Shikha Sharma, Julia Zapatero-Rodríguez, Pedro Estrela, and Richard O'Kennedy. Point-of-care diagnostics in low resource settings: present status and future role of microfluidics. *Biosensors*, 5(3):577–601, 2015.

[43] Brandon Berg, Bingen Cortazar, Derek Tseng, Haydar Ozkan, Steve Feng, Qingshan Wei, Raymond Yan-Lok Chan, Jordi Burbano, Qamar Farooqui, Michael Lewinski, et al. Cellphone-based hand-held microplate reader for point-of-care testing of enzyme-linked immunosorbent assays. *ACS Nano*, 9(8):7857–7866, 2015.

[44] Christoph Laske, Hamid R Sohrabi, Shaun M Frost, Karmele López-de Ipiña, Peter Garrard, Massimo Buscema, Justin Dauwels, Surjo R Soekadar, Stephan Mueller, Christoph Linnemann, et al. Innovative diagnostic tools for early detection of Alzheimer's disease. *Alzheimer's & Dementia*, 11(5):561–578, 2015.

[45] Brunero Cappella and Giovanni Dietler. Force-distance curves by atomic force microscopy. *Surface Science Reports*, 34(1-3):1–104, 1999.

[46] G Longo, L Alonso-Sarduy, L Marques Rio, A Bizzini, A Trampuz, J Notz, G Dietler, and S Kasas. Rapid detection of bacterial resistance to antibiotics using afm cantilevers as nanomechanical sensors. *Nature Nanotechnology*, 8(7):522, 2013.

[47] Sandor Kasas, Francesco Simone Ruggeri, Carine Benadiba, Caroline Maillard, Petar Stupar, Hélène Tournu, Giovanni Dietler, and Giovanni Longo. Detecting nanoscale vibrations as signature of life. *Proceedings of the National Academy of Sciences*, 112(2):378–381, 2015.

[48] Kidong Park, Larry J Millet, Namjung Kim, Huan Li, Xiaozhong Jin, Gabriel Popescu, NR Aluru, K Jimmy Hsia, and Rashid Bashir. Measurement of adherent cell mass and growth. *Proceedings of the National Academy of Sciences*, 107(48):20691–20696, 2010.

[49] Subra Suresh. Biomechanics and biophysics of cancer cells. *Acta Materialia*, 55(12):3989–4014, 2007.

[50] Charles S Smith. Piezoresistance effect in germanium and silicon. *Physical Review*, 94(1):42, 1954.

[51] William Paul and GL Pearson. Pressure dependence of the resistivity of silicon. *Physical Review*, 98(6):1755, 1955.

[52] Rudolf H Krondorfer and Yeong K Kim. Packaging effect on mems pressure sensor performance. *IEEE Transactions on Components and Packaging Technologies*, 30(2):285–293, 2007.

[53] Parag Thakre, Atanu Phukan, Nikhil Chandra, and Sriharsha Aradhya. Mems flow sensor, March 4 2008. US Patent 7,337,678.

[54] Kenneth E Wojciechowski, Bernhard E Boser, and Albert P Pisano. A mems resonant strain sensor operated in air. In *Micro Electro Mechanical Systems, 2004. 17th IEEE International Conference on.(MEMS)*, pages 841–845. IEEE, 2004.

[55] AS Sezen, S Sivaramakrishnan, S Hur, R Rajamani, W Robbins, and Bradley J Nelson. Passive wireless mems microphones for biomedical applications. *Journal of Biomechanical Engineering*, 127(6):1030–1034, 2005.

[56] Fangrong Hu, Jun Yao, Chuankai Qiu, and Hao Ren. A mems micromirror driven by electrostatic force. *Journal of Electrostatics*, 68(3):237–242, 2010.

[57] Jean-Christophe Eloy and Eric Mounier. Status of the mems industry. In *MEMS/MOEMS Components and Their Applications II*, volume 5717, pages 43–50. International Society for Optics and Photonics, 2005.

[58] Yole Développement SA. Biomems & non-invasive sensors: Microsystems for life sciences & healthcare 2018. *www.i-micronews.com/report/product/biomems-non-invasive-sensors-microsystems-for-life-sciences-healthcare-2018.html*, 2018.

[59] Thomas Braun, Murali Krishna Ghatkesar, Natalija Backmann, Wilfried Grange, Pascale Boulanger, Lucienne Letellier, Hans-Peter Lang, Alex Bietsch, Christoph Gerber, and Martin Hegner. Quantitative time-resolved measurement of membrane protein–ligand interactions using microcantilever array sensors. *Nature Nanotechnology*, 4(3):179, 2009.

[60] JL Arlett, EB Myers, and ML Roukes. Comparative advantages of mechanical biosensors. *Nature Nanotechnology*, 6(4):203, 2011.

[61] Ming Su, Shuyou Li, and Vinayak P Dravid. Microcantilever resonance-based DNA detection with nanoparticle probes. *Applied Physics Letters*, 82(20):3562–3564, 2003.

[62] Namsoo Kim, Dong-Kyung Kim, and Yong-Jin Cho. Development of indirect-competitive quartz crystal microbalance immunosensor for c-reactive protein. *Sensors and Actuators B: Chemical*, 143(1):444–448, 2009.

[63] Gengfeng Zheng, Xuan PA Gao, and Charles M Lieber. Frequency domain detection of biomolecules using silicon nanowire biosensors. *Nano Letters*, 10(8):3179–3183, 2010.

[64] Frank Vollmer and Stephen Arnold. Whispering-gallery-mode biosensing: label-free detection down to single molecules. *Nature Methods*, 5(7):591, 2008.

[65] Alexandre G Brolo. Plasmonics for future biosensors. *Nature Photonics*, 6(11):709, 2012.

[66] Jeffrey N Anker, W Paige Hall, Olga Lyandres, Nilam C Shah, Jing Zhao, and Richard P Van Duyne. Biosensing with plasmonic nanosensors. In *Nanoscience And Technology: A Collection of Reviews from Nature Journals*, pages 308–319. World Scientific, 2010.

[67] Tao Ding, Ventsislav K Valev, Andrew R Salmon, Chris J Forman, Stoyan K Smoukov, Oren A Scherman, Daan Frenkel, and Jeremy J Baumberg. Light-induced actuating nanotransducers. *Proceedings of the National Academy of Sciences*, 113(20):5503–5507, 2016.

[68] Sunjie Ye, Gemma Marston, James R McLaughlan, Daniel O Sigle, Nicola Ingram, Steven Freear, Jeremy J Baumberg, Richard J Bushby, Alexander F Markham, Kevin Critchley, et al. Engineering gold nanotubes with controlled length and near-infrared absorption for theranostic applications. *Advanced Functional Materials*, 25(14):2117–2127, 2015.

[69] Gang L Liu, Joseph C Doll, and Luke P Lee. High-speed multispectral imaging of nanoplasmonic array. *Optics Express*, 13(21):8520–8525, 2005.

[70] Antoine Lesuffleur, Hyungsoon Im, Nathan C Lindquist, and Sang-Hyun Oh. Periodic nanohole arrays with shape-enhanced plasmon resonance as real-time biosensors. *Applied Physics Letters*, 90(24):243110, 2007.

[71] Daniel O Sigle, Setu Kasera, Lars O Herrmann, Aniello Palma, Bart de Nijs, Felix Benz, Sumeet Mahajan, Jeremy J Baumberg, and Oren A Scherman. Observing single molecules complexing with cucurbit [7] uril through nanogap surface-enhanced raman spectroscopy. *The Journal of Physical Chemistry Letters*, 7(4):704–710, 2016.

[72] Shuwen Zeng, Kandammathe Valiyaveedu Sreekanth, Jingzhi Shang, Ting Yu, Chih-Kuang Chen, Feng Yin, Dominique Baillargeat, Philippe Coquet, Ho-Pui Ho, Andrei V Kabashin, et al. Graphene–gold metasurface architectures for ultrasensitive plasmonic biosensing. *Advanced Materials*, 27(40):6163–6169, 2015.

[73] Ralf Lucklum and Peter Hauptmann. Acoustic microsensors—the challenge behind microgravimetry. *Analytical and Bioanalytical Chemistry*, 384(3):667–682, 2006.

[74] Isabelle Dufour, Etienne Lemaire, Benjamin Caillard, Hélène Debéda, Claude Lucat, Stephen M Heinrich, Fabien Josse, and Oliver Brand. Effect of hydrodynamic force on microcantilever vibrations: Applications to liquid-phase chemical sensing. *Sensors and Actuators B: Chemical*, 192:664–672, 2014.

[75] Todd M Squires and Stephen R Quake. Microfluidics: Fluid physics at the nanoliter scale. *Reviews of Modern Physics*, 77(3):977, 2005.

[76] Patrick Tabeling. *Introduction to microfluidics*. Oxford University Press on Demand, 2005.

[77] George M Whitesides. The origins and the future of microfluidics. *Nature*, 442(7101):368, 2006.

[78] Patrick Tabeling. Recent progress in the physics of microfluidics and related biotechnological applications. *Current Opinion in Biotechnology*, 25:129–134, 2014.

[79] Andreas Manz, D Jed Harrison, Elisabeth MJ Verpoorte, James C Fettinger, Aran Paulus, Hans Lüdi, and H Michael Widmer. Planar chips technology for miniaturization and integration of separation techniques into monitoring systems: capillary electrophoresis on a chip. *Journal of Chromatography A*, 593(1-2):253–258, 1992.

[80] Eric K Sackmann, Anna L Fulton, and David J Beebe. The present and future role of microfluidics in biomedical research. *Nature*, 507(7491):181, 2014.

[81] HTG Van Lintel, FCM Van de Pol, and S Bouwstra. A piezoelectric micropump based on micromachining of silicon. *Sensors and Actuators*, 15(2):153–167, 1988.

[82] D Jed Harrison, Andreas Manz, Zhonghui Fan, Hans Luedi, and H Michael Widmer. Capillary electrophoresis and sample injection systems integrated on a planar glass chip. *Analytical Chemistry*, 64(17):1926–1932, 1992.

[83] Carlo S Effenhauser, Gerard JM Bruin, Aran Paulus, and Markus Ehrat. Integrated capillary electrophoresis on flexible silicone microdevices: analysis of DNA restriction fragments and detection of single DNA molecules on microchips. *Analytical Chemistry*, 69(17):3451–3457, 1997.

[84] David C Duffy, J Cooper McDonald, Olivier JA Schueller, and George M Whitesides. Rapid prototyping of microfluidic systems in poly (dimethylsiloxane). *Analytical Chemistry*, 70(23):4974–4984, 1998.

[85] Ravi S Kane, Shuichi Takayama, Emanuele Ostuni, Donald E Ingber, and George M Whitesides. Patterning proteins and cells using soft lithography. In *The Biomaterials: Silver Jubilee Compendium*, pages 161–174. Elsevier, 2006.

[86] J Cooper McDonald and George M Whitesides. Poly (dimethylsiloxane) as a material for fabricating microfluidic devices. *Accounts of Chemical Research*, 35(7):491–499, 2002.

[87] Erwin Berthier, Edmond WK Young, and David Beebe. Engineers are from pdms-land, biologists are from polystyrenia. *Lab on a Chip*, 12(7):1224–1237, 2012.

[88] Nirveek Bhattacharjee, Arturo Urrios, Shawn Kang, and Albert Folch. The upcoming 3d-printing revolution in microfluidics. *Lab on a Chip*, 16(10):1720–1742, 2016.

[89] Jong Wook Hong and Stephen R Quake. Integrated nanoliter systems. *Nature Biotechnology*, 21(10):1179, 2003.

[90] Douglas B Weibel, Maarten Kruithof, Scott Potenta, Samuel K Sia, Andrew Lee, and George M Whitesides. Torque-actuated valves for microfluidics. *Analytical Chemistry*, 77(15):4726–4733, 2005.

[91] Daniel J Laser and Juan G Santiago. A review of micropumps. *Journal of Micromechanics and Microengineering*, 14(6):R35, 2004.

[92] Larry J Millet, Joshua D Lucheon, Robert F Standaert, Scott T Retterer, and Mitchel J Doktycz. Modular microfluidics for point-of-care protein purifications. *Lab on a Chip*, 15(8):1799–1811, 2015.

[93] TW Herling, T Müller, L Rajah, JN Skepper, M Vendruscolo, and TPJ Knowles. Integration and characterization of solid wall electrodes in microfluidic devices fabricated in a single photolithography step. *Applied Physics Letters*, 102(18):184102, 2013.

[94] Axel Günther, Manish Jhunjhunwala, Martina Thalmann, Martin A Schmidt, and Klavs F Jensen. Micromixing of miscible liquids in segmented gas-liquid flow. *Langmuir*, 21(4):1547–1555, 2005.

[95] Piotr Garstecki, Michael A Fischbach, and George M Whitesides. Design for mixing using bubbles in branched microfluidic channels. *Applied Physics Letters*, 86(24):244108, 2005.

[96] Piotr Garstecki, Irina Gitlin, Willow DiLuzio, George M Whitesides, Eugenia Kumacheva, and Howard A Stone. Formation of monodisperse bubbles in a microfluidic flow-focusing device. *Applied Physics Letters*, 85(13):2649–2651, 2004.

[97] Dongeun Huh, Geraldine A Hamilton, and Donald E Ingber. From 3d cell culture to organs-on-chips. *Trends in Cell Biology*, 21(12):745–754, 2011.

[98] Matthias Mehling and Savaş Tay. Microfluidic cell culture. *Current Opinion in Biotechnology*, 25:95–102, 2014.

[99] Bernhard H Weigl and Paul Yager. Microfluidic diffusion-based separation and detection. *Science*, 283(5400):346–347, 1999.

[100] Henrik Bruus. *Theoretical microfluidics*, volume 18. Oxford University Press, 2008.

[101] Paolo Arosio, Thomas Müller, Luke Rajah, Emma V Yates, Francesco A Aprile, Yingbo Zhang, Samuel IA Cohen, Duncan A White, Therese W Herling, Erwin J De Genst, et al. Microfluidic diffusion analysis of the sizes and interactions of proteins under native solution conditions. *ACS Nano*, 10(1):333–341, 2015.

[102] Paolo Arosio, Kevin Hu, Francesco A Aprile, Thomas Müller, and Tuomas PJ Knowles. Microfluidic diffusion viscometer for rapid analysis of complex solutions. *Analytical Chemistry*, 88(7):3488–3493, 2016.

[103] Emma V Yates, Thomas Müller, Luke Rajah, Erwin J De Genst, Paolo Arosio, Sara Linse, Michele Vendruscolo, Christopher M Dobson, and Tuomas PJ Knowles. Latent analysis of unmodified biomolecules and their complexes in solution with attomole detection sensitivity. *Nature Chemistry*, 7(10):802, 2015.

[104] Pavan Kumar Challa, Quentin Peter, Maya A Wright, Yuewen Zhang, Kadi L Saar, Jacqueline A Carozza, Justin LP Benesch, and Tuomas PJ Knowles. Real-time intrinsic fluorescence visualization and sizing of proteins and protein complexes in microfluidic devices. *Analytical Chemistry*, 90(6):3849–3855, 2018.

[105] Yuewen Zhang, Emma V Yates, Liu Hong, Kadi L Saar, Georg Meisl, Christopher M Dobson, and Tuomas PJ Knowles. On-chip measurements of protein unfolding from direct observations of micron-scale diffusion. *Chemical Science*, 9(14):3503–3507, 2018.

[106] Therese W Herling, Aviad Levin, Kadi L Saar, Christopher M Dobson, and Tuomas PJ Knowles. Microfluidic approaches for probing amyloid assembly and behaviour. *Lab on a Chip*, 18(7):999–1016, 2018.

[107] James Friend and Leslie Y Yeo. Microscale acoustofluidics: Microfluidics driven via acoustics and ultrasonics. *Reviews of Modern Physics*, 83(2):647, 2011.

[108] Ghulam Destgeer, Kyung Heon Lee, Jin Ho Jung, Anas Alazzam, and Hyung Jin Sung. Continuous separation of particles in a pdms microfluidic channel via travelling surface acoustic waves (tsaw). *Lab on a Chip*, 13(21):4210–4216, 2013.

[109] Maria Antfolk, Cecilia Magnusson, Per Augustsson, Hans Lilja, and Thomas Laurell. Acoustofluidic, label-free separation and simultaneous concentration of rare tumor cells from white blood cells. *Analytical Chemistry*, 87(18):9322–9328, 2015.

[110] Ghulam Destgeer, Hyunjun Cho, Byung Hang Ha, Jin Ho Jung, Jinsoo Park, and Hyung Jin Sung. Acoustofluidic particle manipulation inside a sessile droplet: four distinct regimes of particle concentration. *Lab on a Chip*, 16(4):660–667, 2016.

[111] Gianni Medoro, Nicoló Manaresi, Andrea Leonardi, Luigi Altomare, Marco Tartagni, and Roberto Guerrieri. A lab-on-a-chip for cell detection and manipulation. *IEEE Sensors Journal*, 3(3):317–325, 2003.

[112] Stefan Haeberle and Roland Zengerle. Microfluidic platforms for lab-on-a-chip applications. *Lab on a Chip*, 7(9):1094–1110, 2007.

[113] WS Mielczarek, EA Obaje, TT Bachmann, and M Kersaudy-Kerhoas. Microfluidic blood plasma separation for medical diagnostics: is it worth it? *Lab on a Chip*, 16(18):3441–3448, 2016.

[114] JG Santiago. Electroosmotic flows in microchannels with finite inertial and pressure forces. *Analytical Chemistry*, 73(10):2353–2365, 2001.

[115] Michael P Hughes. Strategies for dielectrophoretic separation in laboratory-on-a-chip systems. *Electrophoresis*, 23(16):2569–2582, 2002.

[116] Ryan T Turgeon and Michael T Bowser. Micro free-flow electrophoresis: theory and applications. *Analytical and Bioanalytical Chemistry*, 394(1):187–198, 2009.

[117] Kadi L Saar, Yingbo Zhang, Thomas Müller, Challa P Kumar, Sean Devenish, Andrew Lynn, Urszula Łapińska, Xiaoting Yang, Sara Linse, and Tuomas PJ Knowles. On-chip label-free protein analysis with downstream electrodes for direct removal of electrolysis products. *Lab on a Chip*, 18(1):162–170, 2018.

[118] Therese W Herling, Paolo Arosio, Thomas Müller, Sara Linse, and Tuomas PJ Knowles. A microfluidic platform for quantitative measurements of effective protein charges and single ion binding in solution. *Physical Chemistry Chemical Physics*, 17(18):12161–12167, 2015.

[119] Roberto Gambari, Monica Borgatti, Luigi Altomare, Nicolo Manaresi, Gianni Medoro, Aldo Romani, Marco Tartagni, and Roberto Guerrieri. Applications to cancer research of "lab-on-a-chip" devices based on dielectrophoresis (dep). *Technology in Cancer Research & Treatment*, 2(1):31–39, 2003.

[120] Jian Chen, Jason Li, and Yu Sun. Microfluidic approaches for cancer cell detection, characterization, and separation. *Lab on a Chip*, 12(10):1753–1767, 2012.

[121] DR Link, Shelley L Anna, DA Weitz, and HA Stone. Geometrically mediated breakup of drops in microfluidic devices. *Physical Review Letters*, 92(5):054503, 2004.

[122] Ralf Seemann, Martin Brinkmann, Thomas Pfohl, and Stephan Herminghaus. Droplet based microfluidics. *Reports on Progress in Physics*, 75(1):016601, 2011.

[123] Assaf Rotem, Adam R Abate, Andrew S Utada, Volkert Van Steijn, and David A Weitz. Drop formation in non-planar microfluidic devices. *Lab on a Chip*, 12(21):4263–4268, 2012.

[124] Monya Baker. Digital PCR hits its stride. *Nature Methods*, 9:541–544, 2012.

[125] Yonghao Zhang and Pinar Ozdemir. Microfluidic DNA amplification—a review. *Analytica Chimica Acta*, 638(2):115–125, 2009.

[126] Dennis J Eastburn, Adam Sciambi, and Adam R Abate. Ultrahigh-throughput mammalian single-cell reverse-transcriptase polymerase chain reaction in microfluidic drops. *Analytical Chemistry*, 85(16):8016–8021, 2013.

[127] Aviad Levin, Thomas CT Michaels, Lihi Adler-Abramovich, Thomas O Mason, Thomas Müller, Bohan Zhang, L Mahadevan, Ehud Gazit, and Tuomas PJ Knowles. Elastic instability-mediated actuation by a supra-molecular polymer. *Nature Physics*, 12(10):926, 2016.

[128] Sarah Köster, Francesco E Angile, Honey Duan, Jeremy J Agresti, Anton Wintner, Christian Schmitz, Amy C Rowat, Christoph A Merten, Dario Pisignano, Andrew D Griffiths, et al. Drop-based microfluidic devices for encapsulation of single cells. *Lab on a Chip*, 8(7):1110–1115, 2008.

[129] Linas Mazutis, John Gilbert, W Lloyd Ung, David A Weitz, Andrew D Griffiths, and John A Heyman. Single-cell analysis and sorting using droplet-based microfluidics. *Nature Protocols*, 8(5):870, 2013.

[130] Evan Z Macosko, Anindita Basu, Rahul Satija, James Nemesh, Karthik Shekhar, Melissa Goldman, Itay Tirosh, Allison R Bialas, Nolan Kamitaki, Emily M Martersteck, et al. Highly parallel genome-wide expression profiling of individual cells using nanoliter droplets. *Cell*, 161(5):1202–1214, 2015.

[131] Lindsey W Plasschaert, Rapolas Žilionis, Rayman Choo-Wing, Virginia Savova, Judith Knehr, Guglielmo Roma, Allon M Klein, and Aron B Jaffe. A single-cell atlas of the airway epithelium reveals the cftr-rich pulmonary ionocyte. *Nature*, 560(7718):377, 2018.

[132] Arjun P Sudarsan and Victor M Ugaz. Fluid mixing in planar spiral microchannels. *Lab on a Chip*, 6(1):74–82, 2006.

[133] Hamed Amini, Wonhee Lee, and Dino Di Carlo. Inertial microfluidic physics. *Lab on a Chip*, 14(15):2739–2761, 2014.

[134] Kanaka Hettiarachchi, Esra Talu, Marjorie L Longo, Paul A Dayton, and Abraham P Lee. On-chip generation of microbubbles as a practical technology for manufacturing contrast agents for ultrasonic imaging. *Lab on a Chip*, 7(4):463–468, 2007.

[135] Sally A Peyman, Radwa H Abou-Saleh, James R McLaughlan, Nicola Ingram, Benjamin RG Johnson, Kevin Critchley, Steven Freear, J Anthony Evans, Alexander F Markham, P Louise Coletta, et al. Expanding 3d geometry for enhanced on-chip microbubble production and single step formation of liposome modified microbubbles. *Lab on a Chip*, 12(21):4544–4552, 2012.

[136] Esther Amstad, Manesh Gopinadhan, Christian Holtze, Chinedum O Osuji, Michael P Brenner, Frans Spaepen, and David A Weitz. Production of amorphous nanoparticles by supersonic spray-drying with a microfluidic nebulator. *Science*, 349(6251):956–960, 2015.

[137] Esther Amstad, Frans Spaepen, Michael P Brenner, and David A Weitz. The microfluidic nebulator: production of sub-micrometer sized airborne drops. *Lab on a Chip*, 17(8):1475–1480, 2017.

[138] Richard P Feynman. There's plenty of room at the bottom [data storage]. *Journal of Microelectromechanical Systems*, 1(1):60–66, 1992.

[139] Chris Toumey. Plenty of room, plenty of history. *Nature Nanotechnology*, 4(12):783, 2009.

[140] Joseph A Stroscio and Robert J Celotta. Controlling the dynamics of a single atom in lateral atom manipulation. *Science*, 306(5694):242–247, 2004.

[141] Leo Gross, Fabian Mohn, Nikolaj Moll, Peter Liljeroth, and Gerhard Meyer. The chemical structure of a molecule resolved by atomic force microscopy. *Science*, 325(5944):1110–1114, 2009.

[142] Jacob K Rosenstein, Meni Wanunu, Christopher A Merchant, Marija Drndic, and Kenneth L Shepard. Integrated nanopore sensing platform with sub-microsecond temporal resolution. *Nature Methods*, 9(5):487, 2012.

[143] Nicholas AW Bell, Christian R Engst, Marc Ablay, Giorgio Divitini, Caterina Ducati, Tim Liedl, and Ulrich F Keyser. DNA origami nanopores. *Nano Letters*, 12(1):512–517, 2011.

[144] Ulrich F Keyser. Enhancing nanopore sensing with DNA nanotechnology. *Nature Nanotechnology*, 11(2):106, 2016.

[145] James Clarke, Hai-Chen Wu, Lakmal Jayasinghe, Alpesh Patel, Stuart Reid, and Hagan Bayley. Continuous base identification for single-molecule nanopore DNA sequencing. *Nature Nanotechnology*, 4(4):265, 2009.

[146] Jan CT Eijkel and Albert Van Den Berg. Nanofluidics: what is it and what can we expect from it? *Microfluidics and Nanofluidics*, 1(3):249–267, 2005.

[147] Seung-min Park, Yun Suk Huh, Harold G Craighead, and David Erickson. A method for nanofluidic device prototyping using elastomeric collapse. *Proceedings of the National Academy of Sciences*, 106(37):15549–15554, 2009.

[148] Rohit Karnik, Kenneth Castelino, and Arun Majumdar. Field-effect control of protein transport in a nanofluidic transistor circuit. *Applied Physics Letters*, 88(12):123114, 2006.

[149] Prashanta Dutta and Ali Beskok. Analytical solution of combined electroosmotic/pressure driven flows in two-dimensional straight channels: finite Debye layer effects. *Analytical Chemistry*, 73(9):1979–1986, 2001.

[150] Lyderic Bocquet and Patrick Tabeling. Physics and technological aspects of nanofluidics. *Lab on a Chip*, 14(17):3143–3158, 2014.

[151] Curtis D Chin, Tassaneewan Laksanasopin, Yuk Kee Cheung, David Steinmiller, Vincent Linder, Hesam Parsa, Jennifer Wang, Hannah Moore, Robert Rouse, Gisele Umviligihozo, et al. Microfluidics-based diagnostics of infectious diseases in the developing world. *Nature Medicine*, 17(8):1015, 2011.

[152] Vijay Srinivasan, Vamsee K Pamula, and Richard B Fair. An integrated digital microfluidic lab-on-a-chip for clinical diagnostics on human physiological fluids. *Lab on a Chip*, 4(4):310–315, 2004.

[153] Zhiqiang Du, N Colls, Kwan H Cheng, Mark W Vaughn, and L Gollahon. Microfluidic-based diagnostics for cervical cancer cells. *Biosensors and Bioelectronics*, 21(10):1991–1995, 2006.

[154] Jeremy J Agresti, Eugene Antipov, Adam R Abate, Keunho Ahn, Amy C Rowat, Jean-Christophe Baret, Manuel Marquez, Alexander M Klibanov, Andrew D Griffiths, and David A Weitz. Ultrahigh-throughput screening in drop-based microfluidics for directed evolution. *Proceedings of the National Academy of Sciences*, 107(9):4004–4009, 2010.

[155] Doron Gerber, Sebastian J Maerkl, and Stephen R Quake. An in vitro microfluidic approach to generating protein-interaction networks. *Nature Methods*, 6(1):71, 2009.

[156] Alexander Linden and Jackie Fenn. Understanding Gartner's hype cycles. *Strategic Analysis Report Nº R-20-1971. Gartner, Inc*, 2003.

[157] William E Cox. Product life cycles as marketing models. *The Journal of Business*, 40(4):375–384, 1967.

[158] Bradley C Edwards. Design and deployment of a space elevator. *Acta Astronautica*, 47(10):735–744, 2000.

[159] Microfluidics market outlook. https://www.i-micronews.com/category-listing/product/status-of-the-microfluidics-industry-2017.html. Accessed: 2018-09-01.

[160] H Sirringhaus, T Kawase, RH Friend, T Shimoda, M Inbasekaran, W Wu, and EP Woo. High-resolution inkjet printing of all-polymer transistor circuits. *Science*, 290(5499):2123–2126, 2000.

[161] Md Jasim Uddin, Nicolaos Scoutaris, Pavlos Klepetsanis, Babur Chowdhry, Mark R Prausnitz, and Dennis Douroumis. Inkjet printing of transdermal microneedles for the delivery of anticancer agents. *International Journal of Pharmaceutics*, 494(2):593–602, 2015.

[162] Kevin C Krogman, Joseph L Lowery, Nicole S Zacharia, Gregory C Rutledge, and Paula T Hammond. Spraying asymmetry into functional membranes layer-by-layer. *Nature Materials*, 8(6):512, 2009.

[163] Thibaut Martini, Caroline Chubilleau, Olivier Poncelet, Alain Ricaud, Anne Blayo, Celine Martin, and Konstantin Tarasov. Spray and inkjet fabrication of Cu_2ZnSnS_4 thin films using nanoparticles derived from a continuous-flow microwave-assisted synthesis. *Solar Energy Materials and Solar Cells*, 144:657–663, 2016.

[164] Ferry Iskandar. Nanoparticle processing for optical applications–a review. *Advanced Powder Technology*, 20(4):283–292, 2009.

[165] Ian A Harding, Robert Justice Shartle, Glenn Renowitzky, and Lewis Leung. Micro-droplet dispensing for a medical diagnostic device, December 14 2004. US Patent 6,830,934.

[166] Philippe Marmottant and Emmanuel Villermaux. On spray formation. *Journal of Fluid Mechanics*, 498:73–111, 2004.

[167] Madhusudan Singh, Hanna M Haverinen, Parul Dhagat, and Ghassan E Jabbour. Inkjet printing—process and its applications. *Advanced Materials*, 22(6):673–685, 2010.

[168] John B Fenn, Matthias Mann, Chin Kai Meng, Shek Fu Wong, and Craige M Whitehouse. Electrospray ionization–principles and practice. *Mass Spectrometry Reviews*, 9(1):37–70, 1990.

[169] HY Gan, Xuechuan Shan, T Eriksson, BK Lok, and YC Lam. Reduction of droplet volume by controlling actuating waveforms in inkjet printing for micro-pattern formation. *Journal of Micromechanics and Microengineering*, 19(5):055010, 2009.

[170] Brian Derby. Bioprinting: inkjet printing proteins and hybrid cell-containing materials and structures. *Journal of Materials Chemistry*, 18(47):5717–5721, 2008.

[171] Ramesh Murugesan and Valérie Orsat. Spray drying for the production of nutraceutical ingredients—a review. *Food and Bioprocess Technology*, 5(1):3–14, 2012.

[172] Kikuo Okuyama, Mikrajuddin Abdullah, I Wuled Lenggoro, and Ferry Iskandar. Preparation of functional nanostructured particles by spray drying. *Advanced Powder Technology*, 17(6):587–611, 2006.

[173] Amrit Paudel, Zelalem Ayenew Worku, Joke Meeus, Sandra Guns, and Guy Van den Mooter. Manufacturing of solid dispersions of poorly water soluble drugs by spray drying: formulation and process considerations. *International Journal of Pharmaceutics*, 453(1):253–284, 2013.

[174] Krzysztof Cal and Krzysztof Sollohub. Spray drying technique. i: Hardware and process parameters. *Journal of Pharmaceutical Sciences*, 99(2):575–586, 2010.

[175] Okawara mfg co., ltd. http://www.oc-sd.co.jp/english/atomization.html. Accessed: 2018-08-21.

[176] Cordin Arpagaus. A novel laboratory-scale spray dryer to produce nanoparticles. *Drying Technology*, 30(10):1113–1121, 2012.

[177] Martin Trebbin, Kilian Krüger, Daniel DePonte, Stephan V Roth, Henry N Chapman, and Stephan Förster. Microfluidic liquid jet system with compatibility for atmospheric and high-vacuum conditions. *Lab on a Chip*, 14(10):1733–1745, 2014.

[178] Lord Rayleigh. On the stability, or instability, of certain fluid motions. *Proceedings of the London Mathematical Society*, 1(1):57–72, 1879.

[179] Julian Thiele, Maike Windbergs, Adam R Abate, Martin Trebbin, Ho Cheung Shum, Stephan Förster, and David A Weitz. Early development drug formulation on a chip: Fabrication of nanoparticles using a microfluidic spray dryer. *Lab on a Chip*, 11(14):2362–2368, 2011.

[180] Cilong Yu, Xiang Qian, Yan Chen, Quan Yu, Kai Ni, and Xiaohao Wang. Three-dimensional electro-sonic flow focusing ionization microfluidic chip for mass spectrometry. *Micromachines*, 6(12):1890–1902, 2015.

[181] Pavan K Challa, Tadas Kartanas, Jérôme Charmet, and Tuomas PJ Knowles. Microfluidic devices fabricated using fast wafer-scale led-lithography patterning. *Biomicrofluidics*, 11(1):014113, 2017.

[182] B-H Jo, Linda M Van Lerberghe, Kathleen M Motsegood, and David J Beebe. Three-dimensional micro-channel fabrication in polydimethylsiloxane (pdms) elastomer. *Journal of Microelectromechanical Systems*, 9(1):76–81, 2000.

[183] Jeongyun Y Kim, Juyeoul Y Baek, Kyam A Lee, and Sanghoon H Lee. Automatic aligning and bonding system of pdms layer for the fabrication of 3d microfluidic channels. *Sensors and Actuators A: Physical*, 119(2):593–598, 2005.

[184] Francesco Simone Ruggeri, Jerome Charmet, Tadas Kartanas, Quentin Peter, Sean Chia, Johnny Habchi, Christopher M Dobson, Michele Vendruscolo, and Tuomas PJ Knowles. Microfluidic deposition for resolving single-molecule protein architecture and heterogeneity. *Nature communications*, 9(1):3890, 2018.

[185] Patrick Flagmeier, Georg Meisl, Michele Vendruscolo, Tuomas PJ Knowles, Christopher M Dobson, Alexander K Buell, and Céline Galvagnion. Mutations associated with familial Parkinson's disease alter the initiation and amplification steps of α-synuclein aggregation. *Proceedings of the National Academy of Sciences*, 113(37):10328–10333, 2016.

[186] Peter Dybdahl Hede, Poul Bach, and Anker D Jensen. Two-fluid spray atomisation and pneumatic nozzles for fluid bed coating/agglomeration purposes: A review. *Chemical Engineering Science*, 63(14):3821–3842, 2008.

[187] Merle C Potter, David C Wiggert, and Bassem H Ramadan. *Mechanics of fluids*. Nelson Education, 2016.

[188] Pratim Biswas and Richard C Flagan. High-velocity inertial impactors. *Environmental Science & Technology*, 18(8):611–616, 1984.

[189] K Triballier, C Dumouchel, and J Cousin. A technical study on the spraytec performances: influence of multiple light scattering and multi-modal drop-size distribution measurements. *Experiments in Fluids*, 35(4):347–356, 2003.

[190] Juan C Lasheras and EJ Hopfinger. Liquid jet instability and atomization in a coaxial gas stream. *Annual Review of Fluid Mechanics*, 32(1):275–308, 2000.

[191] Jonathan Barrett and Charles Clement. Kinetic evaporation and condensation rates and their coefficients. *Journal of Colloid and Interface Science*, 150(2):352–364, 1992.

[192] Eric W Weisstein. Spherical cap. *www.mathworld.wolfram.com/SphericalCap.html*, 2008.

[193] Céline Sadek, Pierre Schuck, Yannick Fallourd, Nicolas Pradeau, Cécile Le Floch-Fouéré, and Romain Jeantet. Drying of a single droplet to investigate process–structure–function relationships: a review. *Dairy Science & Technology*, 95(6):771–794, 2015.

[194] CK Law. Recent advances in droplet vaporization and combustion. *Progress in Energy and Combustion Science*, 8(3):171–201, 1982.

[195] Vincent Chan, David J Graves, Paolo Fortina, and Steven E McKenzie. Adsorption and surface diffusion of DNA oligonucleotides at liquid/solid interfaces. *Langmuir*, 13(2):320–329, 1997.

[196] Daniel J Müller and Andreas Engel. Atomic force microscopy and spectroscopy of native membrane proteins. *Nature Protocols*, 2(9):2191, 2007.

[197] Pedro J de Pablo and Mariano Carrión-Vázquez. Imaging biological samples with atomic force microscopy. *Cold Spring Harbor Protocols*, 2014(2):pdb–top080473, 2014.

[198] Frank Ostendorf, Carsten Schmitz, Sabine Hirth, Angelika Kühnle, Jacek J Kolodziej, and Michael Reichling. How flat is an air-cleaved mica surface? *Nanotechnology*, 19(30):305705, 2008.

[199] Francesco Simone Ruggeri, Jozef Adamcik, Jae Sun Jeong, Hilal A Lashuel, Raffaele Mezzenga, and Giovanni Dietler. Influence of the β-sheet content on the mechanical properties of aggregates during amyloid fibrillization. *Angewandte Chemie*, 127(8):2492–2496, 2015.

[200] Johnny Habchi, Sean Chia, Céline Galvagnion, Thomas CT Michaels, Mathias MJ Bellaiche, Francesco Simone Ruggeri, Michele Sanguanini, Ilaria Idini, Janet R Kumita, Emma Sparr, et al. Cholesterol catalyses aβ42 aggregation through a heterogeneous nucleation pathway in the presence of lipid membranes. *Nature Chemistry*, 10(6):673, 2018.

[201] Jongin Hong, Joshua B Edel, et al. Micro-and nanofluidic systems for high-throughput biological screening. *Drug Discovery Today*, 14(3-4):134–146, 2009.

[202] Minhaz Uddin Ahmed, Ishtiaq Saaem, Pae C Wu, and April S Brown. Personalized diagnostics and biosensors: a review of the biology and technology needed for personalized medicine. *Critical Reviews in Biotechnology*, 34(2):180–196, 2014.

[203] Helen Bridle, Wenxing Wang, Despoina Gavriilidou, Farid Amalou, Duncan P Hand, and Wenmiao Shu. Static mode microfluidic cantilevers for detection of waterborne pathogens. *Sensors and Actuators A: Physical*, 247:144–149, 2016.

[204] Ya-Tang Yang, Carlo Callegari, XL Feng, Kamil L Ekinci, and Michael L Roukes. Zeptogram-scale nanomechanical mass sensing. *Nano Letters*, 6(4):583–586, 2006.

[205] Cyril Vančura, Isabelle Dufour, Stephen M Heinrich, Fabien Josse, and Andreas Hierlemann. Analysis of resonating microcantilevers operating in a viscous liquid environment. *Sensors and Actuators A: Physical*, 141(1):43–51, 2008.

[206] Philip S Waggoner, Christine P Tan, Leon Bellan, and Harold G Craighead. High-Q, in-plane modes of nanomechanical resonators operated in air. *Journal of Applied Physics*, 105(9):094315, 2009.

[207] Ville Kaajakari, Tomi Mattila, Aarne Oja, Jyrki Kiihamaki, and Heikki Seppa. Square-extensional mode single-crystal silicon micromechanical resonator for low-phase-noise oscillator applications. *IEEE Electron Device Letters*, 25(4):173–175, 2004.

[208] Reza Abdolvand, Houri Johari, Gavin K Ho, Ahmet Erbil, and Farrokh Ayazi. Quality factor in trench-refilled polysilicon beam resonators. *Journal of Microelectromechanical Systems*, 15(3):471–478, 2006.

[209] Scott S Verbridge, Rob Ilic, HG Craighead, and Jeevak M Parpia. Size and frequency dependent gas damping of nanomechanical resonators. *Applied Physics Letters*, 93(1):013101, 2008.

[210] James WM Chon, Paul Mulvaney, and John E Sader. Experimental validation of theoretical models for the frequency response of atomic force microscope cantilever beams immersed in fluids. *Journal of Applied Physics*, 87(8):3978–3988, 2000.

[211] Tae Yun Kwon, Kilho Eom, Jae Hong Park, Dae Sung Yoon, Tae Song Kim, and Hong Lim Lee. In situ real-time monitoring of biomolecular interactions based on resonating microcantilevers immersed in a viscous fluid. *Applied Physics Letters*, 90(22):223903, 2007.

[212] Scott S Verbridge, Leon M Bellan, Jeevak M Parpia, and HG Craighead. Optically driven resonance of nanoscale flexural oscillators in liquid. *Nano Letters*, 6(9):2109–2114, 2006.

[213] D Ramos, J Tamayo, Johann Mertens, and Montserrat Calleja. Photothermal excitation of microcantilevers in liquids. *Journal of Applied Physics*, 99(12):124904, 2006.

[214] Cyril Vančura, Jan Lichtenberg, Andreas Hierlemann, and Fabien Josse. Characterization of magnetically actuated resonant cantilevers in viscous fluids. *Applied Physics Letters*, 87(16):162510, 2005.

[215] Abdelhamid Maali, Cedric Hurth, Rodolphe Boisgard, Cédric Jai, Touria Cohen-Bouhacina, and Jean-Pierre Aimé. Hydrodynamics of oscillating atomic force microscopy cantilevers in viscous fluids. *Journal of Applied Physics*, 97(7):074907, 2005.

[216] Kiran Menon, Reenu Anne Joy, Neeru Sood, and RK Mittal. The applications of biomems in diagnosis, cell biology, and therapy: a review. *BioNanoScience*, 3(4):356–366, 2013.

[217] Jing Wu and Min Gu. Microfluidic sensing: state of the art fabrication and detection techniques. *Journal of Biomedical Optics*, 16(8):080901, 2011.

[218] Onursal Onen, Asad A Ahmad, Rasim Guldiken, and Nathan D Gallant. Surface modification on acoustic wave biosensors for enhanced specificity. *Sensors*, 12(9):12317–12328, 2012.

[219] Massimo S Fiandaca, Mark E Mapstone, Amrita K Cheema, and Howard J Federoff. The critical need for defining preclinical biomarkers in Alzheimer's disease. *Alzheimer's & Dementia*, 10(3):S196–S212, 2014.

[220] Maria Andreasen, Nikolai Lorenzen, and Daniel Otzen. Interactions between misfolded protein oligomers and membranes: A central topic in neurodegenerative diseases? *Biochimica et Biophysica Acta (BBA)-Biomembranes*, 1848(9):1897–1907, 2015.

[221] Ji Homola, Sinclair S Yee, and Günter Gauglitz. Surface plasmon resonance sensors. *Sensors and Actuators B: Chemical*, 54(1-2):3–15, 1999.

[222] Cathy I Cheng, Yi-Pin Chang, and Yen-Ho Chu. Biomolecular interactions and tools for their recognition: focus on the quartz crystal microbalance and its diverse surface chemistries and applications. *Chemical Society Reviews*, 41(5):1947–1971, 2012.

[223] Robert E Speight and Matthew A Cooper. A survey of the 2010 quartz crystal microbalance literature. *Journal of Molecular Recognition*, 25(9):451–473, 2012.

[224] Todd M Squires, Robert J Messinger, and Scott R Manalis. Making it stick: convection, reaction and diffusion in surface-based biosensors. *Nature Biotechnology*, 26(4):417, 2008.

[225] Thomas P Burg, Michel Godin, Scott M Knudsen, Wenjiang Shen, Greg Carlson, John S Foster, Ken Babcock, and Scott R Manalis. Weighing of biomolecules, single cells and single nanoparticles in fluid. *Nature*, 446(7139):1066, 2007.

[226] Selim Olcum, Nathan Cermak, Steven C Wasserman, Kathleen S Christine, Hiroshi Atsumi, Kris R Payer, Wenjiang Shen, Jungchul Lee, Angela M Belcher, Sangeeta N Bhatia, et al. Weighing nanoparticles in solution at the attogram scale. *Proceedings of the National Academy of Sciences*, 111(4):1310–1315, 2014.

[227] Mario M Modena, Yu Wang, Dietmar Riedel, and Thomas P Burg. Resolution enhancement of suspended microchannel resonators for weighing of biomolecular complexes in solution. *Lab on a Chip*, 14(2):342–350, 2014.

[228] Selim Olcum, Nathan Cermak, Steven C Wasserman, and Scott R Manalis. High-speed multiple-mode mass-sensing resolves dynamic nanoscale mass distributions. *Nature Communications*, 6:7070, 2015.

[229] Takaharu Okajima, Hiroshi Sekiguchi, Hideo Arakawa, and Atsushi Ikai. Self-oscillation technique for afm in liquids. *Applied Surface Science*, 210(1-2):68–72, 2003.

[230] Blake N Johnson and Raj Mutharasan. Biosensing using dynamic-mode cantilever sensors: A review. *Biosensors and Bioelectronics*, 32(1):1–18, 2012.

[231] Elmar Bonaccurso and Hans-Jürgen Butt. Microdrops on atomic force microscope cantilevers: evaporation of water and spring constant calibration. *The Journal of Physical Chemistry B*, 109(1):253–263, 2005.

[232] William P Robins. *Phase noise in signal sources: theory and applications*, volume 9. IET, 1984.

[233] John R Vig and Yoonkee Kim. Noise in microelectromechanical system resonators. *IEEE Transactions on Ultrasonics, Ferroelectrics, and Frequency Control*, 46(6):1558–1565, 1999.

[234] Carolyn A Haskard and Eunice CY Li-Chan. Hydrophobicity of bovine serum albumin and ovalbumin determined using uncharged (prodan) and anionic (ans-) fluorescent probes. *Journal of Agricultural and Food Chemistry*, 46(7):2671–2677, 1998.

[235] Nicole Pamme. Continuous flow separations in microfluidic devices. *Lab on a Chip*, 7(12):1644–1659, 2007.

[236] Andreas Lenshof and Thomas Laurell. Continuous separation of cells and particles in microfluidic systems. *Chemical Society Reviews*, 39(3):1203–1217, 2010.

[237] Nguyen TK Thanh and Luke AW Green. Functionalisation of nanoparticles for biomedical applications. *Nano Today*, 5(3):213–230, 2010.

[238] James P Brody and Paul Yager. Diffusion-based extraction in a microfabricated device. *Sensors and Actuators-A-Physical Sensors*, 58(1):13–18, 1997.

[239] Michele Celebrano, Philipp Kukura, Alois Renn, and Vahid Sandoghdar. Single-molecule imaging by optical absorption. *Nature Photonics*, 5(2):95, 2011.

[240] Susan Jones and Janet M Thornton. Principles of protein-protein interactions. *Proceedings of the National Academy of Sciences*, 93(1):13–20, 1996.

[241] Adriano Aguzzi and Tracy O'connor. Protein aggregation diseases: pathogenicity and therapeutic perspectives. *Nature reviews Drug Discovery*, 9(3):237, 2010.

[242] Alexander Star, Eugene Tu, Joseph Niemann, Jean-Christophe P Gabriel, C Steve Joiner, and Christian Valcke. Label-free detection of DNA hybridization using carbon nanotube network field-effect transistors. *Proceedings of the National Academy of Sciences*, 103(4):921–926, 2006.

[243] Yi Xiao, Arica A Lubin, Alan J Heeger, and Kevin W Plaxco. Label-free electronic detection of thrombin in blood serum by using an aptamer-based sensor. *Angewandte Chemie*, 117(34):5592–5595, 2005.

[244] Sandeep Kumar Vashist, E Marion Schneider, and John HT Luong. Commercial smartphone-based devices and smart applications for personalized healthcare monitoring and management. *Diagnostics*, 4(3):104–128, 2014.

[245] Jan Weile and Cornelius Knabbe. Current applications and future trends of molecular diagnostics in clinical bacteriology. *Analytical and Bioanalytical Chemistry*, 394(3):731–742, 2009.

[246] Daniel Otzen. Functional amyloid: turning swords into plowshares. *Prion*, 4(4):256–264, 2010.

[247] Felix JH Hol and Cees Dekker. Zooming in to see the bigger picture: microfluidic and nanofabrication tools to study bacteria. *Science*, 346(6208):1251821, 2014.

[248] Wayne U Wang, Chuo Chen, Keng-hui Lin, Ying Fang, and Charles M Lieber. Label-free detection of small-molecule–protein interactions by using nanowire nanosensors. *Proceedings of the National Academy of Sciences*, 102(9):3208–3212, 2005.

[249] Günter Sauerbrey. Verwendung von schwingquarzen zur wägung dünner schichten und zur mikrowägung. *Zeitschrift für Physik*, 155(2):206–222, 1959.

[250] J Hlavay and GG Guilbault. Applications of the piezoelectric crystal detector in analytical chemistry. *Analytical Chemistry*, 49(13):1890–1898, 1977.

[251] K Keiji Kanazawa and Joseph G Gordon II. The oscillation frequency of a quartz resonator in contact with liquid. *Analytica Chimica Acta*, 175:99–105, 1985.

[252] Jan Rickert, Andreas Brecht, and Wolfgang Göpel. Qcm operation in liquids: constant sensitivity during formation of extended protein multilayers by affinity. *Analytical Chemistry*, 69(7):1441–1448, 1997.

[253] Tuomas PJ Knowles, Wenmiao Shu, Glyn L Devlin, Sarah Meehan, Stefan Auer, Christopher M Dobson, and Mark E Welland. Kinetics and thermodynamics of amyloid formation from direct measurements of fluctuations in fibril mass. *Proceedings of the National Academy of Sciences*, 104(24):10016–10021, 2007.

[254] Benjamin Godber, Mark Frogley, Marian Rehak, Alexander Sleptsov, Kevin SJ Thompson, Yildiz Uludag, and Matthew A Cooper. Profiling of molecular interactions in real time using acoustic detection. *Biosensors and Bioelectronics*, 22(9-10):2382–2386, 2007.

[255] Nicola Doy, Glen McHale, MI Newton, Christopher Hardacre, Rile Ge, JM MacInnes, Dmitriy Kuvshinov, and RW Allen. Small volume laboratory on a chip measurements incorporating the quartz crystal microbalance to measure the viscosity-density product of room temperature ionic liquids. *Biomicrofluidics*, 4(1):014107, 2010.

[256] T Müller, DA White, and TPJ Knowles. Dry-mass sensing for microfluidics. *Applied Physics Letters*, 105(21):214101, 2014.

[257] Tadas Kartanas, Victor Ostanin, Pavan Kumar Challa, Ronan Daly, Jerome Charmet, and Tuomas PJ Knowles. Enhanced quality factor label-free biosensing with microcantilevers integrated into microfluidic systems. *Analytical Chemistry*, 89(22):11929–11936, 2017.

[258] Bin-Da Chan, Kutay Icoz, Wanfeng Huang, Chun-Li Chang, and Cagri A Savran. On-demand weighing of single dry biological particles over a 5-order-of-magnitude dynamic range. *Lab on a Chip*, 14(21):4188–4196, 2014.

[259] Olivier Lazcka, F Javier Del Campo, and F Xavier Munoz. Pathogen detection: A perspective of traditional methods and biosensors. *Biosensors and Bioelectronics*, 22(7):1205–1217, 2007.

[260] Arun K Bhunia. Biosensors and bio-based methods for the separation and detection of foodborne pathogens. In *Advances in Food and Nutrition Research*, volume 54, pages 1–44. Elsevier, 2008.

[261] Lloyd R Snyder, Joseph J Kirkland, and John W Dolan. *Introduction to modern liquid chromatography*. John Wiley & Sons, 2011.

[262] Sadao Mori and Howard G Barth. *Size exclusion chromatography*. Springer Science & Business Media, 2013.

[263] Jin Tamaoka and Kazuo Komagata. Determination of DNA base composition by reversed-phase high-performance liquid chromatography. *FEMS Microbiology Letters*, 25(1):125–128, 1984.

[264] Alois Jungbauer and Rainer Hahn. *Ion-exchange chromatography*, volume 463. Elsevier, 2009.

[265] Pedro Cuatrecasas. Protein purification by affinity chromatography derivatizations of agarose and polyacrylamide beads. *Journal of Biological Chemistry*, 245(12):3059–3065, 1970.

[266] Scott B Ficarro, Arthur R Salomon, Laurence M Brill, Daniel E Mason, Michelle Stettler-Gill, Ansgar Brock, and Eric C Peters. Automated immobilized metal affinity chromatography/nano-liquid chromatography/electrospray ionization mass spectrometry platform for profiling protein phosphorylation sites. *Rapid Communications in Mass Spectrometry: An International Journal Devoted to the Rapid Dissemination of Up-to-the-Minute Research in Mass Spectrometry*, 19(1):57–71, 2005.

[267] Benjamin J Cargile, Jonathan L Bundy, Thaddeus W Freeman, and James L Stephenson. Gel based isoelectric focusing of peptides and the utility of isoelectric point in protein identification. *Journal of Proteome Research*, 3(1):112–119, 2004.

[268] Otto G Berg and Peter H von Hippel. Diffusion-controlled macromolecular interactions. *Annual Review of Biophysics and Biophysical Chemistry*, 14(1):131–158, 1985.

[269] Adam D Catherman, Owen S Skinner, and Neil L Kelleher. Top down proteomics: facts and perspectives. *Biochemical and Biophysical Research Communications*, 445(4):683–693, 2014.

[270] Adam D Catherman, Kenneth R Durbin, Dorothy R Ahlf, Bryan P Early, Ryan T Fellers, John C Tran, Paul M Thomas, and Neil L Kelleher. Large-scale top-down proteomics of the human proteome: membrane proteins, mitochondria, and senescence. *Molecular & Cellular Proteomics*, 12(12):3465–3473, 2013.

[271] Albert JR Heck. Native mass spectrometry: a bridge between interactomics and structural biology. *Nature Methods*, 5(11):927, 2008.

[272] Pierre C Havugimana, G Traver Hart, Tamás Nepusz, Haixuan Yang, Andrei L Turinsky, Zhihua Li, Peggy I Wang, Daniel R Boutz, Vincent Fong, Sadhna Phanse, et al. A census of human soluble protein complexes. *Cell*, 150(5):1068–1081, 2012.

[273] Hans JCT Wessels, Rutger O Vogel, Robert N Lightowlers, Johannes N Spelbrink, Richard J Rodenburg, Lambert P van den Heuvel, Alain J van Gool, Jolein Gloerich, Jan AM Smeitink, and Leo G Nijtmans. Analysis of 953 human proteins from a mitochondrial hek293 fraction by complexome profiling. *PLoS One*, 8(7):e68340, 2013.

[274] John Cavanagh, Wayne J Fairbrother, Arthur G Palmer III, and Nicholas J Skelton. *Protein NMR spectroscopy: principles and practice*. Elsevier, 1995.

[275] Ernesto Freire, Obdulio L Mayorga, and Martin Straume. Isothermal titration calorimetry. *Analytical Chemistry*, 62(18):950A–959A, 1990.

[276] Joseph R Lakowicz. Principles of frequency-domain fluorescence spectroscopy and applications to cell membranes. In *Fluorescence Studies on Biological Membranes*, pages 89–126. Springer, 1988.

[277] WI Goldburg. Dynamic light scattering. *American Journal of Physics*, 67(12):1152–1160, 1999.

[278] Mats Andersson, Bengt Wittgren, and Karl-Gustav Wahlund. Accuracy in multiangle light scattering measurements for molar mass and radius estimations. model calculations and experiments. *Analytical Chemistry*, 75(16):4279–4291, 2003.

[279] Klaus Weber and Mary Osborn. The reliability of molecular weight determinations by dodecyl sulfate-polyacrylamide gel electrophoresis. *Journal of Biological Chemistry*, 244(16):4406–4412, 1969.

[280] Allen P Minton. Quantitative characterization of reversible molecular associations via analytical centrifugation. *Analytical Biochemistry*, 190(1):1–6, 1990.

[281] Samuel Cohen, Tuomas Knowles, Christopher Dobson, Luke Rajah, and Duncan White. Fluidic device, October 8 2015. US Patent App. 14/438,145.

[282] Emma Yates, Christopher Dobson, Therese Herling, and Tuomas Knowles. Fluidic separation and detection, September 15 2016. US Patent App. 15/036,455.

[283] Alexander C Johnson and Michael T Bowser. Micro free flow electrophoresis. *Lab on a Chip*, 18(1):27–40, 2018.

[284] Simon A Pfeiffer, Benjamin M Rudisch, Petra Glaeser, Matthias Spanka, Felix Nitschke, Andrea A Robitzki, Christoph Schneider, Stefan Nagl, and Detlev Belder. Continuous purification of reaction products by micro free-flow electrophoresis enabled by large area deep-uv fluorescence imaging. *Analytical and Bioanalytical Chemistry*, 410(3):853–862, 2018.

[285] A Guttman, AS Cohen, DN Heiger, and Barry L Karger. Analytical and micropreparative ultrahigh resolution of oligonucleotides by polyacrylamide gel high-performance capillary electrophoresis. *Analytical Chemistry*, 62(2):137–141, 1990.

[286] Christoph J Wienken, Philipp Baaske, Ulrich Rothbauer, Dieter Braun, and Stefan Duhr. Protein-binding assays in biological liquids using microscale thermophoresis. *Nature Communications*, 1:1093, 2010.

[287] Thomas R Covey, Edgar D Lee, Andries P Bruins, and Jack D Henion. Liquid chromatography/mass spectrometry. *Analytical Chemistry*, 58(14):1451A–1461A, 1986.

[288] John P Shockcor, Steve E Unger, Ian D Wilson, Peta JD Foxall, Jeremy K Nicholson, and John C Lindon. Combined hplc, nmr spectroscopy, and ion-trap mass spectrometry with application to the detection and characterization of xenobiotic and endogenous metabolites in human urine. *Analytical Chemistry*, 68(24):4431–4435, 1996.

[289] John P Larmann Jr, Anthony V Lemmo, Alvin W Moore Jr, and James W Jorgenson. Two-dimensional separations of peptides and proteins by comprehensive liquid chromatography-capillary electrophoresis. *Electrophoresis*, 14(1):439–447, 1993.

[290] Matthew Geiger, Nicholas W Frost, and Michael T Bowser. Comprehensive multidimensional separations of peptides using nano-liquid chromatography coupled with micro free flow electrophoresis. *Analytical Chemistry*, 86(10):5136–5142, 2014.

[291] Renata F Gerhardt, Andrea J Peretzki, Sebastian K Piendl, and Detlev Belder. Seamless combination of high-pressure chip-hplc and droplet microfluidics on an integrated microfluidic glass chip. *Analytical Chemistry*, 89(23):13030–13037, 2017.

[292] Andrew Evan Kamholz, Bernhard H Weigl, Bruce A Finlayson, and Paul Yager. Quantitative analysis of molecular interaction in a microfluidic channel: the t-sensor. *Analytical Chemistry*, 71(23):5340–5347, 1999.

[293] Daniel E Raymond, Andreas Manz, and H Michael Widmer. Continuous sample pretreatment using a free-flow electrophoresis device integrated onto a silicon chip. *Analytical Chemistry*, 66(18):2858–2865, 1994.

[294] Therese Herling, Thomas Mueller, and Tuomas Knowles. Fluidic analysis and separation, February 23 2017. US Patent App. 15/307,221.

[295] Thomas Müller, Paolo Arosio, Luke Rajah, Samuel IA Cohen, Emma V Yates, Michele Vendruscolo, Christopher M Dobson, and Tuomas PJ Knowles. Particle-based Monte-Carlo simulations of steady-state mass transport at intermediate Péclet numbers. *International Journal of Nonlinear Sciences and Numerical Simulation*, 17(3-4):175–183, 2016.

[296] B Srinivasa Reddy and Biswanath N Chatterji. An fft-based technique for translation, rotation, and scale-invariant image registration. *IEEE Transactions on Image Processing*, 5(8):1266–1271, 1996.

[297] M Spiga and GL Morino. A symmetric solution for velocity profile in laminar flow through rectangular ducts. *International Communications in Heat and Mass Transfer*, 21(4):469–475, 1994.

[298] Robert J Hunter. *Zeta potential in colloid science: principles and applications*, volume 2. Academic press, 2013.

[299] Jeffrey D Carbeck and Russel S Negin. Measuring the size and charge of proteins using protein charge ladders, capillary electrophoresis, and electrokinetic models of colloids. *Journal of the American Chemical Society*, 123(6):1252–1253, 2001.

[300] Stefan Westermann, Agustin Avila-Sakar, Hong-Wei Wang, Hanspeter Niederstrasser, Jonathan Wong, David G Drubin, Eva Nogales, and Georjana Barnes. Formation of a dynamic kinetochore-microtubule interface through assembly of the dam1 ring complex. *Molecular Cell*, 17(2):277–290, 2005.

[301] Boris Batas, Huwel R Jones, and Julian B Chaudhuri. Studies of the hydrodynamic volume changes that occur during refolding of lysozyme using size-exclusion chromatography. *Journal of Chromatography A*, 766(1-2):109–119, 1997.

[302] ATTO-TEC GmbH. Fluorescent Dye Catalog. *www.atto-tec.com*, 2018.